

S&G 3657

516  
957

Client Report 343901

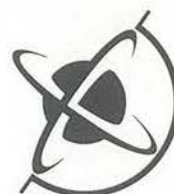
CONFIDENTIAL

**Quantification of  
seismic wavefield  
amplification by  
topographic features**

**A Report prepared for  
the Earthquake  
Commission**

**Rafael Benites and  
John Haines**

**July 1994**



*Institute of*  
**GEOLOGICAL  
& NUCLEAR  
SCIENCES**  
*Limited*



*Institute of*  
**GEOLOGICAL  
& NUCLEAR  
SCIENCES**  
*Limited*

**Quantification of seismic wavefield amplification  
by topographic features**

by

**Rafael Benites and John Haines**

**Prepared for**

**The Earthquake Commission**

**CONFIDENTIAL**

**Client Report 343901**

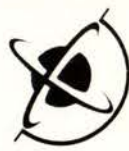
**July 1994**

**This report is an unpublished report of the  
Institute of Geological & Nuclear Sciences Limited.  
It may not be disclosed to, or acted upon by any other person  
without the prior written consent of the Institute.**



## CONTENTS

SUMMARY.....	1
PART I .....	3
1. INTRODUCTION.....	3
2. OBSERVATIONS OF TOPOGRAPHICAL EFFECTS AND COMPARISON WITH SIMPLE THEORETICAL MODELS .....	4
2.1 Experimental Results.....	5
2.2 Theoretical Results .....	7
3. COMPARISON OF EXPERIMENTAL AND THEORETICAL RESULTS.....	10
4. RECENT THEORETICAL MODELS.....	12
4.1 Two-dimensional complex topography .....	13
4.2 Three-dimensional topography .....	18
5. CONCLUSIONS .....	20
PART II .....	44
1. INTRODUCTION.....	44
2. 2-D MODELLING .....	45
2.1 Case 1 .....	45
2.2 Case 2 .....	49
2.3 Case 3 .....	50
3. 3-D MODELLING .....	54
3.1 Mountain.....	55
3.2 Canyon.....	56
4. CONCLUSIONS .....	58
ACKNOWLEDGMENTS .....	106
REFERENCES FOR PART I AND PART II .....	106



## **Quantification of seismic wavefield amplification by topographic features**

### **SUMMARY**

The present report is presented in two parts. In Part I a review of the experimental and theoretical research on the effects of surface topography on earthquake ground motion done in the last 20 years reveals significant disagreements between observations of the ground motion on top of elevated topographies, like mountain ranges and hills, and the corresponding theoretical predictions. Although the general trend of amplification on top of massive crests is predicted, the values of the amplification factors are underestimated by the predictions. In the past, these disagreements were attributed to the simplicity of the models involving isolated ridges of homogeneous material properties. In recent years there have been improvements in the theoretical methods to incorporate complex underground geological structures associated with two-dimensional mountain ranges, and to compute the ground motion in three-dimensional topographical features. It appears that the observed amplification factors are caused to a large extent by mountain base deamplification, in addition to the amplification on its top. The case of depressions is less controversial, mainly due to lack of observations for a thorough comparison.

In Part II several examples of modelling the effects of two- and three-dimensional generic topographies on the ground motion due to earthquakes are presented and discussed. The modelling is performed by using numerical methodologies developed in New Zealand. For the two-dimensional cases we consider three possible types of ridges, the first two corresponding to uplift, with the ridge being flanked by two small sedimentary basins of different irregular shapes. In the first of these cases the material properties of the ridge (i.e. density, velocities of  $P$  and  $S$  waves) are constant, and in the second the  $S$ -wave velocity varies with position and depth, in a way that resembles some observed uplifts. The last two-dimensional example corresponds to a ridge formed by tilt of a stack of irregularly shaped layers, exhibiting inhomogeneous material properties. Results for these cases show that the larger



amplifications, up to 12 times the amplitude of the incident wave, occur in the basins at points on the free surface close to the base of the ridge, for both homogeneous and inhomogeneous material properties. To a lesser degree, there is also amplification at the top of the ridge, up to 3 times with respect to the incident wave, which is in agreement with the results by the models discussed in Part I. Finally, we computed the seismic responses of three-dimensional canyons and hills whose material properties are constant, for several types of incident waves and for several angles of incidence (with respect to the vertical) and azimuths. The results show that amplifications up to 14 times the amplitude of the incident wave occur at the top of the ridge, and that the three-dimensional response is strongly sensitive to the shape ratios (i.e. major axis to minor axis, height to major axis) and to the input frequency.



# Quantification of seismic wavefield amplification by topographic features

## PART I

### 1. INTRODUCTION

By effects of topography on earthquake ground motion we refer to the spatial variations of the ground motion resulting from the scattering and diffraction phenomena introduced by the shape of the earth surface on the incoming waves caused by an earthquake. The study of such effects is therefore relevant to the assessment of earthquake damage in mountain ranges, depressions, or areas where there is a combination of both.

Regarding the effects produced by the presence of elevated topographies, like mountains, numerous observations of the damage caused by destructive earthquakes in hilly areas show consistently that the intensity of the damage is much larger at the top of the hill than at its base (Geli et al. 1988, reporting such observations since 1902).

In order to quantify such phenomena several experiments were carried out (Davis and West, 1973, Rogers et al. 1974, Griffiths and Bollinger 1979, Tucker et al. 1984) confirming in general the observed amplification trend at massive crests, regardless of the complexity of the geological setting of the region. Direct measurements of the spectral ratio of the motion at the top of the hill with respect to that at its base, yielded values of the corresponding amplification factors of up to 30 (Davis and West, 1973). It appears that the maximum values occur for input wavelengths comparable to the width of the hill at its base, and that they depend weakly on the shape ratio  $h/l$ , i.e. the ratio of the height  $h$  to the half-width  $l$  of the hill.

To characterise this amplification effect, several theoretical models of seismic wave propagation in mountains have been proposed since 1972. Earlier models considered a homogeneous half-space exhibiting an isolated ridge topography (two dimensions), and incident  $SH$ ,  $P$  and  $SV$  plane waves. To represent the wave propagation they used Finite



Difference schemes (Boore, 1972), Finite Element (Smith, 1975), Discrete Wave Number & Aki-Larner (1970) methods (Bouchon, 1973; Bard, 1982), Integral Equation and Boundary Integral (Sills, 1978, Sanchez-Sesma et al., 1982). Results from these models confirm, consistently, the observed amplification trend at the top of the ridge, but the values obtained for the top/base amplification factor are in the range from 1 to 3, for horizontal and vertical components of the motion (in plane), and for *SH* motion (antiplane), whether the amplification factor is determined from time domain (peak-to-peak) ratio or from frequency domain (spectral) ratio. The discrepancies between observed and predicted top/base amplification factors are dramatic, suggesting that the model of an isolated ridge in homogeneous half-space is too simplistic to represent realistic cases of seismic wave propagation in a mountain range. Since some of the above mentioned experiments involved two and three dimensional isolated ridges, the implication is that the effects due solely to the presence of the ridge topography may not be observed in nature but are combined with the effects introduced by other features of the ground. The case of depressions, like canyons, has been studied thoroughly theoretically (Trifunac, 1973; Smith, 1975; Bouchon, 1973, among the earlier) but only few observations are available for comparison. Perhaps the best known records are the two horizontal components of acceleration recorded by the Pacoima Dam accelerograph during the San Fernando 1971 earthquake (Trifunac, 1973; Boore, 1972; Bouchon, 1973).

In this report we review recent advances in the study of topographic effects in the ground motion. First we will summarise briefly the relevant details and results of the experimental and theoretical studies mentioned above, then we will present the latest theoretical efforts to incorporate two-dimensional realistic media and three-dimensional analysis in order to reduce the gap between observed and predicted amplification factors.

## **2. OBSERVATIONS OF TOPOGRAPHICAL EFFECTS AND COMPARISON WITH SIMPLE THEORETICAL MODELS**

In this section we describe briefly the results of some experiments carried out to quantify the effects on the ground motion of elevated topographies and depressions, as well as early theoretical attempts to characterise them. Then we will compare both and suggest the



probable reasons, in each case, for the reported discrepancy between observed and predicted amplification factors.

## 2.1 Experimental Results

### *Mountain Range*

Several aftershocks of the San Fernando 1971 earthquake were recorded at stations located on the top and at the base of the Kagel Mountain and the Josephine Peak. Davis and West (1973) computed the top/base velocity spectral ratios and found large amplification at wavelengths approximately equal to the width of the mountain at its base. Davis and (1973) West also applied their analysis to the seismic records observed on the top and base of the Butler Mountain, Nevada, caused by the collapse of an underground cavity. Their results in this case show large, frequency dependent amplification factors up to 10.

Rogers et al. (1974) recorded an underground nuclear explosion at several sites across the NASA Mountain, Nevada. This mountain range can be considered to be two dimensional in shape, of smooth geometry and regular properties (homogeneous). The wavefront of the recorded incident seismic waves was parallel to the ridge axis. Their computation of top/base ratios was restricted to the time domain since only analog records were available, yielding amplification factors of about 1.25 higher at the top. In addition Rogers et al. (1974) performed scale model experiments of the topographic effect using Oliver et al.'s (1954) seismic model and ultrasonic incident *P* waves. They found not only a qualitative agreement with the observed records, but were able to perform a parameter study of the effect of a hill in terms of angles of incidence and azimuth, slope of the hill and frequency. They found an amplification factor of about 1.55 corresponding to a diffracted Rayleigh wave. A seismic experiment in the Appalachian Mountains was carried out by Griffiths and Bollinger (1979), who recorded one earthquake and 136 events corresponding to quarry and mine blasts, at stations located on six topographical features. In this case the topography (corresponding to hill and valleys) can also be considered two-dimensional, with the incident waves from most events coming at azimuths nearly perpendicular to the mountain axis. The horizontal



seismometers were aligned parallel to the ridge strike so their records would correspond to the *SH* motion. However, the geological structure was clearly different from the one studied by Griffiths and Bollinger (1979), in that thin layers of soft sediments appear to cover the ridges, and these were not isolated but appeared as spatially periodic elevated topographies. In this case, too, the records were analogue, and the computed time domain amplification factors, top/base, yielded values between 1.7 and 3.4. A specific experiment to measure spectral differences of the motion in a small ridge was carried out by Tucker et al. (1984). They observed that the spectral ratios were almost independent of azimuth distance and size of the seismic events. The spectral amplification factor with respect to a nearby tunnel not located at the base of the ridge was about 8. In addition, they reported other observations at ridges with much smaller top/base spectral amplifications. Finally, Umeda et al. (1986) reported that boulders on top of a 100m high and 500m wide ridge were thrown off during the Western Nagama Prefecture, Japan Earthquake, 1984, suggesting the occurrence of anomalously high accelerations at the site. They computed a top/base spectral amplification factor of the order of 10. This small ridge is nearly two-dimensional and exhibits a non-homogeneous underground structure.

### *Depressions*

There are not many observations of ground motion in depressions (like canyons). Perhaps a unique case is the strong ground motion recorded at the two horizontal components of the Pacoima Dam accelerograph AR-240 during the San Fernando 1971 earthquake (Trifunac and Hudson, 1971; Boore, 1972). The recorded peak acceleration was as large as 1.25g. The question is: is this a good estimate of the actual acceleration field within the epicentral region? or it is the result of local site effects?

Looking at the regional scale, the accelerograph was at the bottom of a canyon, about 8 km south from the epicentre and on the strike of the fault plane (N70° W). However, looking at the local scale, the accelerograph sits on top of a small ridge inside the canyon. Considering that the peak acceleration occurs at 10 Hz, and assuming that the shear wave velocity is about 2 km/s, and a Poisson ratio of 0.25, the corresponding wavelengths would be about 340 m for



$P$  waves and 200 m for  $S$  waves (Bouchon, 1973). For this input, it appears that the effects of the ridge should be predominant. There is no consensus on this issue, which we address in the next section.

## 2.2 Theoretical Results

The problem of characterising the effects due purely to irregular free-surface topography is not trivial considering that even a flat free-surface introduces complex effects on the motion, depending on the type of incident wave ( $P$ ,  $SV$ ,  $SH$ ), angle of incidence and source characteristics. On one hand the flat free surface doubles the amplitude of  $SH$  waves, with no local variations and for any angle of incidence. On the other hand it amplifies dramatically the horizontal component of an  $SV$  wave incident at the critical angle, as shown in Figure 1 (Aki 1988). Some researchers attribute to this effect the localised large damage pattern observed during Whittier Narrows 1987 earthquake in Los Angeles (Aki 1988), and it must be expected when the free-surface topography departs from flat to irregular.

### *Mountains*

Boore (1972) used a Finite Difference scheme to represent the propagation of  $SH$  waves in a homogeneous half-space with a mountain topography. He calculated the top/base amplification factors for two slopes,  $23^\circ$  and  $35^\circ$ , and found that the maximum value was about 1.4. Smith (1975) used Finite Elements to study a triangular shaped symmetrical mountain, of  $20^\circ$  slope (shape ratio  $h/l = 0.373$ ). He found that the maximum top/base amplification factor, about 1.8, occurred for  $SV$  waves for values of input wave lengths equal to 1.5 times the half width of the mountain. Bouchon (1973) modelled a symmetric ridge of cosine shapes, for incident  $SH$ ,  $P$  and  $SV$  waves, using the Discrete Wave Number DWN technique (Aki-Larner 1970). His results for vertically incident  $SH$  emphasised the effect of the shape ratio for values  $h/l = 0.23, 0.4, 0.67$  and  $0.8$ , setting the input wavelength as  $\lambda = 5h$ . For example, for  $h/l = 0.23$  (i.e.  $\lambda = 1.15l$ ), the amplification factor top/base was about 1.25, while for  $h/l = 0.8$  ( $\lambda = 2l$ ) it was about 1.7. These values increased slightly with the angle of

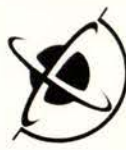


incidence. For the case of  $P$ - $SV$ , keeping  $h/l = 0.4$  and  $\lambda = 4h$  ( $\lambda = 1.6l$ ), the top/base amplification factors were about 1.5 and 1.4 for vertically incident  $P$  and  $SV$  plane waves, respectively. While the effect of a  $35^\circ$  angle incidence can be neglected for  $P$ , it increased the amplification factor for  $SV$  up to 2.3 (Figure 2).

There have been other studies of the effects of elevated topographies using modifications of these techniques (Zahradnik and Urban, 1984 with Finite Differences, Bard 1982, with DWN). Although they confirmed the observed amplification effect at the top, it remains always less than a factor of 3. A summary of the results for  $SH$  waves is shown in Figure 3 for a mountain of  $h/l = 0.4$ . Here the frequency response in terms of the non-dimensional frequency  $\eta$  is computed for six stations distributed down the mountain slope, from top to bottom. Note that in this model the quality factor  $Q$  has been incorporated into the DWN procedure.

### *Depressions*

Since Trifunac (1973) presented his closed form solutions for the displacement fields produced by plane  $SH$  waves propagating in a half-space with cylindrical canyon topography of semi-circular and semi-elliptical cross-sections, the seismic response of two dimensional canyons has been studied thoroughly using various numerical techniques developed to incorporate in the solution the geological complexities and type of incident seismic wave encountered in realistic problems (Aki 1988). The exact frequency response of a semi-circular canyon to incident  $SH$  waves is shown in Figure 4, at eight stations distributed across it. In Figure 4  $a$  is the radius of the canyon,  $\omega = 2\pi f$  ( $f$  is frequency),  $\gamma$  is the angle of incidence. The response is given for three *angles* of incidence,  $0^\circ$  (vertical),  $30^\circ$  and  $90^\circ$ , measured clockwise from the vertical. We observe a remarkable variability of the site effects, showing that the largest amplification occurs at the edges of the canyon. Both the amplitude and variability of the response are significantly affected by the angle of incidence, reaching an almost constant value of 4 (twice the response due to the flat surface) at the edge on the incident side, for  $\gamma = 90^\circ$ . Similar results were obtained by Sanchez-Sesma and Rosenblueth



(1979) using a boundary integral scheme, which in turn can be applied to problems involving arbitrary cross-sectional shapes. Both the analytical solutions due to Trifunac and the results of the Boundary Integral method have become testing benchmarks for other approximate techniques aimed to compute accurately the effects of irregular topographies on the ground motion.

Bouchon (1973) presented the case of a cosine-shaped depression (Figure 5) for incident  $P$ ,  $SV$ , and  $SH$  waves, first by fixing the shape ratio  $h/l$  to 0.62 (top), then by assuming several values of shape ratios for  $SH$  only (bottom). This parametric study of the responses emphasises the relation between input wavelength  $\lambda$  and the depth of the depression  $h$  in the form  $\lambda = 5 h$ , considering that this relation is characteristic of the responses for input wavelengths in the range between  $2 h$  and  $20 h$ .

As these effects became important in the modern design of long linear canals, bridge supports and dams, researchers have extended their analyses to more complex geological structures. Among them Wong (1982) studied the case of  $P$  and  $SV$  waves scattered by circular canyons, for the first time; Sanchez-Sesma (1985) presented an analytical expression (originally due to Macdonald, 1902) for  $SH$  waves diffracted by a wedge-shaped ridge or depression, Moeen-Vaziri and Trifunac (1988) studied the shear motion in canals of arbitrary cross-sectional shape, Dakoulos and Gazetas (1986) computed the vibrations of embankment dams due to input shear waves, and Vogt et al. (1988) treated the case of a canyon of arbitrary cross-sectional shape in layered half-space. The time domain solutions for  $P$ ,  $SV$ ,  $SH$  and Rayleigh waves in a semi-circular canyon of radius  $a$  were given by Kawase (1988), using a hybrid method based on DWN and Boundary Element methods. Figure 6 shows the transient motion at a dense array of stations distributed along the range, for  $SH$  (top first) and  $SV$  (middle and bottom) incident waves with Ricker wavelet source time function of central non-dimensional frequency  $\eta = 2$ , where  $\eta = 2a/\lambda$ . The remarkable features in these seismograms are the diffracted waves (or "creeping" waves) travelling in the canyon which, on interacting with the incident wave, cause a very localised amplification and phase shift at the edges.



The extensive theoretical work mentioned so far has helped to confirm the observed amplification patterns of the ground motion due to irregular free-surface topography and to understand the basic wave phenomena involved in it. This is summarised in Table 1, for ridge and canyon irregularities. If these theoretical models could be verified by direct comparison with data, they could then be used for a reliable estimation of the ground motion in sites where no earthquakes have been recorded. Such data are considered in the next section.

### 3. COMPARISON OF EXPERIMENTAL AND THEORETICAL RESULTS

Although the amount of research on two-dimensional modelling of irregular topographies is extensive, few experimental data or other type of observations are available for comparison in the case of canyons. This is mainly because few geological configurations regarded as depressions or canyons are long enough to be considered two-dimensional. As pointed out by Trifunac (1973) one of those could be the Kern Canyon, in Sierra, Nevada. Another which at least would be satisfactory for qualitative analysis is the Pacoima Canyon, in the vicinity of the Pacoima Dam. The situation is different for elevated topographies, as mentioned in the introduction, and direct comparisons of theory and experiment are possible for various cases. For example, response spectra have been obtained at two stations over granite in the Kagel Mountains (Davis and West 1973). Bard (1983) tried to model the observed amplifications with an isolated ridge. His comparisons are shown in Figure 7 (a), (b). Many other authors have contributed to similar comparisons, and their results are summarised in Figure 8 (time-domain), and Figure 9 (frequency-domain), in terms of the shape ratio of the ridge, and for several events (both figures reproduced from Geli et al. 1988). In these figures open symbols represent observed result, the darker ones being regarded as three-dimensional observations (Davis and West 1973), while closed symbols represent those from theoretical models (two and three dimensions). The code for each symbol prescribes the author and year of the results, as specified in the caption. Only one paper for the three-dimensional results has been included (Zhengpeng et al. 1980) because his results are directly comparable with those reported for the two-dimensional case. The non-dimensional frequency is defined as  $2a/\lambda$ . In



both Figures 8 and 9 we note generally a significant mismatch of observed and predicted results. In the time-domain the horizontal component is predicted better than the vertical component, which shows a large scatter for different observed events. In the frequency domain we observe drastic mismatches, particularly when the comparison involves two-dimensional models. For example, for  $h/l = 0.4$  the values of observed and best predicted top/base amplification factors are in the ratio 30/2 for the horizontal component, and about 9/1.6 for the vertical component.

In the case of depressions, Trifunac (1973) associated the large values of acceleration recorded at the Pacoima Dam accelerograph with the amplification effects computed at the edges of a cylindrical canyon of semi-circular cross-section shape. The comparison is very qualitative, based on the assumption that different sections of the output wave at the canyon came from different fracturing sections of the fault. A more thorough modelling was proposed by Bouchon (1973), who considered the canyon as regional scale, and the top of a small ridge within the canyon (where the accelerograph sat) as local site scale. His comparisons show good qualitative agreement (Figure 10) although the amplitudes cannot be matched.

Taking into account most of the work done between 1972 and 1984 on the observations and theoretical models of topographical effects on ground motion, and their comparison, we draw the following conclusions.

For a mountain:

- There is a consistent broadband amplification at the top of the mountain, which appears to reach its maximum when the wavelength of the incident wave is comparable to the mountain width at its base.
- The base of the mountain suffers a trend of amplification-deamplification, ranging between 1.25 and -0.5 with respect to the amplitude of the incident wave, depending on the observed top/base amplification factors. For incident  $P$  waves the deamplification



starts at large wavelengths (i.e. several times the mountain width), while the maximum amplification factors occur for wavelengths slightly longer than the mountain width.

- The amplification is lower for incident  $P$  waves than for incident  $S$  waves, but it is slightly larger for inplane motion ( $P$ - $SV$ ) than for antiplane motion ( $SH$ ).
- The amplification is lower on the flanks of the mountain than at the top, but it develops rapid phase variations causing large differential motions.
- The amplification is weakly dependent on the shape ratio, but strongly dependent on the angle of incidence.
- There is a remarkable mismatch between observed amplifications at the top of a mountain and those predicted by their corresponding theoretical models, suggesting that the models may under-estimate the response of the mountain by factors up to 15. The mismatch is more pronounced in the frequency-domain than in the time domain.

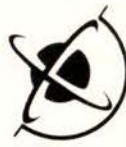
For Depressions:

- There is not enough experimental data to check the results of theoretical models of depressions. Exact results for ideal canyons predict large amplifications at the edges and deamplifications in the center. The amplification depends strongly on the angles of incidence and weakly on the shape ratio.
- The Pacoima Dam horizontal acceleration records have not been modelled satisfactorily.

In the next section we will review the theoretical efforts since 1984 aimed at decreasing the gaps between observations and theory. We will no longer make distinctions between elevated topographies and depressions, since most of the recently developed methods apply to both, as well as to sediment filled basins.

#### **4. RECENT THEORETICAL MODELS**

As efficient numerical methods to compute seismic wave scattering and diffraction by irregular topographies developed, it became clearer that the gap between the observed and



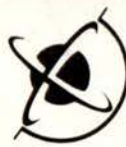
predicted values of amplification was due to the simplicity of assuming a two-dimensional, isolated, homogeneous topographical feature. In most real experiments the surface geology was well known. For example, the Kagel Mountain and the Josephine Peak, in California (Davis and West, 1973) are composed of granite and dacite, respectively, from top to base. However, a suitable 2-D model of homogeneous material (Bard and Tucker, 1985) predicted responses far below those observed. The disagreements were attributed to the marked three-dimensionality of the mountains, and to weathering effects on their tops (Rogers et al., 1974). On the other hand, experiments on two-dimensional mountain ranges (like NASA Mountain, Appalachian Mountain) yielded large discrepancies too, even for *SH* calculations. The possible causes for the discrepancies were summarised as follows:

1. The recording sites were covered by thin layers of low-velocity alluvium.
2. The topographical features were not isolated but belonged to an environment of periodic, similar structures or neighbouring topography.
3. There was an irregular layer structure underneath the topographical feature.
4. The topographical feature was prominently three-dimensional.

We shall divide this part of our review in two subsections: complex two-dimensional topographic modelling, and three-dimensional modelling.

#### **4.1 Two-dimensional complex topography**

The studies reviewed here are mainly due to P.Y. Bard and B.E. Tucker (1985), and Geli et al. (1988). The case of neighbouring topographies affecting the response of a homogeneous mountain was treated by Bard and Tucker (1985) using the DWN method. Figure 11 shows the response of a structure composed of three similar sinusoidal ridges in a homogeneous half-space, for vertically incident *SH* waves, at six stations distributed from top to bottom along the flanks of two adjacent ridges. For comparison, the response of a single ridge is given by a solid line (as in Figure 3). It appears that the presence of neighbouring ridges amplifies the motion at the top of the central ridge, and deamplifies the motion at its base,



which in turn induces the largest peak in the corresponding spectral ratio (see Figure 13 (b)) of amplitude 10 at  $\eta = 0.7$ .

The effects for other station distributions (inner and outer flanks) are similar but less strong, systematically showing their maximum amplitude at the top. Geli et al. (1988) extended this study to include underground layering, in addition to neighbouring topographies. Their results are shown in Figure 12, which also describes the stratified medium used in the computations. As in Figure 11, the solid line corresponds to a single ridge. In this case the amplifications tend to be narrow-banded, three to four times larger than their corresponding homogeneous case, for all stations. This effect can be attributed to the interference between subsurface layering and surface topography. The largest amplification of up to 12 occurs at the top of the central ridge, for wavelengths comparable with the width of one ridge. Explicit comparisons of the amplifications at the top of the ridge for both homogeneous underground and layered underground are given in Figure 13, (a) and (b) respectively. The comparisons are made for an isolated ridge, and for the central ridge of three-neighbouring identical ridges. The results are given as the spectral ratios of top to base for the isolated ridge (full line), top to base for the central ridge (thick dotted line) and top to next lateral base for the central ridge (thin dashed line). In all cases the largest amplification is given by the spectral ratio for the latter case.

The next important work by Geli et al. (1988) was the study of the effects of subsurface layering in an isolated ridge. They set up the models shown in Figure 14, according to the assumptions that the subsurface layering in elevated topographies can be associated with weathering (top) i.e. uniformly covered with thin layers of soft material; and erosion (middle and bottom) i.e. covered with irregular layers of sediments whose thickness increase downward on the flanks. This case is treated with a modified version of the Aki-Larner (1970) method, in which the effect of the flat layers is introduced by means of the Thompson-Haskell propagator matrix (Aki and Richards, 1980). The quality factor  $Q$  for each layer is also incorporated. Results are shown in Figure 15, for  $SH$  waves (vertically incident) for two velocity values of the surface layer,  $0.6\beta_3$  full line and  $0.4\beta_3$  dashed line, where  $\beta_3$  is the



shear wave velocity of layer 3. Each row from left to right represents the amplifications at the top, at the bottom and the top/base spectral ratios, for each configuration. It is shown that in every case the maximum amplification factor is below 3, occurring at about  $\eta = 0.8$ . It is remarkable that there is a low frequency amplification (of up to 1.1) which is independent of the surface layer velocity and underground layering. It is also noted that the narrow band top/base spectral peaks of higher frequencies are actually the result of base deamplification. These amplifications seem insensitive to the deep underground structure (compare (b) and (c)). Although the types of inhomogeneous mountains treated by Bard and Tucker (1985) and Geli et al. (1988) are complex, they do not solve the problem of the large observed amplification factors. It was evident, however, that such large values could be the result of base deamplification rather than authentic amplification at the top. When there is a deamplification it is better to compute explicitly the transfer functions at each station. Taking into account that there are numerical problems related to the Rayleigh-ansatz assumption in the Aki-Larner methods (not discussed in Geli et al. 1988), an alternative method was developed by Benites (1990) using a hybrid method based on Boundary Integral and Gaussian beam methods. The simple case of an *SH* wave impinging upon a ridge of cosine shape was treated, in which the shear wave velocity varied linearly with depth. The purpose was to isolate the effects of the velocity gradient by studying the response of the mountain as it departed from the homogeneous case. The results relevant to our review are given in Figure 16, showing the spectral transfer function for five stations from top (No 1) to bottom (No 5), in terms of the non-dimensional frequency  $\eta$ . The velocity gradient is 100% in (a), i.e. the velocity at the bottom is twice the velocity at the top; and 0% in (b) (homogeneous). The most striking feature observed in Figure 16 (a) is the rapid increase of the spectral peak amplitudes towards the top, reaching a maximum value of about 14, or 28 absolute amplification value (amplitudes are normalised with respect to the response of the flat-free surface). A closer look shows that the frequency at which the maximum amplitude occurs shifts towards the top, from about  $\eta = 0.5$  for the station in the bottom to  $\eta = 0.7$  for the station at the top. The amplification factor computed from the spectral ratio top/base at  $\eta = 0.7$  is about 18. For comparison, the amplification factor at the top of the homogeneous mountain is about 5. It is worth noting that in the homogeneous case the peak amplitude also



occurs at  $\eta = 0.7$  at the top, but at  $\eta = 0.2$  at the bottom. From the theoretical results of this particular case we may infer the effects of the vertical inhomogeneity:

- (1) The spectral amplitudes of the ground motion increase everywhere, from the top of the mountain to the base, but most strongly along the flanks towards the top, and gently at the bottom. It appears that some deamplification occurs in the high frequency range.
- (2) The frequencies of the spectral peak amplitudes at the bottom shift upwards for frequencies less than that corresponding to a wavelength of one fourth of the width of the mountain ( $a/4$ ). It is not clear if this shift also occurs at stations on the top.
- (3) The frequency shift of the peak ground motion at the bottom induces large amplification factors at the top, reaching values of up to 18 for 100% shear velocity gradient.

Benites (1990) also computed the time domain solution for *SH* waves of a mountain with vertical heterogeneity in order to study the effects on the wave propagation. These are shown in Figure 17, for four gradients ' $g$ ', aspect ratio  $h/a = 0.4$  and Ricker input wavelet with central frequency  $\eta = 2$ . For this particular case  $a = 2.5$  (units of length) and  $\beta_h$  is fixed at  $\beta_h = 2$  (units of length/ sec). Since ' $g$ ' is defined by  $\beta_o = \beta_h - gh$  (see top of Figure 16),  $\beta_o = 2 - g$  (absolute). So a gradient  $g = 0.25 \text{ sec}^{-1}$  implies that the surface velocity  $\beta_o = 1.75$ .

In addition to the discussion by Bard (1982) on the differential motions generated along the flanks of a homogeneous ridge, it is worth noting that the elevated topography keeps the amplitude of the incident wave almost unchanged, while it generates an outward going diffracted wave whose amplitudes increases as it propagates from the center towards the edges, along the flanks (see Figure 17,  $g = 0$ ). Just outside the region of the mountain, the amplitude of the diffracted wave decreases abruptly. When the velocity gradient is introduced, it induces a strong wave interference within the ridge and the effects observed in the homogeneous case become more pronounced. For example, for  $g = 1$  it is observed that the diffracted wave loses its energy rapidly outside the ridge. The conclusions drawn from this numerical experiment cannot be generalised since the proposed model is very simple;



however the results suggest that the response of a mountain with realistic geological structure is strongly affected by near surface layering involving shear wave velocities increasing downwards, causing large amplifications at its top.

So far in this section we have described studies involving sinusoidal ridges with complex velocity distributions and *SH* waves. Kawase (1990) studied the effects of a homogeneous ridge, whose free-surface topography conforms to an arc of a circle, on propagating *SH*, *P-SV* and Rayleigh waves. His results for *SH* incidence are very similar to those already described for the sinusoidal homogeneous ridge. For *SV* incidence the character of the diffracted wave generated within the ridge is entirely different from the *SH* case. The corresponding time domain solution for  $30^\circ$  incidence is shown in Figure 18, for horizontal (a) and vertical (b) components of displacement. In (a) the first arrival must correspond to a diffracted *P* wave, judging from its apparent velocity. Also, the amplitude of the direct *SV* wave varies within the ridge, being significantly amplified along the slope on the side of incidence. Later arrivals appear to correspond to diffracted *P*, *SV* and Rayleigh waves, the *P* and *SV* propagating backwards as well. For *P* wave incidence, shown in Figure 19, the diffraction is less complex than for *SV*, having clearly defined diffracted *P* and Rayleigh waves at the edges. An interesting case reported by Kawase (1990) is that the ridge appears to split an incident Rayleigh wave into two wave-trains, clearly observed in both horizontal and vertical components. In each component these waves have the same amplitude, which is about one-half the amplitude of the incident wave. Diffracted *P* and *SV* waves also appear to be generated but with very small amplitudes.

Summarising the present section, two-dimensional models of elevated topographies with complicated geological configurations have helped to reduce the disagreement between observed amplification factors at the top of a mountain and those predicted for the isolated, homogeneous ridge, but their predictions are not yet satisfactory. They have improved the understanding of the phenomena, suggesting that the observed large amplification factors may be induced to a large extent by deamplification at the base of the ridge. Models associated with combined weathering and erosion of an isolated ridge do not improve the predictions, yielding amplification factors of less than 3. On the other hand, models that



incorporate either weathering or neighbouring ridges yield a factor of 10. It is demonstrated that the response of the ridge is not affected by the deep underground structure, but it is by the near-surface layering. Simple models of ridges with vertical variation of velocity show that the response is strongly affected by the velocity gradient, yielding amplification factors of up to 18. This value results from large amplifications on the top and rather small ones at the bottom, due to shifting of the frequency at which the maximum amplification at the bottom occurs.

#### **4.2 Three-dimensional topography**

Modelling of the effects of three-dimensional topographies on seismic ground motion is still a subject in development, even for simple geometries. At present the slow progress is due more to computational limitations in obtaining solutions for frequencies of significance in strong ground motion, than to the lack of suitable numerical methods already developed for the problem.

Perhaps one of the earliest attempts to study seismic wave propagation in 3-D media is the one by Evans et al. (1954), using scale models, with piezoelectric source of acoustic waves. These models corresponded to stratified elastic plates, and their three-dimensionality was intended mainly to study the wavefronts resulting from reflections at the front and back faces of the models. It should be noted that the authors modelled Lamb's problem in free elastic plates, obtaining excellent agreement with the theory. Early purely theoretical attempts used equivalent surface load distribution to represent the scattering field by depressions (and inclusions) of gentle slopes (Hudson 1972). A first order approximation of Green's function was developed to reproduce some observed surface waves. Since then, several authors have contributed to the subject, namely Singh and Sabina, 1977; Lee, 1982; Zhengpeng et al., 1980; Sanchez-Sesma, 1983; Wong, 1966; Luco and Wong, 1987; Mossessian and Dravinski, 1989. Among them, perhaps the most complete study is due to Zhengpeng et al. 1980, for a topography of truncated conical shape on a homogeneous half-space (Figure 20). The cone can be upright, representing a mountain, or dipped downwards, representing a depression. The problem of scattering of an incident shear wave is reduced to a two-dimensional problem



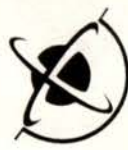
using axisymmetry, in terms of the azimuthal angle  $\phi$ . The wave propagation in the 2-D media is then solved by Finite Differences. Results for the hill are shown in Figure 20, for the spectral ratio of the radial and tangential components with respect to the incident wave. The slope of the cone is  $45^\circ$ , and the ratios are given in terms of a non-dimensional period

$$T = 2\pi/\omega \quad R = \lambda/R$$

where  $R$  is the radius of the cone

Zhengpeng et al. argue that if  $\lambda \geq R$  and the input motion is horizontal, the amplification of the ground motion is due to the vibration of the hill as a whole, and if the input is vertical the amplification is due to convergence of wave energy propagating from the base upwards. The spectral ratio reaches its first maximum at  $To = 3.2 R/\beta$ , for  $H/R = 1/3$ . The amplifications shown in Figure 20 are less than 5. According to the authors the method predicted the amplification factor of the tip of an isolated hill observed during the Haicheng 1975 earthquake. No details about the observed values are given. Sanchez-Sesma (1985) treated the case for a hemispherical cavity for vertically incident  $P$  waves. He used azimuthal decomposition (axisymmetry) and expansion of the scattered wavefield in terms of a specified set of basis functions. The boundary conditions are satisfied in the least squares sense. His results are for relative ground motion for several single frequencies. For the vertical component of the motion he obtained a maximum amplification of about 3.4 for a frequency that corresponds to a wavelength equal to twice the size of the cavity, and about 3.2 in the case of a ridge (same size of wavelength). No results are given for the frequency domain amplification, nor for inclined incidence, nor for wavelengths shorter than 1.33 times the width of the ridge or cavity.

Luco et al. (1989) have studied the case of the three-dimensional response of a canyon in a layered half-space. The canyon is infinitely long but of arbitrary cross-sectional shape, and the incident wave ( $SH$ ,  $P$  or  $SV$  plane waves) impinges in the underlying half-space with incident angles measured with respect to the vertical and horizontal axis of the canyon. The authors compare their results for simple geometries in the limiting two-dimensional case with the corresponding results by 2-D methods, and perform a comprehensive parametric study of



the 3-D canyon with semi-circular cross-section. They demonstrate that the effect of the horizontal angle of incidence strongly affects both the amplitude and the variation of the motion within the canyon. They also perform a test to compute the ground motion at the Pacoima site, obtaining amplifications of up to a factor of 6 for a frequency of 5 Hz.

## 5. CONCLUSIONS

We have reviewed the research work regarding the effects of topography on earthquake ground motion of the last 20 years. Observations of the shaking intensity in hill areas during destructive earthquakes suggests that the tops of hills and mountains are subjected to anomalously large amplifications. Measurements of ground motion confirmed this, and theoretical modelling aimed to characterise the amplification effect in simple, homogeneous, isolated topographies showed that indeed amplifications occur at the top of mountains, but predicted values were far below those observed: the maximum predicted amplification factors were below 3, while the maximum observed, at the top was 30. New methods were developed in order to incorporate the modelling of complicated geological configurations associated with topographies. These included weathering, sedimentation neighbouring topographies and vertical velocity gradient.

Only the vertically inhomogeneous mountain yielded large values of the amplification factors, comparable to those observed; but overall, the importance of the new developments has been to improve our understanding of the processes that lead to such large amplification factors. It has become clear that deamplification at the base of the mountain is responsible to a large extent for such large factors. It was also concluded that only the near surface layering has a strong effect on the response of a mountain. The deep underground structure has little effect.

Regarding the three-dimensional modelling of ground motion in topographies, none of the proposed models so far has given strong evidence that the third dimension contributes to large amplifications. An important outcome is that the response of the topography is



strongly affected by both the azimuthal and vertical angle of incidence. This is highly relevant to prediction of strong ground motions at a site close to the epicentre, as well as far-field sites. Three dimensional modelling of a topographic feature close to the epicentre should include the radiation pattern produced as the rupture propagates along the fault. Finally, the performance of all theoretical models, 2-D and 3-D, compared with the experimental data, is summarised in Figure 21. Large discrepancies still exist, and it seems that more work, both theoretical and experimental, needs to be done to confidently predict the effects of topographies on seismic motion.



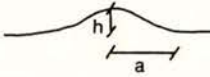
2D Structure \ Effects	Basic phenomena	Spectral characteristics	Application to Earthquake Engineering
Surface topography 	Diffraction of outward propagating surface waves.  Energy focusing in convex parts (such as mountain top).	Broad band effects centered on the frequency for which the wavelength is comparable to the width of the topographic feature  $(\lambda = 5a \text{ to } \lambda = a/4)$	<ul style="list-style-type: none"> <li>- Amplification on top, deamplification at mountain base differential motion on slopes.</li> <li>- Effects much larger on the horizontal components than on the vertical component.</li> </ul>
	Diffracted or "creeping" waves propagating within the canyon.  Strong interference with the incident wave at the edges of the canyon.	Large variability of the amplitude spectra from site to site: broad band outside the canyon, narrow band inside the canyon. Strong dependency on the angle of incidence.	<ul style="list-style-type: none"> <li>- Response depends strongly on the angle of incidence: amplification on the side of the incidence, deamplification on the side opposite to the incidence.</li> <li>- Effects larger on the horizontal components than on the vertical.</li> </ul>

Table 1. Summary of basic phenomena, spectral characteristics and applications to earthquake engineering for two 2-D structures.

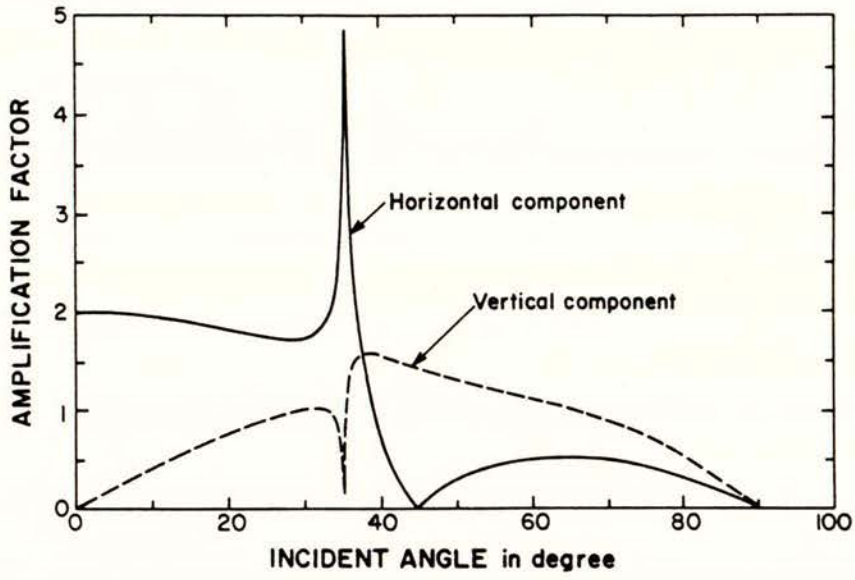


Figure 1: Amplitude of horizontal (solid line) and vertical (broken line) component displacement at the free-surface due to incident  $SV$  waves plotted as a function of incidence angle, for the case of Poisson's ratio 0.25 (from Aki, 1988).

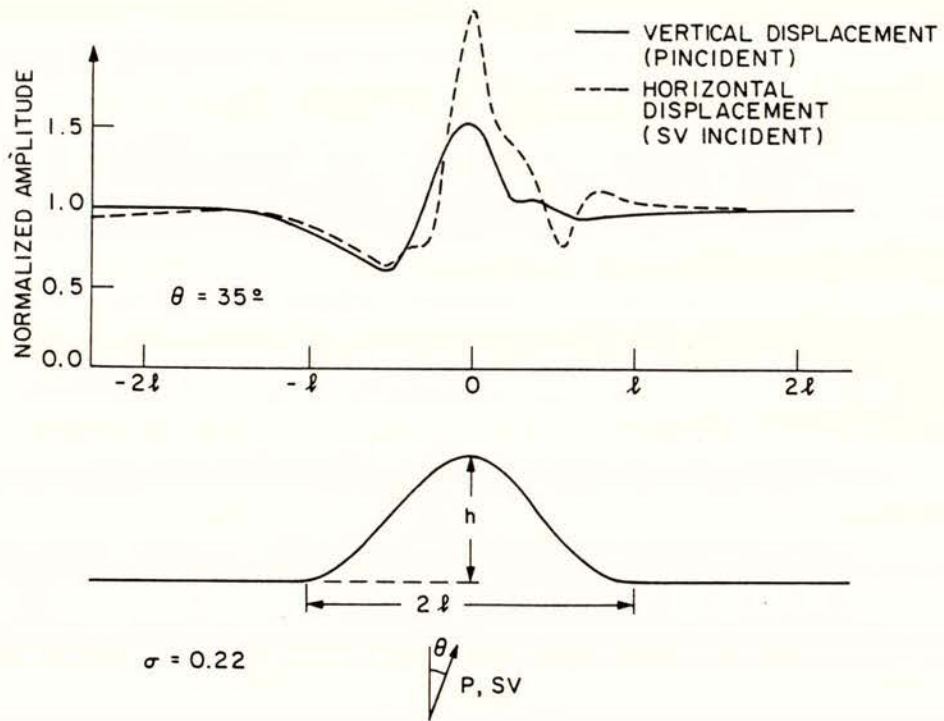


Figure 2: Normalised amplitude of synthesised displacement for  $P$  and  $SV$  waves upon a cosine-shaped ridge. Shape ratio  $h/l = 0.4$  (from Bouchon, 1973).

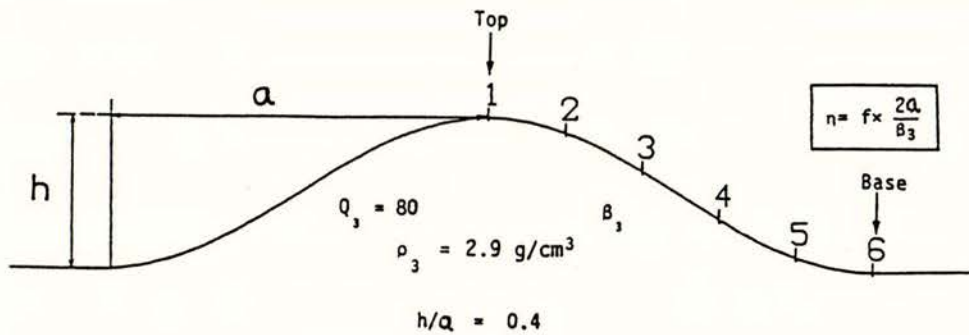
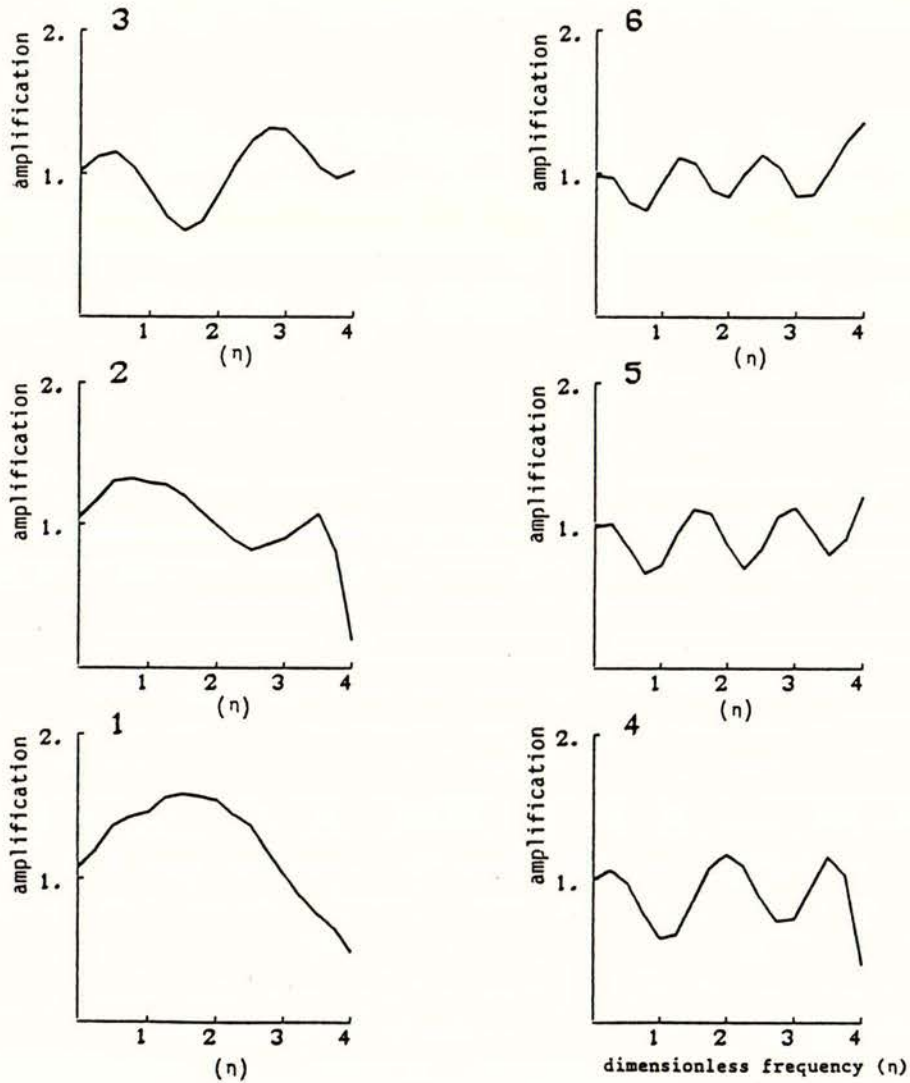
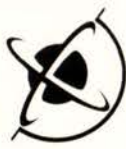


Figure 3: SH Fourier transfer functions obtained at six surface sites for an isolated, homogeneous ridge.  $h/l = 0.4$ .

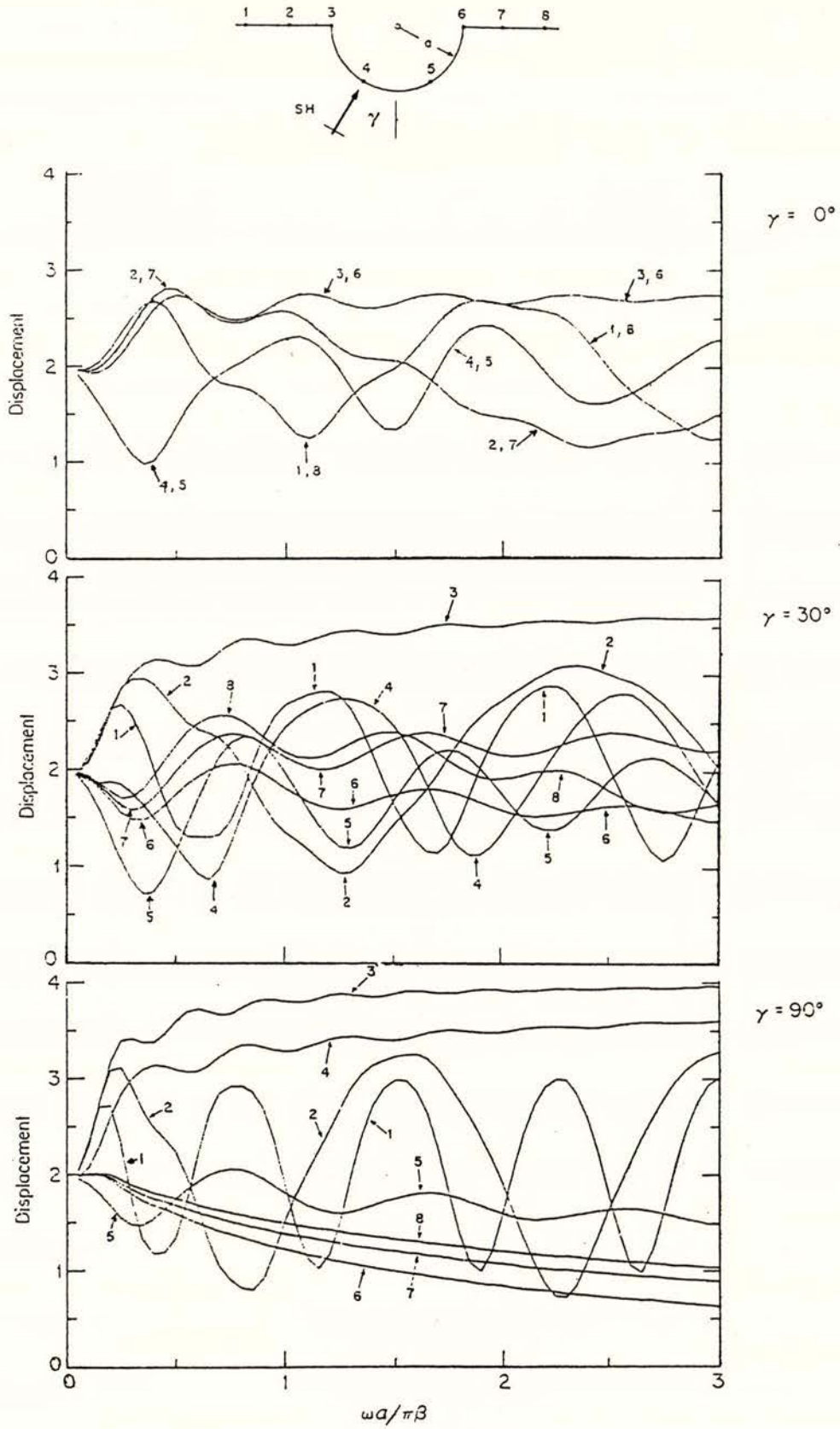


Figure 4: Frequency response at 8 sites along the circular canyon, for angles of incidence  $\gamma = 0^\circ$  (top),  $\gamma = 30^\circ$  (middle) and  $\gamma = 90^\circ$  (bottom). Note that  $\omega a / \pi \beta = 2a/\lambda$ .

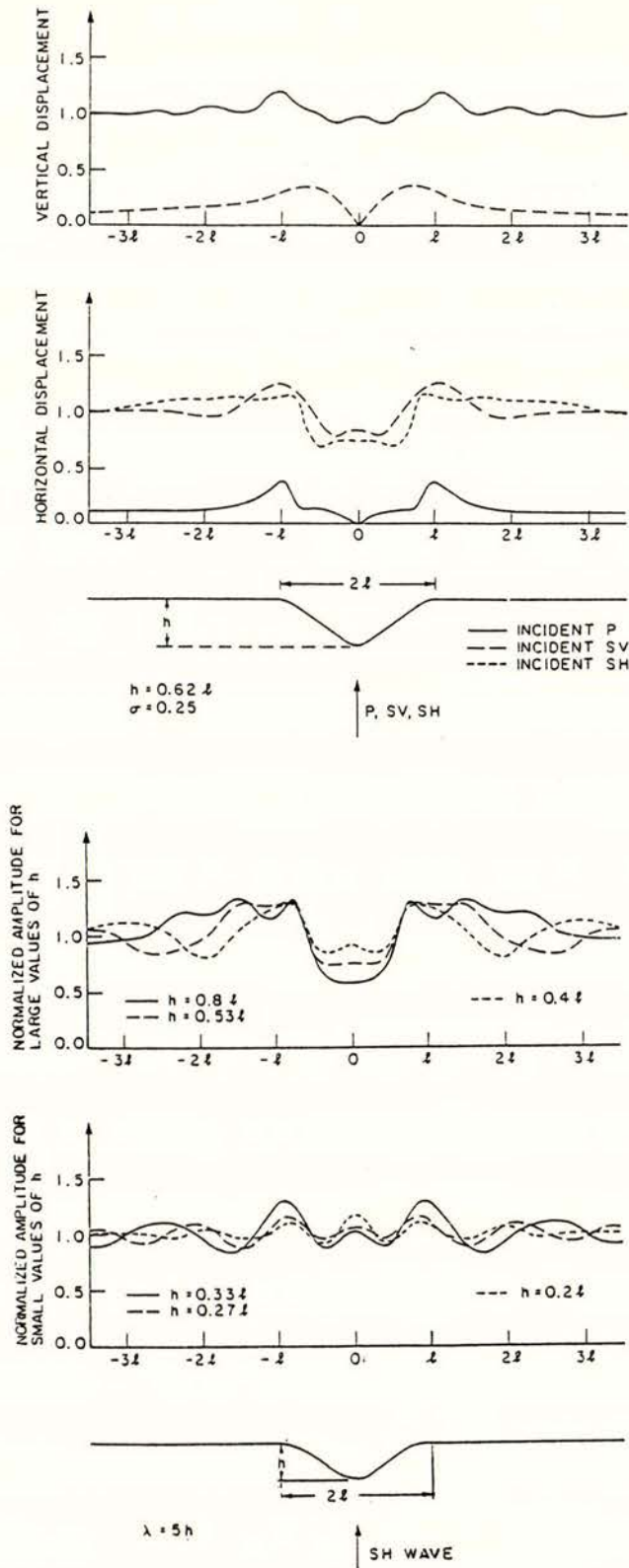


Figure 5: Ground motion amplitude spatial distribution upon the incidence of  $P$ ,  $SV$  and  $SH$  waves, for fixed shape ratio  $h/l = 0.62$  (top), and for several values of  $h/l$  for incident  $SH$  waves (bottom). Since  $\lambda = 5h$ , note that input wavelengths vary between  $l$  (for  $h/l = 0.2$ ) and  $4l$  ( $h/l = 0.8$ ) (from Bouchon, 1973).

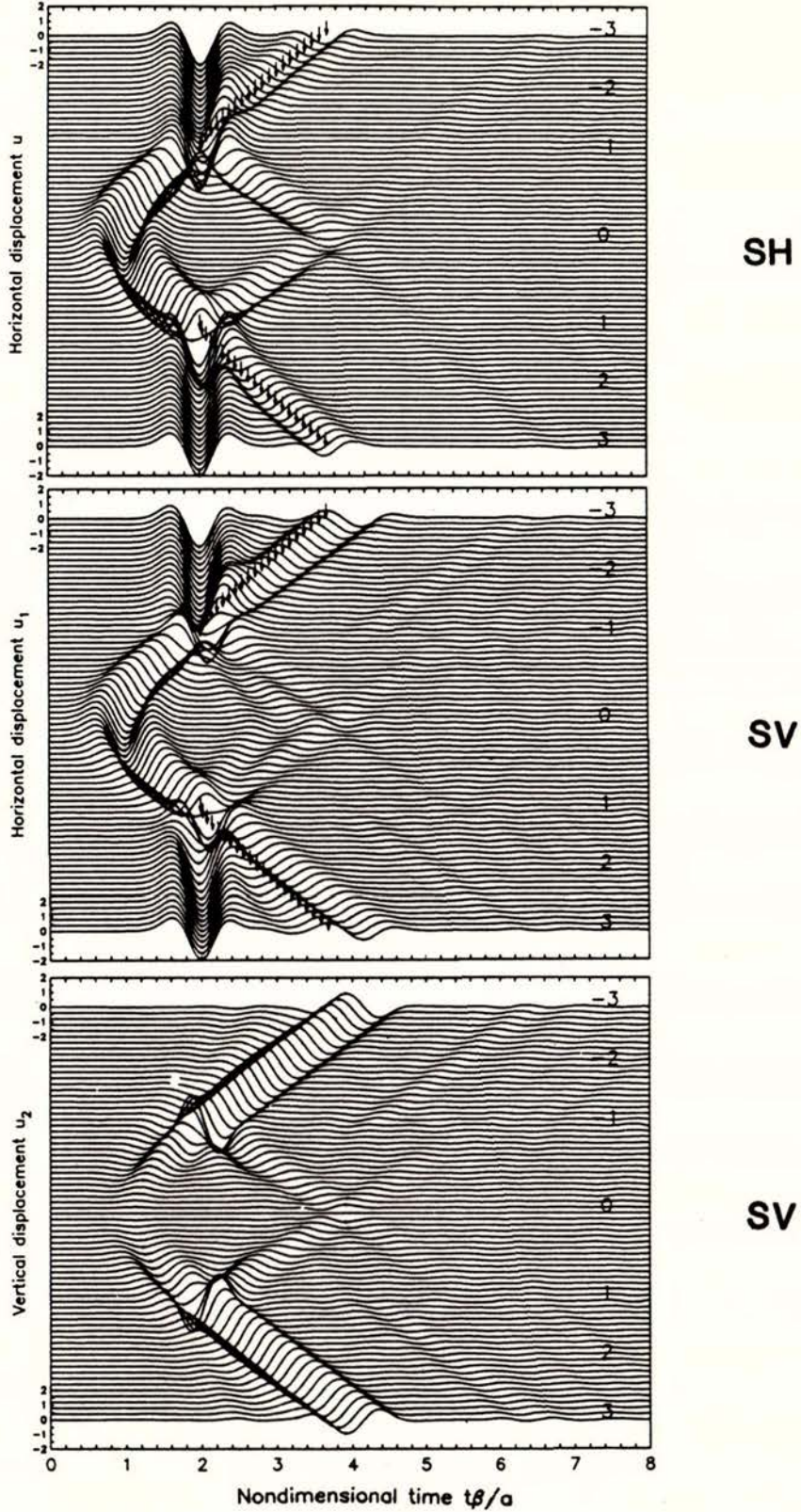
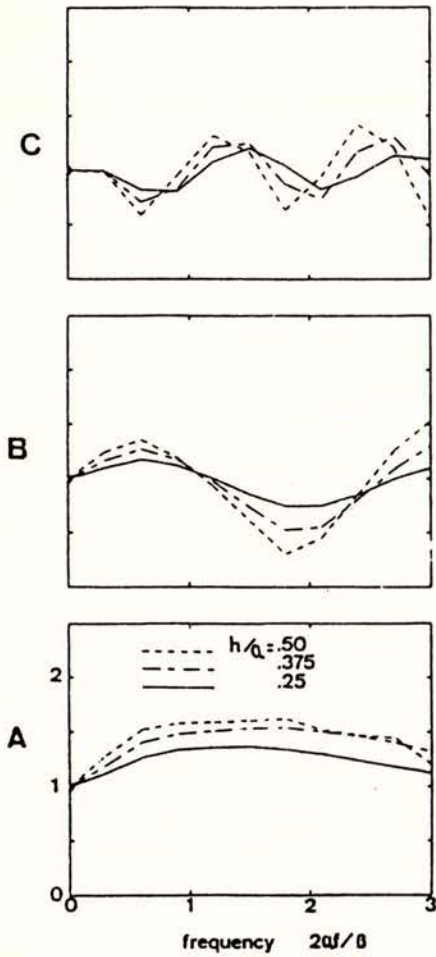
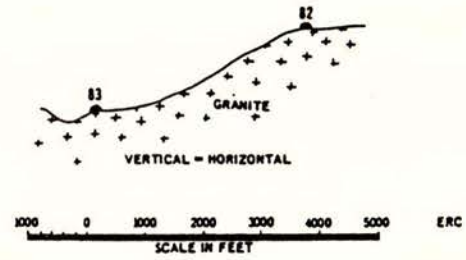
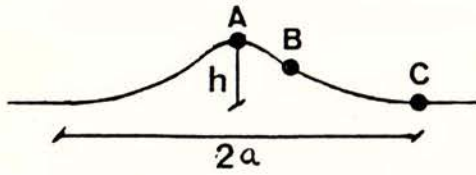


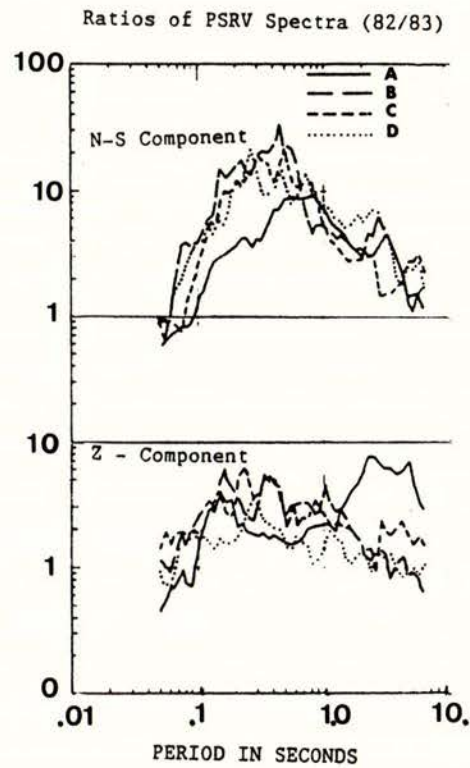
Figure 6: Time domain response of the circular canyon to vertically incident *SH* (top), *SV* (middle for horizontal motion, bottom for vertical motion). Input wavelet is Ricker pulse with central frequency  $\beta/a$ . Small numbers on the top left corner represent relative amplitude units, and those on the top right side, the number of radius 'a' at the left (negative) and right (positive) of the center of the canyon (from Kawase, 1988).



Topography, geology and station (83, 82) location, Kagel Mountain.



a



b

Figure 7: Examples of theoretically predicted (a) and observed (b) topographic effects. A cross section of the topographic feature is shown at the top; the corresponding effects in the frequency domain are shown at the bottom of each figure. PSRV is pseudo velocity spectral ratio.

- (a) shows *SH* response spectra at three sites located, respectively, on the top, mid-slope, and base for three different mountain heights (from Bard, 1982).
- (b) shows ratios of PSRV spectra, top to base, for four different events (A, B, C, D) and two components of motion (from Davis and West, 1973).

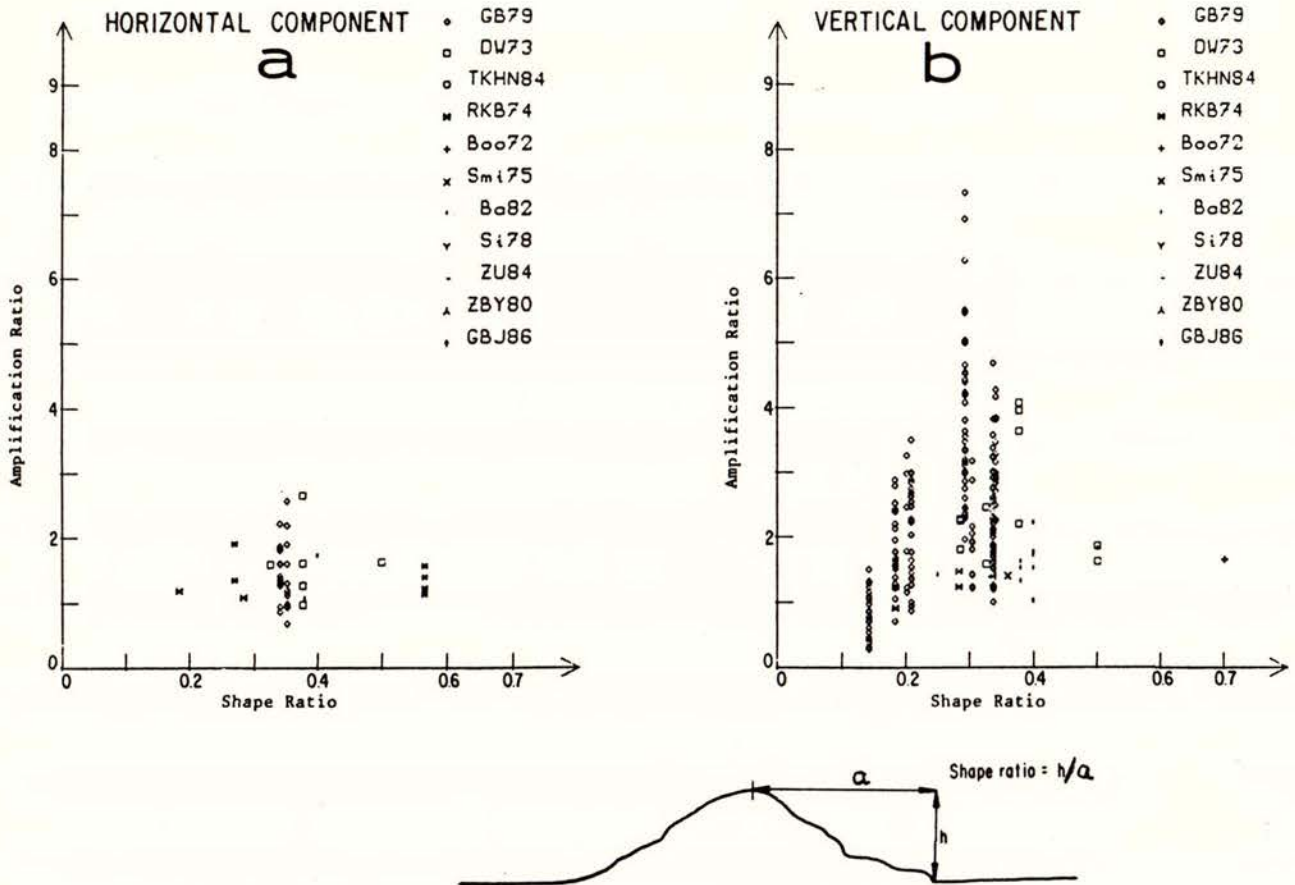


Figure 8: Peak to peak time domain crest/base amplification as reported in the literature, plotted as a function of the shape ratio  $h/a$ . Open symbols indicate experimental field studies, closed symbols indicate results from theoretical studies. (a) horizontal motion, (b) vertical motion. Each symbol correspond to a paper as follows: GB79 = Griffiths and Ballinger, 1979; RKB74 = Rogers et al., 1974; DW73 = Davis and West, 1973; Ba82 = Bard, 1982; Smi75 = Smith, 1975; Si78 = Sills, 1978; TKHN84 = Tucker et al., 1984; ZBY80 = Zhengpeng et al., 1980; Boo72 = Boore, 1972; and ZU84 = Zahradnik and Urban, 1984. (From Geli et al., 1988).

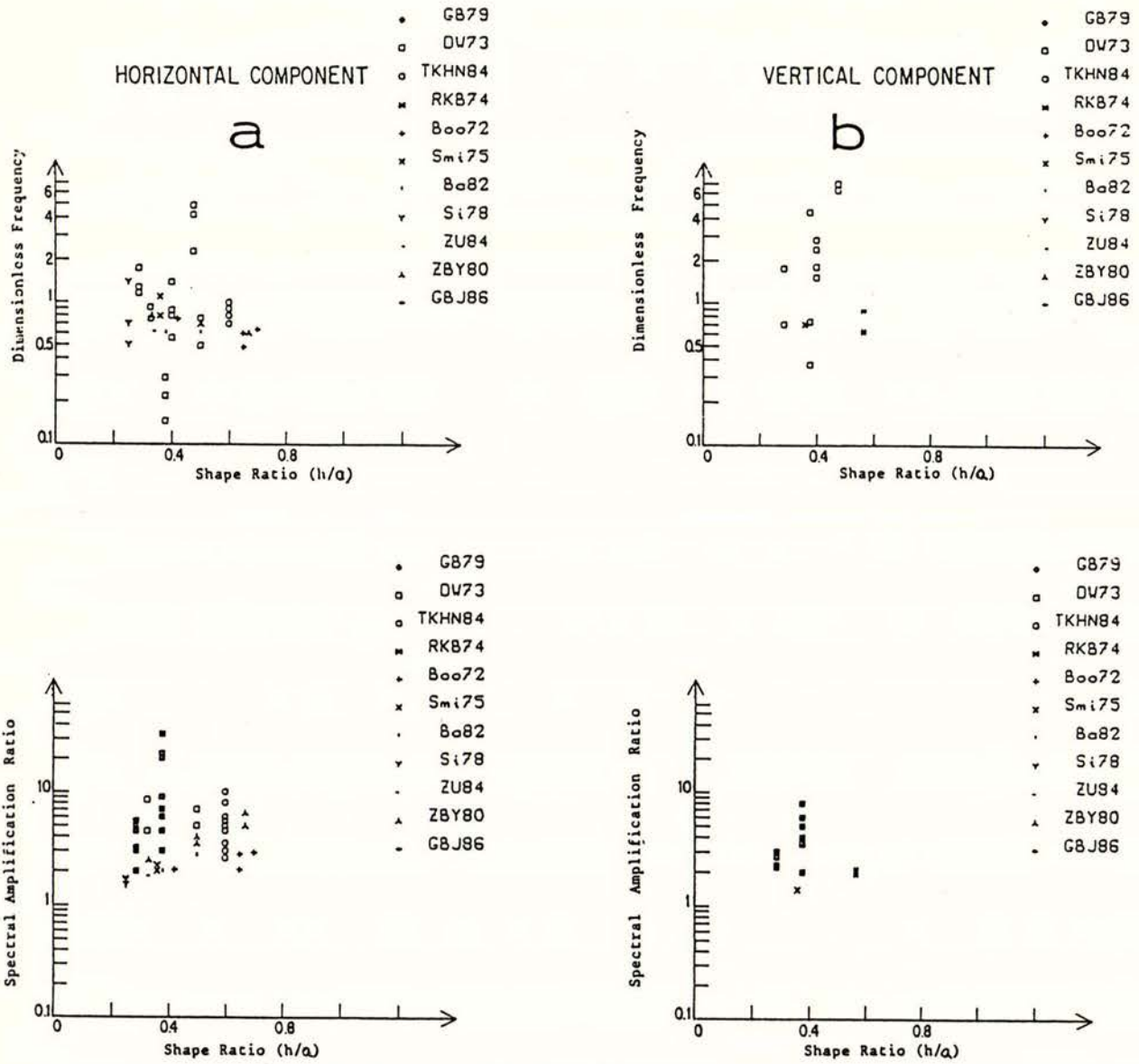


Figure 9: Top: dimensionless frequencies. Bottom: corresponding maximum crest to base spectral amplification peak. Symbols are defined exactly the same as for Figure 8, except for experimental data corresponding to marked 3-D topographies, which are "double". The real frequencies were multiplied, for each case, by  $2 \times 1/\beta$  ( $\beta$  the shear wave velocity). Those values were estimated in the quoted papers (from Geli et al., 1988).

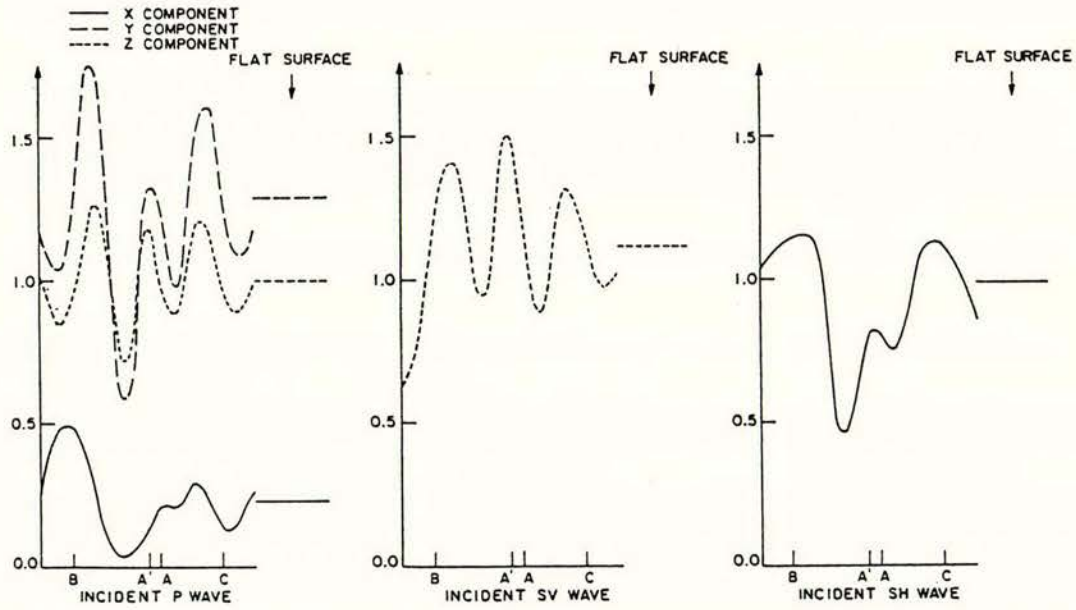


Figure 10: Amplitude of the components of the surface displacement over the Pacoima Canyon for a 2.5 Hz frequency, compared to the flat surface solution. A indicates the position of the accelerograph and A' the bottom of the canyon (from Bouchon, 1973).

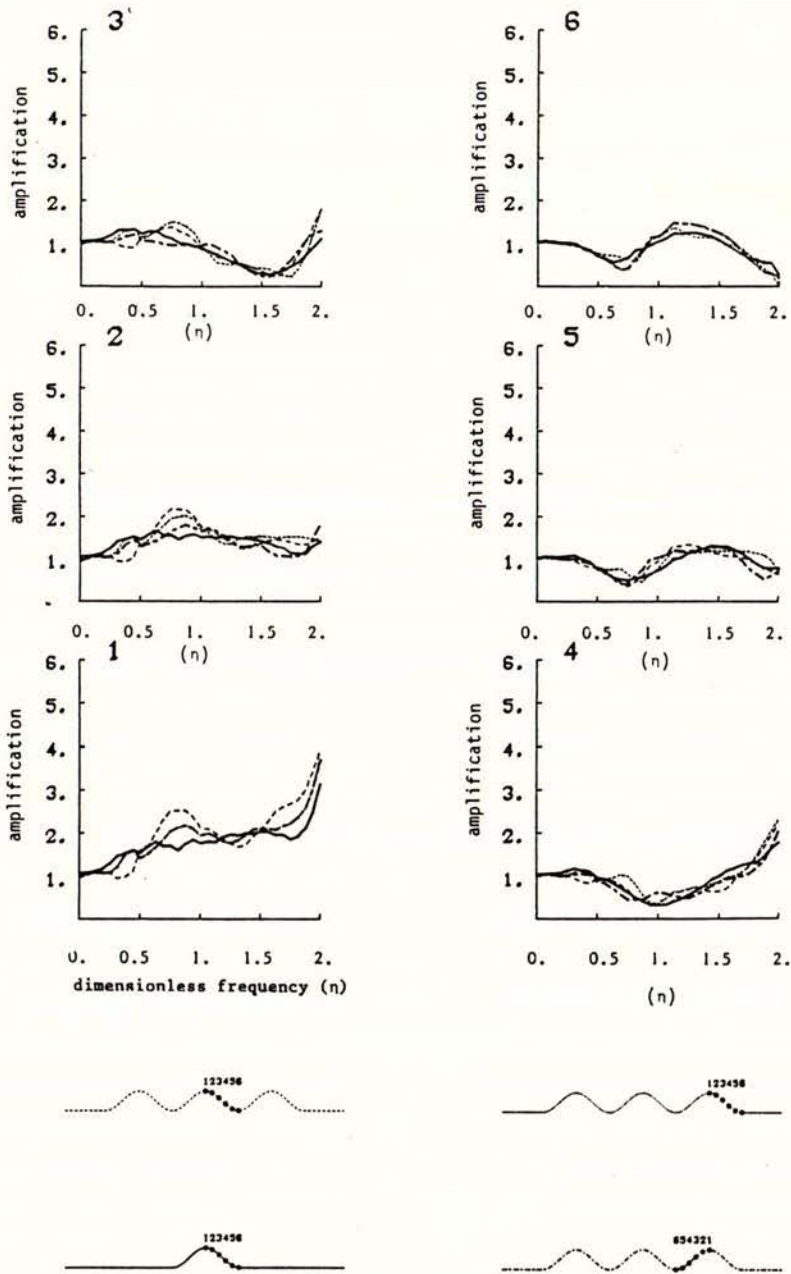


Figure 11: Effect of neighbouring topographies in the case of an homogeneous half-space. The six transfer curves are the *SH* Fourier transfer functions at points 1 to 6, with the line symbol corresponding to the topography depicted at the bottom of the figure. Full thick line = homogeneous multiple ridges; dotted lines = homogeneous multiple ridge with: thin dotted lines = central ridge; thick dotted lines = lateral ridge, inner slope; and thin dotted (with small dots) lines = lateral ridge, outward slope (from Geli et al., 1988).

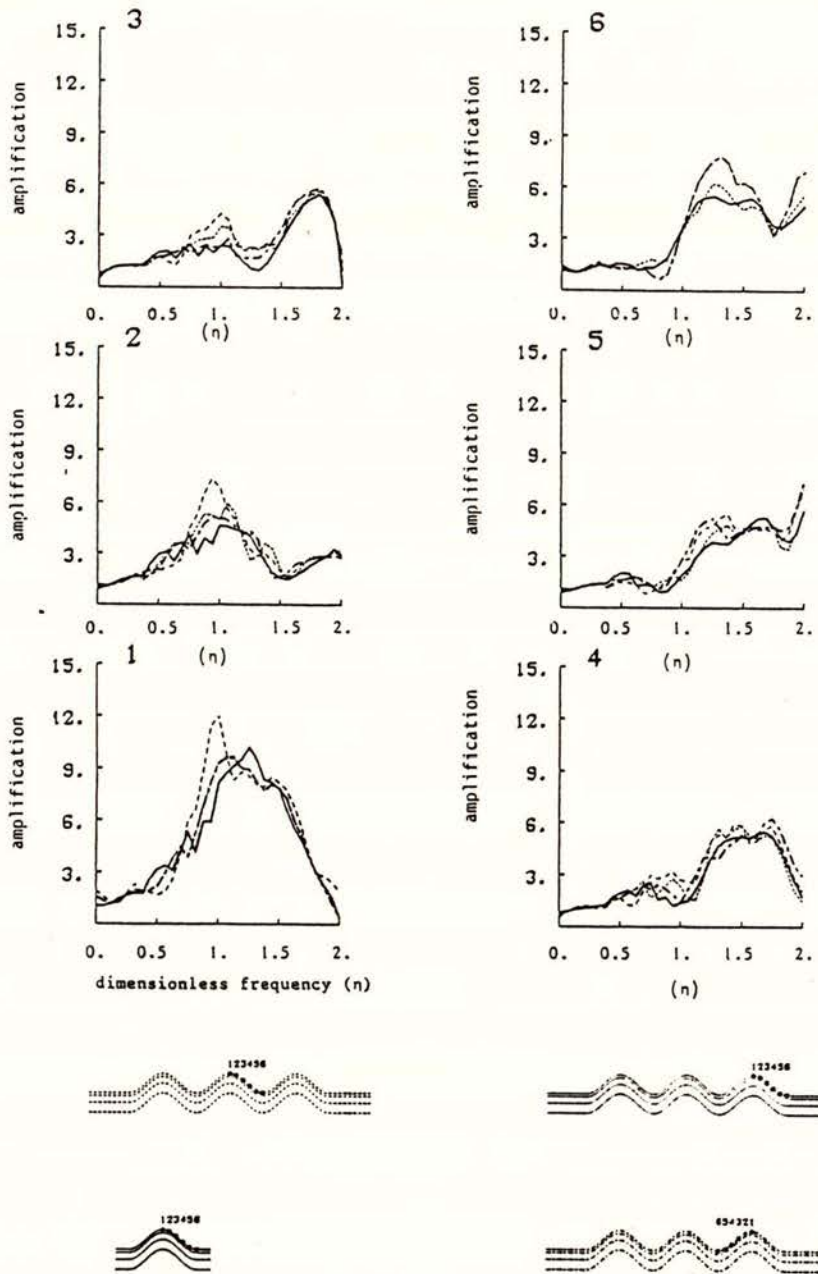


Figure 12: Effect of neighbouring topographies in the case of a layered structure. The explanation for the line symbols are the same as in Figure 10 (from Geli et al., 1988).

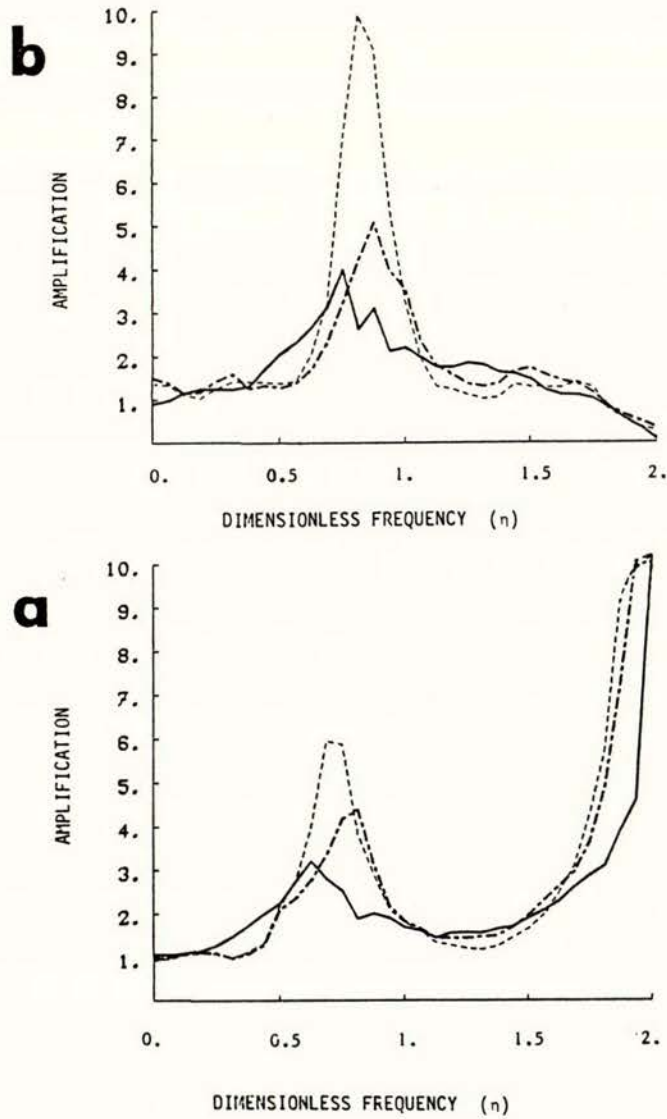
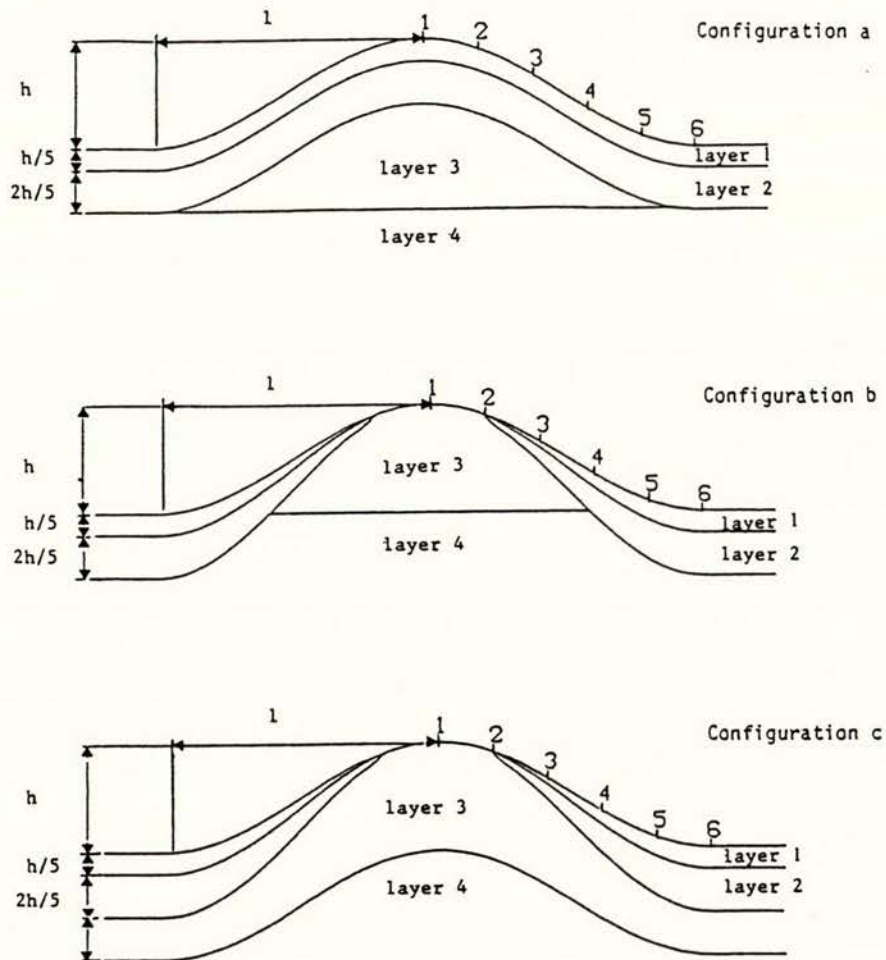


Figure 13: Effect of underground layering and neighbouring topography on crest/base spectral ratios. (a) homogeneous half-space. (b) layered half-space. Thick full lines = isolated ridge; thick dotted lines = multiple ridge, ratio of top of central ridge to lateral base amplification; and thin dotted lines = multiple ridge, ratio of top of central ridge to the next base amplification (from Geli et al., 1988).



	Q	$\rho$ (g/cm <sup>3</sup> )	$\delta$
layer 1	70	2.7	$\delta_3 \times 0.6$ ; $\delta_3 \times 0.4$
layer 2	70	2.8	$0.8 \delta_3$
layer 3	80	2.9	$\delta_3$
layer 4	100	3.1	$\delta_3 \times 1.2$

Figure 14: Cross-sections of the three configurations a, b, and c) selected for investigating the effect of ridge subsurface layering (from Geli et al., 1988).

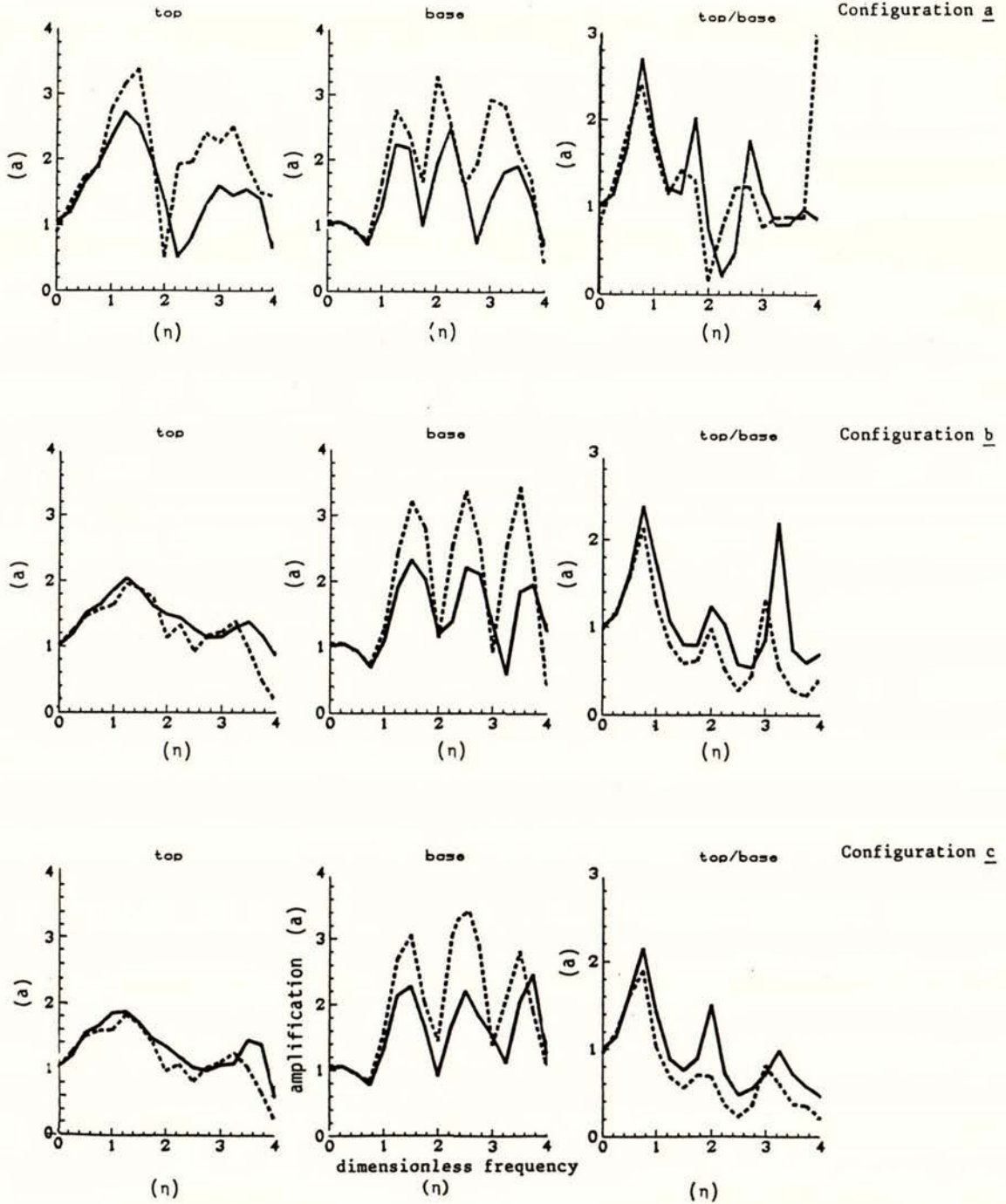
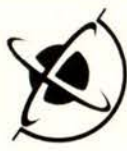


Figure 15: *SH* Fourier transfer functions at the top (left column) and base (middle column) of configuration a (top row), b (middle row), and c (bottom row) of the isolated ridge of Figure 14. In each plot, the thick "full" line corresponds to a surface layer velocity of  $0.6 \beta_3$ , and the dotted line to  $0.4 \beta_4$ . The right column corresponds to the crest/base spectral ratios. (from Geli et al., 1988).

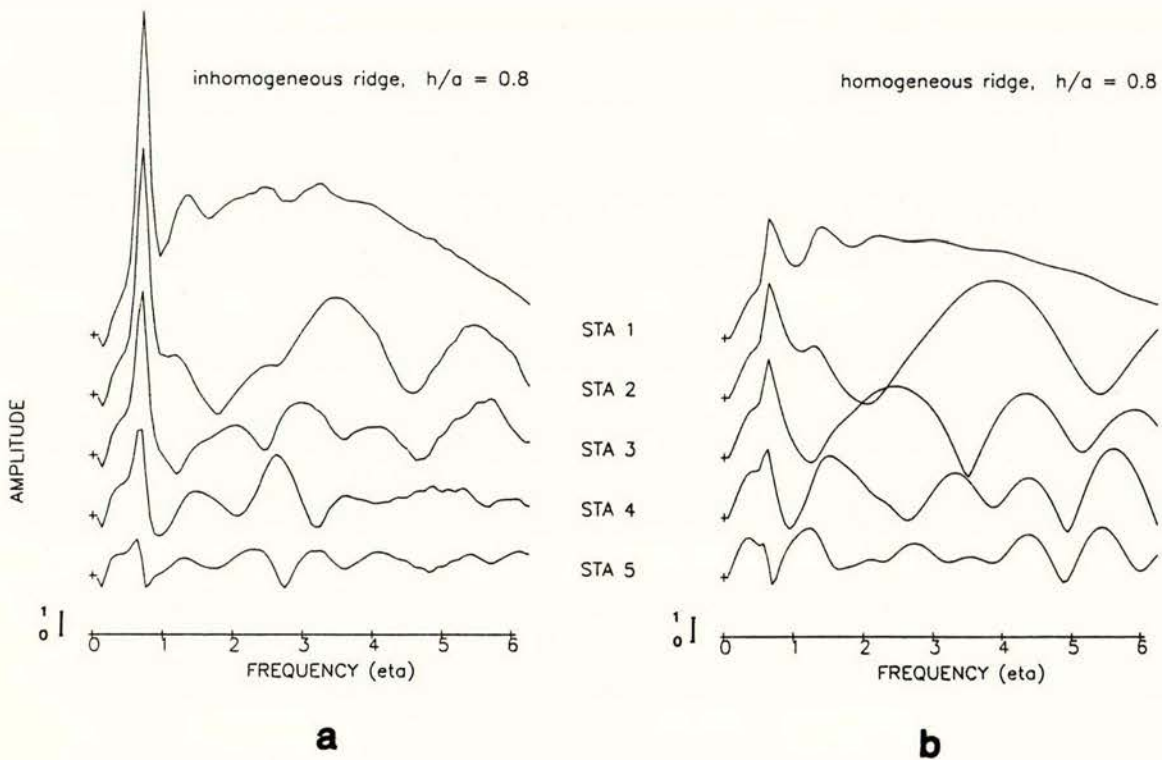
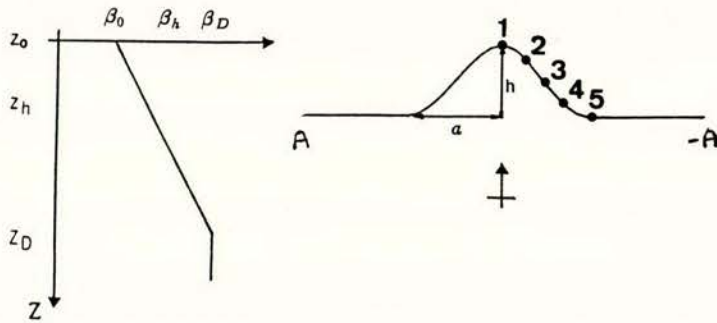


Figure 16: Frequency response of a ridge of shape ratio  $h/a = 0.8$ , for  $SH$  waves vertically incident, at five stations along its flank, from top to bottom. (a) for an inhomogeneous ridge, where the velocity at  $Z_h$  is twice the velocity at the top, (b) for a homogeneous ridge. The velocity at any depth  $Z$  is defined as  $\beta(Z) = \beta_0 + g(Z - Z_0)$ , where  $g$  is the velocity gradient. The non-dimensional frequency (ETA)  $\eta = 2a/\lambda$ , where  $\lambda$  is the wavelength of the incident wave.

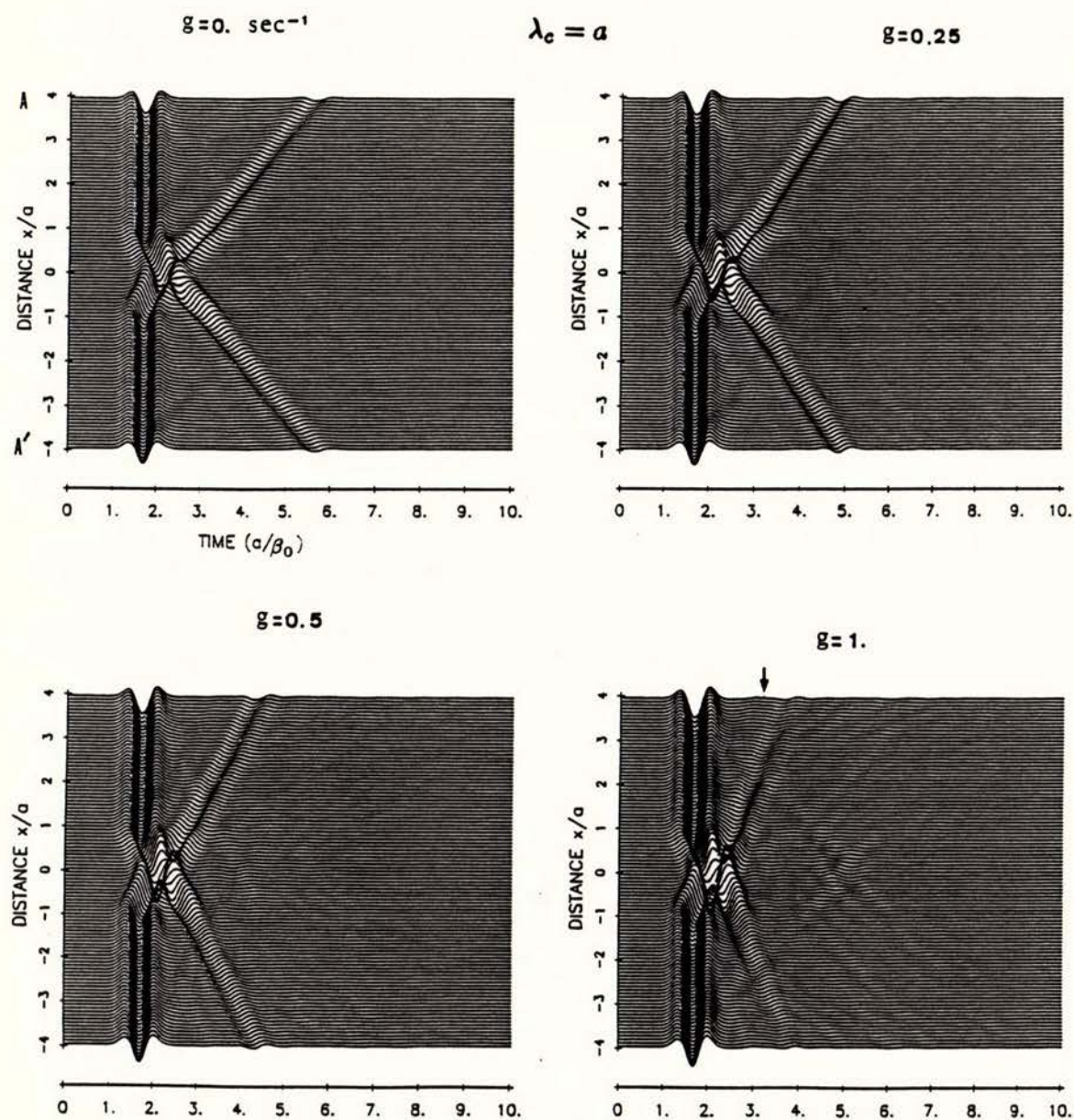


Figure 17: Time domain solutions for a ridge of shape ratio  $h/a = 0.4$ , at 100 stations deployed from A to A' (see figure 16) along the canyon range. The input source-time function is a Ricker pulse of characteristic frequency 1 Hz, corresponding to a wavelength  $\lambda_c = a$ .  $\beta_h$  is fixed to 2 (units of length/sec). For this particular case  $a = 2.5$  (units of length), so that  $g = 0$  implies  $\beta_0 = 2$  (homogeneous),  $g = 0.25$  implies  $\beta_0 = 1.75$ ,  $g = 0.5$  implies  $\beta_0 = 1.5$  and  $g = 1$  implies  $\beta_0 = 1$ , i.e. one-half the velocity at the bottom of the ridge.

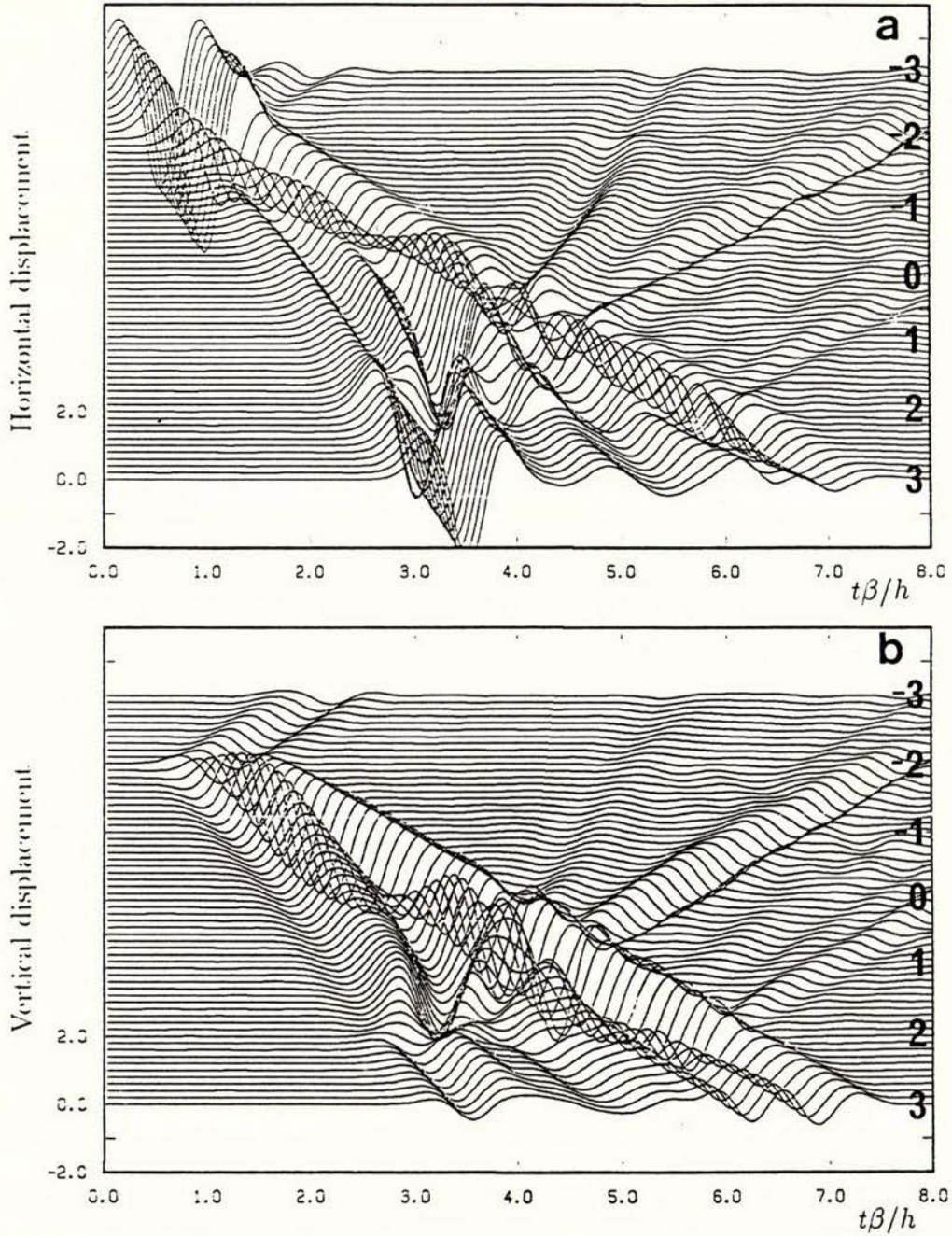


Figure 18: Time responses along the surface of the ridge whose shape is an arc of a circle of radius  $2.5 h$  (where  $h$  is the height of the ridge) to incident  $SV$  waves with  $30^\circ$  angle (which corresponds to the critical angle). Poisson's ratio is  $1/3$ . The characteristic frequency of the Ricker's pulse is 1. (a) horizontal component of displacement, (b) vertical component of displacement (from Kawase, 1988).

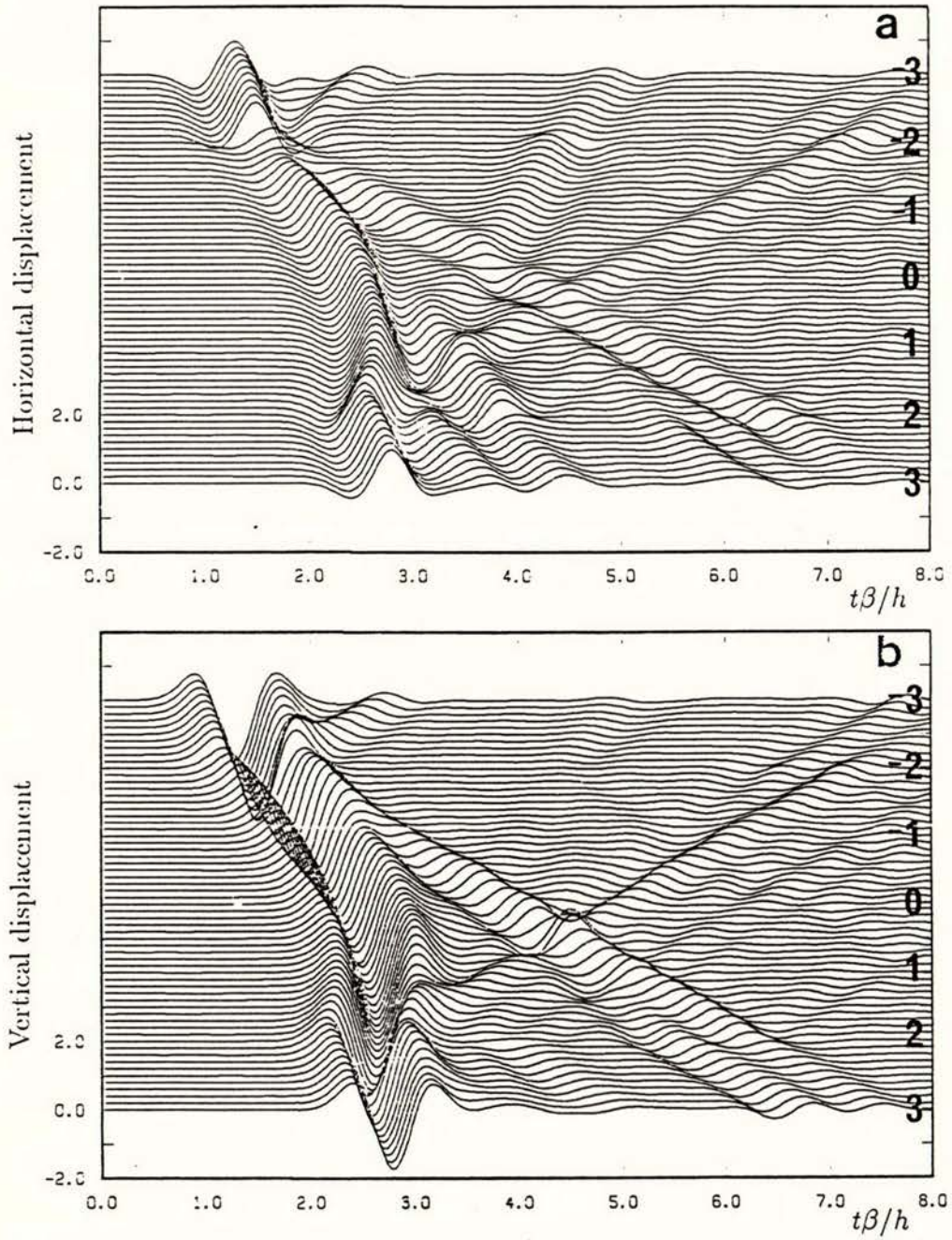


Figure 19: Time responses for incident  $P$  waves with angle  $30^\circ$ . Other parameters in the figure are the same as for Figure 18, (a) horizontal component of displacement, (b) vertical component of displacement.

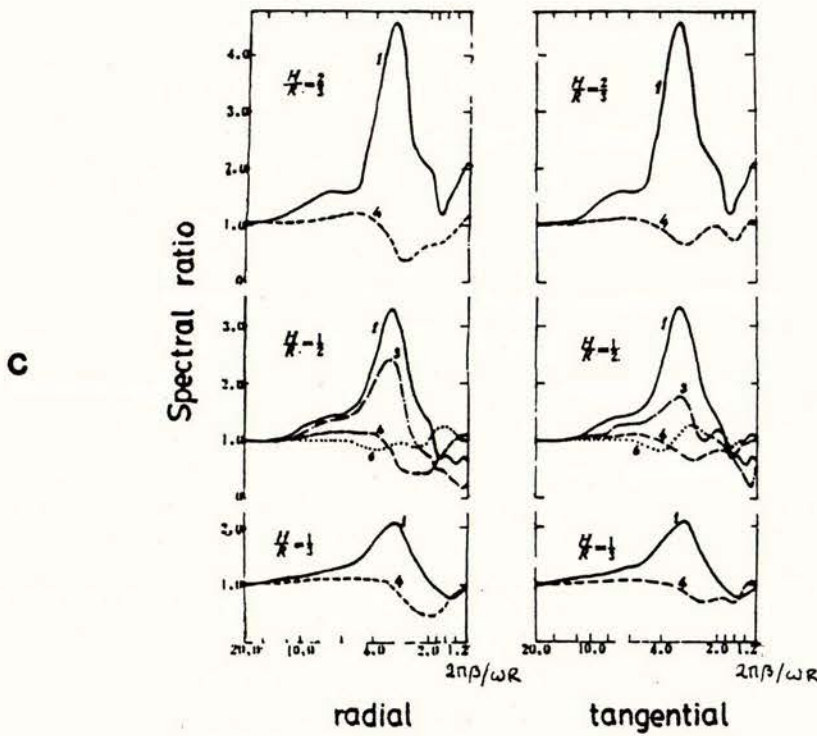
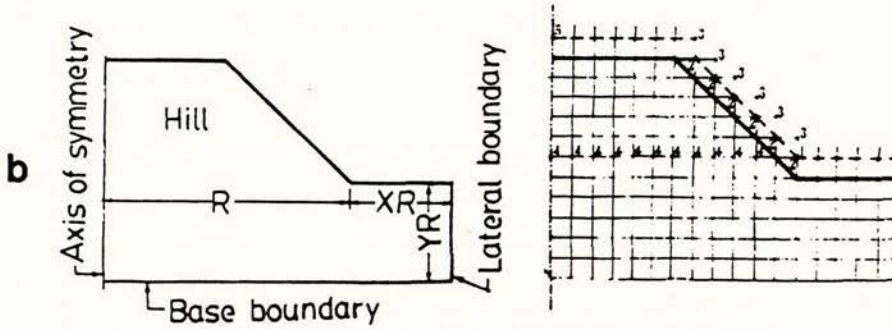
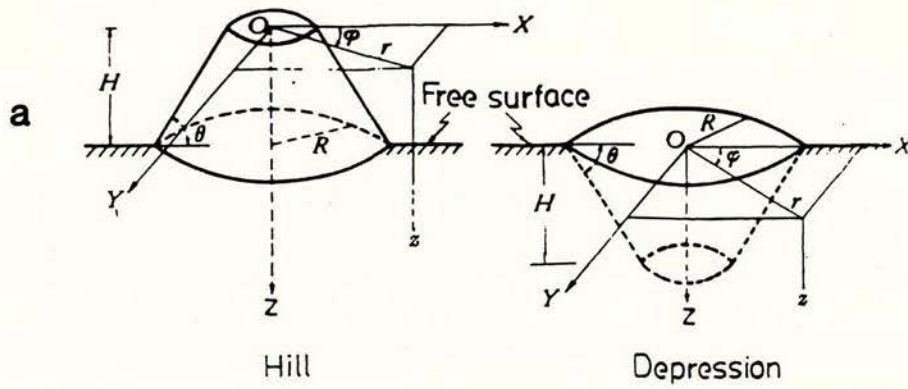


Figure 20: (a) Models of three-dimensional topography, (b) artificial boundaries and fictitious points in the Finite Difference mesh of one-quarter of topography, (c) theoretical spectral ratios at several points on top and flanks of the hill in (b).

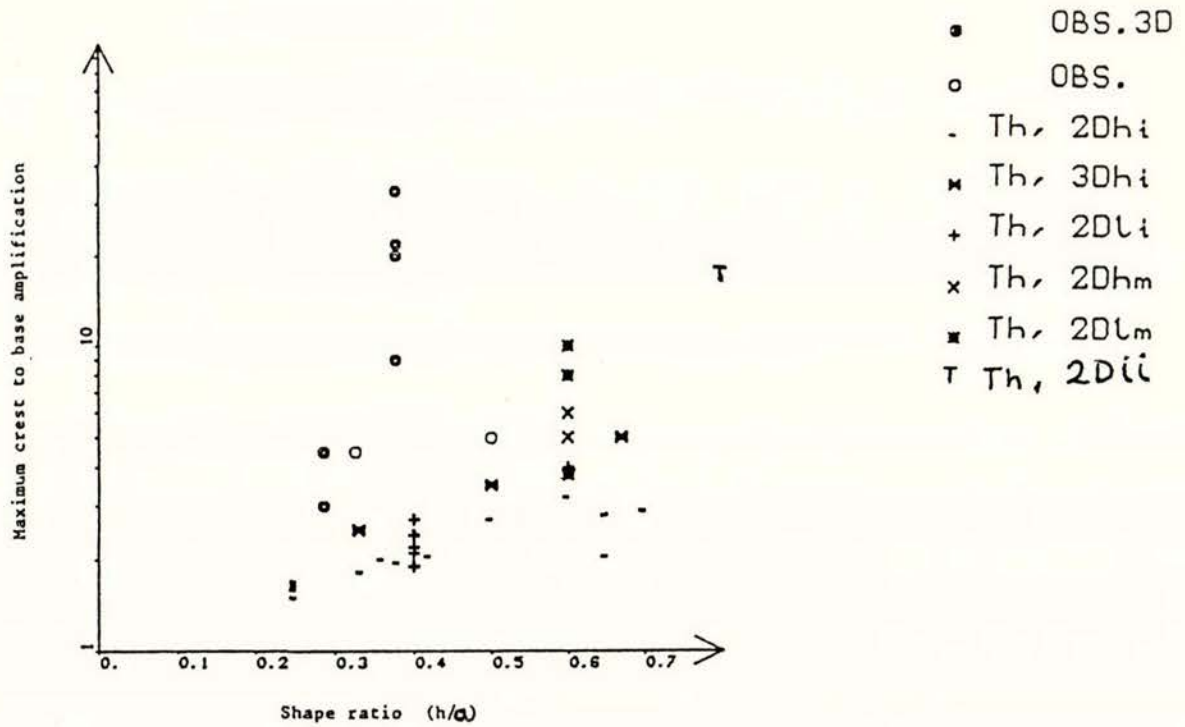
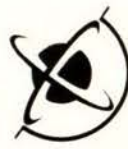


Figure 21: Maximum top/base amplifications for transverse motions, including previous literature results and present results. Open circles indicate observations; "double" circle indicates that the investigated topographies are 3-D. Other symbols h = homogeneous structure, l = layered structure; i = isolated topography; m = multiple topography and ii = vertically inhomogeneous media. The results discussed here correspond to  $h/a = 0.4$  (2Dli),  $h/l = 0.6$  (2Dhi; 2Dlm), and  $h/l = 0.8$  (2Dii).



# **Quantification of seismic wavefield amplification by topographic features**

## **PART II**

### **1. INTRODUCTION**

The results of the two-dimensional (2-D) modelling cases reported in Part I reveal that the complexities assumed for the material properties of hills do not yield significant increases of the computed amplifications at the top, in comparison with those from the corresponding cases with homogeneous material properties. Since these results grossly mismatch some observed amplifications (estimated from spectral ratios) it is suggested that these may be due to either deamplification at the base of the hill, or to three-dimensional (3-D) effects, despite some of the reported observations being made on two-dimensional mountain ranges. Since deamplification at the bottom of the hill is not apparent from the results of the 2-D modelling so far, we extend the study to the cases where the hill is surrounded by basin-like deposits of sediments, in order to analyse the effects of their coupling on the overall response. This includes the cases of constant material properties (Case 1) and varying wave velocities of the media outside the basins (Case 2), in order to account for the possibility of irregular uplift of layers of similar material properties, which may result in resonance. A more complex type of ridge formed by the dipping of two sedimentary irregular layers embedded in an alluvial basin is also considered (Case 3), to account for cases where tilted layers may produce strong focusing effects.

We also address problems of 3-D topographies, by modelling the ground motion of cosine-shaped canyons and ridges upon the impact of plane waves (teleseismic) in order to perform a parametric study of the response in terms of the angle of incidence, shape ratio, frequency and type of incident wave.

The 2-D problems discussed here have been treated with a hybrid method based on the Riccati-Matrix Equation method (Benites and Haines, 1991, Haines, 1989), and the Boundary



Integral method (e.g. Benites and Aki, 1994). The 3-D problems were treated with a boundary integral scheme based on artificial wave source distribution over an extended area covering the irregular topography.

## 2. 2-D MODELLING

In this section the predicted ground motions for the 2-D models described above are presented in terms of both frequency response computed at several recording points (or stations) along the spatial range of the models, and synthetic seismograms. These seismograms are computed from the synthesis of 100 complex valued frequency responses along the spatial range of the models, using a Ricker wavelet as source-time function whose peak frequency is 1.5 Hz, unless specified otherwise. For Cases 1 and 2 a parametric study considering several types of incident waves, several angles of incidence, three components of motion and 100 stations along the range where the motion is computed, yield large amounts of data. To best describe them the frequency responses are given without specifying the position of the stations, except for the one that yields the maximum amplitude for a particular component of motion. In this way the general features of the responses can be analysed. Later in the section some details of amplification at particular positions will be discussed. For Case 3 the analysis in the frequency domain is done for three particular positions within the range. Finally, for the three-dimensional cases the results are given only for the spatial distribution of ground motion for prescribed frequencies.

### 2.1 Case 1

Consider the stratigraphy depicted in Figure 1, consisting of a hill flanked by two small basins, extending over 10 km. The height of the hill is 1 km, with shape ratio (i.e. the ratio of height to half-width at its base) equal to one. The maximum depth for each basin is 250 metres. The material properties of the hill and bedrock are density  $\rho_2 = 1.5 \text{ g/cm}^3$ ,  $S$ -wave velocity  $\beta_2 = 2 \text{ km/s}$  and  $P$ -wave velocity  $\alpha_2 = 3.5 \text{ km/s}$ . For both basins  $\rho_1 = 1 \text{ g/cm}^3$ ,  $\beta_1 = 1 \text{ km/s}$ ,  $\alpha_1 = 1.73 \text{ km/s}$ . Figure 2 shows the response to a vertically incident  $SH$  wave, for up to



3 Hz. The geometry has been divided into three regions; regions 1 and 3 containing the basins to the left and to the right of the hill, respectively, and region 2 containing the hill. The responses are given at 9 stations distributed uniformly along region 1, one being set off the axis (at  $x = -1$  km) to represent the half-space without the model, 5 stations being set within region 2 and 8 stations within region 3. The amplitudes of the responses are given in terms of non-dimensional values corresponding to normalisation with respect to the response of a half-space with flat free-surface without the topography (a factor of 2). The actual units for the computed amplitudes are the same as those of the amplitude of the input wave, and we will refer to them either as 'units of amplitude' or simply by giving their absolute value.

A dominant feature in Figure 2 is that the largest amplitude occurs in the region 1, of up to 8.6 units of amplitude (or  $2 \times$  the value 4.3 in the figure) at the station located at  $x = 3.5$  km, for frequency  $f = 1.71$  Hz. To a lesser degree, the stations on the hill also yield high amplitudes, of up to 5.2 at  $x = 5$  km (top). The variability of the responses with frequency along the basins is remarkable, compared with those on the hill which yield rather flat spectra. In terms of the non-dimensional frequency  $\eta = \text{base width}/\lambda$ , our 3 Hz maximum frequency corresponds to  $\eta = 6$ . Taking this into account, the response of the hill resembles that of the examples shown in Figure 10 of Part I.

Figure 3 shows responses in the time domain computed at 21 stations distributed uniformly along the 10 km range. In addition, we have included two stations on each side of the range outside the basins, to account for the phases travelling away from the model. The total duration of the seismograms is 20 seconds. It is observed that the incident wave is amplified about 2.5 times at the station on the top of the hill, and reflected away from the hill, propagating horizontally throughout the basins (marked with ' $S_L$ ' in the figure). In general, the seismograms of the stations within the hill are of relatively short duration. These suggest that there is a lack of strong multiple reflections within the hill, and that the computed amplification at the top is mainly due to single scattered waves which originated at the base of the hill. The later arrivals, of relatively small amplitude at these stations, are likely to be due to diffraction of waves originating in the basins. On the other hand, the long duration and large amplitude seismograms at stations within the basins suggest resonance, but it must be



pointed out that for region 1 the larger amplitudes do not occur at the center of the basin where the depth is maximum, but rather close to the hill (this is true also for the frequency response). This fact, and the propagation of a wave reflected from the hill horizontally towards the stations outside the range, determine the coupling between the hill and the basins. Note that  $S_L$  is not only transmitted away from the range, but is also reflected at the edges of the basins, contributing to their amplifications. The case of a vertically incident plane  $P$  wave is shown in Figures 4 and 5, for frequency and time domains respectively, also normalised with respect to the response of a half-space without the topography (a factor of 2). Figure 4(a) shows that the larger amplitudes for the horizontal component of the motion occur in the basins, as in the previous case, although the maximum value ( $2 \times 2.3 = 4.6$  at 3.5 km for 2.25 Hz) is about one half of that for the  $SH$  case. The responses along the hill yield flat spectra, with a maximum value of 2.4 for 1.8 Hz. The variability of the response is large within the basins, but in region 1 the response decays abruptly towards the end of the basin. This suggests significant wave conversions taking place at the edge of the basin opposite to the hill. This is not apparent in the basin of region 3, where such decay appears quite smooth. The maximum amplitude of the vertical component  $U_z$  (Figure 4(b)), of about 10.8 at  $x = 2.5$  km, for  $f = 1.77$  Hz, is significantly larger than that of  $U_x$ . The abrupt decay observed for  $U_x$  in region 1 is also observed here, but for stations closer to the center of the basin than towards its edge. It is of interest that the maximum amplitude for each component occurs at a different frequency, and that the frequency of maximum amplitude of  $U_z$  is similar to that of  $SH$  in Figure 2 (see also Table I). Again, the spectra on the hill appear quite flat, with no particular distinction among stations. The synthetic seismograms in Figure 5(a) show that the horizontal component cancels out at the top of the hill, in spite of the asymmetry introduced by the basins. Only weak secondary arrivals appear, resulting from its interactions with the basins. The synthetic seismograms for component  $U_z$  (Figure 5(b)) show that resonance occurs at both the center of the basin in region 1 and at 7 km in region 3. At the top of the hill the incident wave is amplified by a factor of 1.5. From both seismogram sections it appears that the waves propagating from  $x = 2.5$  km in region 1 and from  $x = 8$  km in region 3 towards the ends of the range are dispersive, with both components  $90^\circ$  out of phase, suggesting Rayleigh waves travelling away from the model as a result of  $P$  wave impact.



Figures 6 to 11 correspond to the cases of an  $SV$  plane wave vertically incident, an  $SV$  incident at  $75^\circ$ , and a Rayleigh wave incident, upon region 1, for frequency and time responses. The description of the results follows that from the previous cases, and we refer the reader to Table I (homogeneous) for the peak amplitude values and their corresponding positions and frequencies, in each case. We describe here only the most salient features of these results. The seismograms in Figures 7 (a) and (b) for a vertically incident  $SV$  show that the waves travelling away from the basins do not exhibit dispersion, as happened in the case of  $P$  incidence, but rather show body  $P$  and  $S$  waves converted/transmitted at the edges due the incident wave, and to multiple bouncing of trapped waves within the basins. The seismograms for  $SV$  incident at  $75^\circ$  (Ricker wavelet peak frequency = 1.04 Hz) show strong reflected body  $S_p$  and  $S_s$  waves in region 1 (Figure 9(a)), while the wave emergent from region 2 may correspond to a Rayleigh wave ( $S_r$  in Figure 9(b)). Rayleigh waves incident upon region 1 reflect weak  $P$  waves and strong Rayleigh, while strong  $P$  and Rayleigh emerge from region 2 ( $R_p$  and  $R_r$  in Figures 11 (a),(b)), where  $R_p$  means incident Rayleigh wave converted into  $P$  wave, and so on.

The computations of ground motion so far may raise some questions about the estimation of amplification factors from spectral ratios using teleseismic waves. For instance, if amplification factors for the hill were to be computed from spectral ratios with respect to stations in region 1, the results will depend strongly on the reference location. For example, let us take the case of the vertically incident  $SV$  wave, in Figure 6(b). In the frequency range of 2 to 3 Hz, the stations at the edge of and outside the basin, which presumably are dominated by the incident wave rather than by the effects of the basin, yield flat spectra with values varying from about 0.2 to 0.1. For the top of the hill, whose amplification values vary from about 1 to 2.8, the spectral ratios yield factors for the vertical motion between 5 and 28. Note that this will happen even if the reference spectrum is smoothed. Clearly, the problem boils down to either identifying the frequency content of the source, in which case near-to-middle field sources may be more appropriate, or to use a large time window of the seismograms, which may have the disadvantage of contamination by other nearby site effects. On the other hand, teleseismic waves may be convenient for reverse situations; that is, when



the amplification factors of the basins are to be found from spectral ratios using the hill (outcrop) as reference. The reason is because, as observed in our calculations so far, and in the ridge models reviewed in Part I, the response of a hill over a half-space is not strongly affected by heterogeneities outside it. In other words, the variability of the response over an isolated hill (flanks and top) does not change dramatically in the presence of other stratigraphic features around it. Having one of these seismograms as reference, the effects of the hill can be easily modelled and removed from the data, yielding a seismogram that reflects the source and/or path effects more accurately.

The effects of heterogeneities within the hill on the hill's response have not been fully studied at present. In the next case we address some examples to this subject.

## 2.2 Case 2

In this case the geometry of the problem (Figure 12) is exactly the same as that for Case 1, but the  $S$ -wave velocity of the bedrock varies along the range and with depth, so that its value at a reference point  $x = 5$  km,  $z = 2.5$  km is  $\beta = 3$  km/s. Contour lines through points of the inhomogeneous bedrock having the same  $S$ -wave velocity are depicted in Figure 12. We constrain our analysis to the case of incident  $SH$  waves only. The effects introduced by the inhomogeneity of  $S$ -wave velocity are quite strong in both the frequency and time domains, but not dramatic. This may be due to the fact that the density and the  $S$ -wave velocity of the bedrock at the bottom of the basins are still the same as those at the top of the hill, so that the impedance contrast along the boundaries of the basins and the bedrock is still the same as it was in Case 1. It is the velocity at deeper points in the bedrock which increases, introducing the effect of focusing the incident seismic energy. Comparing the response with its corresponding homogeneous case (Figure 2) and referring to Figure 13, and to Table I, the values of its maximum amplitude, frequency and position are 13.6, 1.8 Hz and 3.5 km, respectively. The variation with frequency of the response on the hill is smaller in this case; the station right on the top becoming almost indistinguishable from the others. The variation of the response in the basins remains almost unchanged with respect to the homogeneous case, except that the resonances are well defined and the amplitudes larger, being up to 14 for



the basin in region 1. The synthetic seismograms in Figure 14 show that the pulses within the basins appear strongly amplified, by a factor of 2, with respect to the corresponding traces in Case 1 (Figure 3). The seismograms are of higher frequency content than those for the homogeneous case (e.g. compare traces at 2, 2.5, 8, 8.5 km) and of longer duration. In general, it appears that the effect of the *S*-wave velocity inhomogeneity is to enhance the resonances in the basins, without shifting either the positions or the frequencies of the maximum amplitudes. The seismograms at stations outside the basins, in the half-space, show the arrivals (with arrows) of the first waves reflected at the basin-bedrock boundaries, and of the waves that propagate horizontally from the hill throughout the basins, at earlier times than those corresponding to the case of homogeneous *S* wave velocity. In addition, a train of phases of similar waveforms but of decaying amplitudes arrives at intervals of about one second. These phases are not observed in the case of homogeneous *S* wave velocity, and are due to multiple bouncing in the inhomogeneous medium close to the surface. On the top of the hill the incident pulse is amplified by a factor of about 2.7, slightly higher than it was in the homogeneous case. The seismogram shows the arrival of waves back-scattered in the basins more clearly than the homogeneous case, although it remains of short duration. The response to an *SH* horizontally incident at  $+90^\circ$  is shown in Figure 15. The amplitudes over the hill are about the same as those for vertical incidence, exhibiting similar variation with frequency. On the other hand, the amplitudes are significantly larger at all stations within the basins, of up to 20.6 for 1.77 Hz, at  $x = 3.5$  km in region 1. The corresponding seismograms in Figure 16 show slight amplification of the incident wave at the top of the hill, of about 1.3 times, exhibiting significant distortion of the wavelet compared with vertical incidence. The seismograms in the basins show resonance, with peak-to-peak amplitudes between three to four times larger than the incident wave at  $x = 3$  km in region 1, and at  $x = 7.0$  km and  $x = 7.5$  km in region 3.

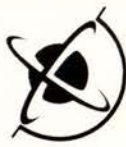
### 2.3 Case 3

Referring to Figure 17, let us consider a ridge formed by two dipping irregular layers of gravels within a sedimentary basin. The whole geometry extends over 2 km, with maximum depth of 500 m. The ridge rises 100 metres above the flat free-surface. The stratigraphy is



formed by four layers numbered from 1 to 4, over a half-space (bedrock), numbered 5; with all layers exhibiting inhomogeneous material properties as listed on the sides of the model in Figure 17. The symbol  $Q$  stands for the quality factor, which is input in the model for both  $P$  and  $S$  waves. As an example, Figure 18 shows contour lines corresponding to variations of  $S$ -wave velocities between 0.2 km/s and 0.25 km/s in layer 1, and 1.2 km/s and 1.5 km/s in layer 4.

Computations of the ground motion for vertically incident plane  $SH$ ,  $P$ , and  $SV$  waves are shown in Figure 19, normalised to the response of the flat-free surface half-space without the basin, and for a single input frequency of 2.5 Hz. The motion was also computed along 1 km of the flat free-surface extending over each side of the basin, to account for the incident wave plus waves reflected/transmitted away by the model. The maximum amplitude of the motion over the hill is not larger than 4, or twice the input amplitude. For incident  $P$  there is no amplification for the horizontal component  $U_x$ , in spite of the irregularity of the medium. Figures 20 (a) and (b) show the ground motion for  $60^\circ$  incidence and for  $SH$  and Rayleigh waves incident at  $\pm 90^\circ$ , respectively. In general, the motion on the ridge is significantly smaller than that on the horizontal deposits for all the incident waves considered, and large amplitudes up to 24 ( $2 \times 12$ ) occur at stations on the sediments close to the left edge of the basin and close to the base of the ridge, for  $SH$  waves at horizontal incidences. For these cases we compute the frequency response at a total of nine stations, distributed as follows: three outside the basin, towards the left, three within the basin, at 0.2 km, 1.0 km and 1.8 km, labelled stations 1, 2, 3 respectively, and three outside the basin towards the right. Results are shown in Figure 21, for incident angles  $+90^\circ$  (top) and  $-90^\circ$  (bottom). Spectra are given for a frequency range from 0 to 4.78 Hz. The latter value corresponds to an input wavelength  $\lambda = 0.52$  km in the bedrock ( $\beta = 2.5$  km/s), which in turn corresponds to four wavelengths within the range. On the surface over the sediments ( $\beta = 0.2$  km/s) that is equivalent to 47 wavelengths, and over the ridge ( $\beta = 0.7$  km/s) to 14 wavelengths, along the range. Only the responses within the basin are identified, as indicated in the top right of the figure, because of their large variability with frequency. The maximum amplitude occurs at station 2, of up to 20 ( $2 \times 10$ ), for  $f = 0.32$  Hz, and for  $-90^\circ$  incidence. The sharpness of the peak suggests



resonance due to waves propagating through regions of low attenuation within the medium. At the same frequency the responses of the stations outside the basin on the left, and the response of the station 3 (on the ridge) are much smaller than the maximum amplitude, which implies that resonance is occurring mainly within the horizontal deposit of sediments (layers 1 and 2 in Figure 17). The corresponding wavelength is 0.625 km on the surface, or about one-half the size of layer 1, suggesting that the resonance is mainly due to waves propagating horizontally within it. The response of the basin to an incident Rayleigh wave (half-space) at  $+90^\circ$  is shown in Figure 22, for up to 1.6 Hz. The labels are the same than those for Figure 21. As in the previous case, the maximum amplitudes are larger at station 2 than those at any other station, for both components of motion. No sharp peaks are observed, and the frequencies of the two largest amplitudes are around 0.50 Hz and 0.64 Hz, respectively. In both examples the responses on the ridge yield flat spectra with low amplitudes and, in general, their character is similar to that of the responses of hills described in the previous section.

To illustrate the complexity of the wave propagation for this Case 3, we have computed the synthetic seismograms for all the incident waves mentioned above, and for 120 receivers at the surface, covering 2 km of the half-space on each side of the basin (a total of 6 km). These are shown in Figure 23 (a)-(d). In general, the common feature in all the seismogram sections is that the motion is concentrated mainly within 0 and 1.2 km, that is in the part of the basin between the left edge and the base of the ridge. In comparison, the motion over the ridge (from 1.2 km to 2 km) is small, and of short duration. From these figures, let us discuss the dependency of the time response on the type of incident wave and the angle of incidence. In the case of a vertically incident *P*-wave (Figure 23 (a)) the waves reflected/converted at bottom of the basin in the bedrock arrive with negligible amplitudes at stations outside the basin. Inside the basin, between its left edge and the base of the ridge, the motion appears to be dominated by body waves travelling in opposite directions during the first five seconds after the arrival of the incident wave ( $t \sim 4.5 \times 2 = 9$  sec in the figure). After the 9-th second the motion becomes rather coherent; all stations within that range exhibiting about the same amplitude of horizontal component ( $U_x$ ). The vertical component ( $U_z$ ) appears to cancel at



several stations after 10 seconds, but displaying similar coherent pattern. Travel times for both components suggest that the velocities of the waves travelling back-and-forth for the vertical component are slower than those for the horizontal. An *SV* wave vertically incident, i.e. with particle motion polarised along the *X* direction (Figure 23(a), bottom) is strongly attenuated at stations along the basin, but generates body waves of amplitude about four times larger than those for an incident *P* wave during the first eight seconds after its arrival. The waves generated towards the base of the ridge are of significantly larger amplitudes than those generated at the left edge of the basin, in particular for the horizontal component (up to three times). At stations close to the base of the ridge the first onsets after the incident wave arrive almost in phase, suggesting focusing induced by the dipping layers. Since the incident wave is purely horizontal, and the horizontal component does not cancel at any station in this region, the motion appears to be dominated by the waves which originated at the base of the ridge travelling in one direction, back-and-forth. The coherency patterns shown by these seismograms, for both components, are similar to those described for the *P* incidence, except that in this case coherence appears at about 12 seconds. It is interesting to note that the inclined incidences of *P* and *S* waves (at  $60^\circ$  and  $30^\circ$  from the right side, respectively, (Figure 23 (b)) generate larger amplitudes than those at vertical incidences at all stations on the sediments, suggesting stronger resonance. The description of the propagation for Rayleigh (Figure 23 (c)) and *SH* (Figure 23 (d)) horizontal incidences follows the context of the previous cases in regard to amplitudes and coherence patterns. It is worth mentioning that it is not possible, without a thorough analysis of particle motion, to conclude whether the motion in the basin after the 10-*th* second is dominated by body waves or by surface waves. Also, the largest amplitudes among these cases correspond to an *SH* wave horizontally incident from the right side of the basin (Figure 23 (d)), at stations close to the base of the ridge. We select this particular case to analyse the maximum amplitude of ground motion for several input frequencies. Referring to Figure 24, we compute 10 seconds of synthetic seismograms at 11 stations along the same range of the previous cases. We choose four values for the breadth of the Ricker wavelet;  $t_b = 1.1, 0.55, 0.36667,$  and  $0.275$  seconds, corresponding to peak frequencies  $f_p = 0.71, 1.42, 2.13$  and  $2.84$  Hz, respectively ( $f_p = \sqrt{6}/\pi t_b$ ). We observe that the maximum amplitude occurs at the station located at 1 km (labelled 'station 2' in Figure 21) for



these four frequencies. But the most interesting feature is that the value of maximum amplitude increases with frequency, peaks at 1.42 Hz, and then decreases with frequency. On the other hand, the duration of the seismogram at this station decreases uniformly from the lowest to the highest frequencies.

### 3. 3-D MODELLING

Consider the topographic features depicted in Figure 25, corresponding to a cosine-shaped 3-D canyon (top) and to a hill, or mountain (bottom) defined in a 31 km by 31 km square area. Both features are of square shape at their base, of side  $2a$ , extending between 10 km and 20 km within the larger area ( $a = 5$  km), in both the directions of  $X$  and  $Y$ . The reasons for choosing this square geometry are two; the first, which is of concern here, is to allow the comparison of the responses at different 2-D profiles parallel to the sides of the square without changing the relation of input wavelength to the base width of the mountain. The comparisons will thus emphasise the dependence on depth (or height for the mountain) at constant frequency. In this sense, comparisons with similar 2-D models by Bouchon (1973) will be possible. It can also allow the choice of profiles along the diagonals passing through the center, for instance, so that the relation of input wavelength to the base width will change. Finally, it will allow us to check the effect of the azimuth of the incident wave. The second reason is because it is the most suitable geometry to combine the Boundary Integral solution with that of Riccati Matrix Equation (Benites and Haines 1991, Haines 1989) to incorporate 3-D basin structures, which will be done in future studies. The maximum depth (height) is 3 km, at the center of the square, i.e. at  $x = 15$  km and  $y = 15$  km. The grid points at which the ground motion is computed are defined by 100 lines regularly distributed between 0 and 31 km along each axis. The incident wave considered in all examples that follow, corresponds to a plane wave, defined with respect to a Cartesian coordinate system  $E$  (for East),  $N$  (for North) and  $Z$  (for depth, positive down), with  $E$  and  $N$  oriented in the direction of  $X$  and  $Y$ , respectively. The incident plane wave is contained in a plane defined by the azimuthal angle  $\phi$ , measured clockwise from  $N$ , and by  $Z$ , henceforth called azimuthal plane. The particle motion of the incident wave is defined as follows: contained in the azimuthal plane for an  $SH$



wave, perpendicular to the azimuthal plane for an  $SV$ ; and in the direction of the angle of incidence with respect to the vertical  $\theta$ , for a  $P$  wave. The frequency of the incident wave is given in terms of a non-dimensional frequency  $\eta$  defined as  $\eta = 2a/\lambda$ .

### 3.1 Mountain

Results for the case of a mountain upon the impact of vertically incident  $P$  wave are shown in Figure 26. These correspond to the three components  $U_x$ ,  $U_y$  and  $U_z$  of the ground motion measured at each point of the grid defining the area containing the mountain. The input frequency  $\eta = 2$  (i.e. when  $\lambda = a$ ). The motion consists of three components along  $X$ ,  $Y$  and  $Z$ . The 3-D views of the horizontal components of motion in this section must be interpreted as follows: for  $U_x$  (top) we look at the variations of the ground motion along the  $X$ -coordinate, or  $Y$ -coordinate, of "sliced" cross-sections, or profiles, cut for a particular  $Y$ -coordinate, or  $X$ -coordinate, respectively. Accordingly, the variations of  $U_y$  with respect to either  $X$  or  $Y$  must be seen in the plot below (middle) along the  $Y$ -coordinate, or  $X$ -coordinate, of sliced cross-sections, or profiles, cut for a particular  $X$ -coordinate, or  $Y$ -coordinate, respectively. We observe that after rotation by  $90^\circ$  the horizontal components are equivalent, with nodes (zero motion) at all points along  $X$  and  $Y$  of the cross-sections cut at the center of the mountain, as expected from the symmetry of the incident wave. The square symmetry of the horizontal motions, shows cancellation towards the edges, for both components, indicating minimum leaking of seismic energy towards the half-space in the directions along the diagonals at the base of the mountain. The variations of the vertical component  $U_z$  along both  $X$  and  $Y$  are shown at the bottom of the figure. The value of 2 corresponds to the response of the half-space to the incident  $P$  wave. The maximum amplitude, of about 8.5, occurs at the top of the hill. This can be seen in Figure 27, where the top two rows correspond to the three components of ground motion at two perpendicular profiles intersecting at the top of the mountain along  $X$  and  $Y$ , respectively. The maximum amplitude for the horizontal components is about 2, occurring on the flanks of the hill. The zero responses are along the profiles corresponding to the nodes in Figure 26. An example of the ground motion computed at points away from the center is shown by the two rows of plots at the bottom of Figure 27, corresponding to two perpendicular profiles intersecting at a point  $x = 12$  km, along  $X$  and  $Y$ ,



respectively. Note that the responses in this case are totally different from those at the corresponding profiles at the center, attributed to the effect of the third dimension. The case of a vertically incident  $SV$  wave is shown in Figure 28. Nodes occur at profiles crossing the center along  $X$  and  $Y$  for  $U_y$ , and along  $Y$  for  $U_z$ . Maximum amplitude occurs for  $U_z$ , of up to 4.3, but the amplitudes for the horizontals are significant, of up to 3.8 for  $U_x$  along profile  $Y$  (Figure 29). It is interesting to note that large amplitudes for the vertical component occur towards the flanks of the mountain, decreasing abruptly to zero right on the top, in accordance with the fact that the incident wave has no vertical motion. Although no computations were made for a 2-D cosine shaped mountain of equal shape ratio (3/5) as for these profiles, the motion does not resemble any of the 2-D responses given by Bouchon (1973) for several shape ratios. For the perpendicular profiles at point  $x = 12$  km described above, no large amplitudes are observed. The  $SH$  vertical incidence is shown in Figures 30 and 31, for completeness. Except for the fact that  $U_x$  and  $U_y$  correspond to a  $90^\circ$  azimuthal rotation of the  $SV$ , as expected, the description of results is exactly the same as for the previous case.

### 3.2 Canyon

Results are presented for  $\eta = 2$  for incident  $P$  waves, in order to compare the motions with those of the hill in Figure 26, and for  $\eta = 1.5$ , i.e. the incident wavelength is  $2/3$  of the base width ( $2a$ ), for incident  $S$  waves. For the vertically incident  $P$  wave case, shown in Figure 32, the profiles along  $X$  and  $Y$  passing through the center are nodal axes for  $U_x$  and  $U_y$ , respectively, showing that both components correspond to a  $90^\circ$  azimuthal rotation of the incident wave in each case, as expected. The maximum amplitude is about 2.3 for the vertical component at the bottom of the canyon, as observed in Figure 33 (top).

The cases for vertically incident  $SV$  and  $SH$  waves are shown in Figures 34 and 35, respectively. It can be observed that the three components in each case correspond to a  $90^\circ$  rotation of the input wave around the  $Z$  axis. The 2-D profile analysis is presented only for the  $SV$  case in Figure 36, showing that the maximum amplitude, about 4, occurs for  $U_x$  along the profile  $Y$  through the center. If this were a 2-D structure,  $U_x$  would be equivalent to the  $SH$



response measured along  $Y$  (anti-plane). Taking this into account, and that the ratio of depth to half-width in our case is  $3/5 = 0.6$ , and that our input wavelength is  $\lambda = 4a/3$  (or  $1.33 a$ ), we compare these 3-D responses with those by Bouchon (1973) for a cosine-shaped canyon, in Figure 5 of Part I. Although there is no case in Bouchon (1973) that matches exactly our shape ratio and input wavelength, we can take the case of  $h/l = 0.62$  in that figure as the closest ( $h$  is depth and  $l$  is half-width, i.e. equal to  $a$  in our case). We also take into account that the input wavelength  $\lambda = 5 h$  (about  $3a$ ) is characteristic of the response between  $\lambda = a$  and  $\lambda = 20a$  (Bouchon 1973). Bearing in mind the normalisations in Figure 5 of part I, the 3-D response of  $U_x$  along  $Y$  for an  $SV$  incidence resembles roughly the 2-D response for an SH wave. As well, the motion  $U_z$  along  $X$  resembles the 2-D vertical motion to an incident  $SV$ . Similarly, the 3-D  $U_x$  response for incident  $P$  in Figure 33 resembles the 2-D horizontal motion for a  $P$  wave. Such resemblance breaks down for the profiles  $X$ - $Z$  passing through  $x = 12$  km, where neither the horizontal component  $U_y$ , nor the vertical  $U_z$  cancel out.

Next we computed the 3-D responses of the canyon for an  $SV$  wave vertically incident but with azimuthal angle  $\phi = 45^\circ$ , shown in Figures 37 and 38. That is, the incidence is upon the largest base-width of the canyon equal to  $2.83a$ . The responses are symmetric in spite of the incidence, as expected, because it is only the phase of the seismic arrivals that changes in this case. As observed in Figure 38 (top), the responses along the two profiles passing through the center are remarkably the similar to those corresponding to  $\phi = 0$ , although the amplitudes are in general smaller by a factor of about 0.75. Note that the nodal lines for the horizontal components in the previous case disappear, indicating dependency on azimuthal angle. For the profiles at  $x = 12$  km (Figure 38, bottom) the symmetry breaks down, but the maximum amplitudes do not change significantly.

For the last case in this section we consider an inclined incident  $SV$  wave with  $\theta = 30^\circ$ , but with  $\phi = 0$ , shown in Figures 39 and 40. The node for  $U_y$  along  $X$  observed in the vertical incidence is conserved, but those for  $U_y$  and  $U_z$  along  $Y$  disappear. The responses are non-symmetric with respect to  $X$  and symmetric with respect to  $Y$ , for both sets of profiles. The characters of the responses of  $U_x$  along  $X$  and  $Y$  change drastically compared with those for



vertical incidence for both sets of profiles, indicating strong dependency on the angle of incidence. Contrary to most cases of inclined  $SV$  incidence in 2-D, here the amplitudes are smaller in general than those for vertical incidence, except for the vertical component.

#### 4. CONCLUSIONS

In this Part II we have performed a parametric study of the ground motion of two and three dimensional topographical structures in terms of the type of input seismic wave, frequency, angle of incidence with respect to the vertical, azimuthal angle, elastic parameters of the media and dimensions defining the shape of the structure. This study was prompted by the outcome of Part I, indicating that large mismatches exist between observed amplification factors along mountain ranges, and those predicted by theoretical methods. Such disagreements may be attributed to complex material properties, 3-D effects, and to the use of spectral ratios to compute amplification factors. Our study focused on 2-D and 3-D models that, although generic and subjected to the impact of teleseismic (plane) waves, may occur in practice. The most important outcomes from these theoretical modellings are listed below.

##### *2-D models*

- For a cosine-shaped hill surrounded by basin-like deposits of soft sediments (Case 1), the maximum amplification occurs always in the basins, for frequencies between 1.6 and 2.3 Hz, and regardless of the type of incidence ( $P$ ,  $SV$  or  $SH$ ). The maximum amplitude is about 13 for the hill with homogeneous material properties, and about 21 for that with heterogeneous distribution of  $S$ -wave velocity in the bedrock, for horizontally incident  $SH$  waves (resembling Love waves). The time-domain responses indicate that the maximum amplitudes correspond to resonance, in the basins. On top of the hill the incident wave is strongly amplified, up to four times, but the computed seismograms are of short duration. Although the spectrum is rather flat, the time-domain pulse may yield large values of peak amplitudes of the ground acceleration.



- The motion on the hill is not strongly affected by presence of the basins. That is, its responses in the frequency and time domains are similar to those of an isolated ridge in a half-space, yielding moderate amplification and mainly flat spectra along its range. The maximum amplitudes are around 3 (units of displacement of the incident wave), which is about the same for the isolated hill (Part I). The coupling between basins and hill is determined by a wave generated on the hill and propagating horizontally through the basins.
- In terms of amplitudes and variability, the coupled responses of basins and hill are sensitive to the angle of incidence.
- The inhomogeneity of the *S*-wave velocity distribution in the bedrock (Case 2) significantly affects the responses of the basins and the hill, in terms of variability and amplitudes. This applies to both the frequency and time domains.
- For the ridge formed by dipping gravel layers within a sedimentary basin (Case 3) the maximum amplitudes, up to 20, occur on the deposits of sediments, close to the foot of the ridge, for all types of incident wave considered. The amplitudes on the ridge are much smaller in comparison, but reach a maximum value of 5 for horizontally incident *SH* waves. The variability of the response along the ridge is small, compared with that on the basins, yielding mostly flat spectra.
- The time-domain responses show that most of the wave propagation processes occur within the sediments after the arrival of the incident wave. Except for the strong amplification of the primary pulse, only small phases appear to arrive at stations on the hill scattered from the basins.
- Amplifications at the base of the ridge in the case considered increase with frequency up to 1.42 Hz, then decrease abruptly.



### 3-D models

- The maximum amplitude of the response of a cosine-shaped hill, or mountain, with square base and homogeneous material properties occurs for the vertical component, of up to 8.5 (units of displacement of the incident wave) upon the incidence of a  $P$  plane wave. The effect of the third dimension at the top of the hill is to strongly alter the horizontal components. For the case of the canyon, the maximum amplification values do not exceed 4 for all the input waves considered.
- In general the character of the responses for both canyon and hill, or their spatial variation, depends weakly on the azimuthal angle of incidence  $\phi$ . However, the nodal profiles for a particular azimuth, i.e. the profiles along which one or more components of motion cancels out, disappear at different azimuths.
- The responses of both hill and canyon depend strongly on the incident angle.
- The motions at 2-D cross-section profiles away from the center of the hill do not resemble at all those corresponding to profiles passing right through the center. This can be attributed mainly to 3-D effects because, first, the relation of input wavelength to size of hill at the base of these profiles is the same as for the center and, second, the effect of the change of shape ratio due to smaller height only does not strongly affect the character of the overall response.
- The 3-D models of canyons reveal that when the response of one of the horizontal components is nodal along profiles passing through the center, the response of the other components with respect to either  $X$  or  $Y$  roughly resemble those for an equivalent 2-D model (see Figures 33 and 34, compared with Figure 5 of Part I). This resemblance breaks down when none of the horizontal components is nodal. Resemblance to 2-D responses does not appear to occur for the case of the hill, although more numerical experiments are required to study the extent to which the response computed with 2-D models are representative of the response in 3-D.



In general the models proposed here do not yield amplification factors as large as those reported for observations (up to 30). The largest amplification factor from the 2-D complex models can be estimated at about 20 from spectral ratios, taking as reference site stations away from the hill. The factors computed using reference stations close to the hill can be quite variable. On the other hand, the amplification factors on the basins, or other sites away from the hill, can be accurately computed from spectral ratios taking as reference a site on the hill (outcrop), because in all instances studied here and in Part I, the character of the response of the hill does not appear to be strongly affected by the surrounding geology.



TABLE I  
Homogeneous

Type	Angle	Component	Frequency (Hz)	Amax	Position (km)
SH	0	V	1.71	8.64	3.5
P	0	Ux	2.25	4.64	3.5
P	0	Uz	1.77	10.78	3.0
SV	0	Ux	1.59	8.66	8.0
SV	0	Uz	2.01	4.90	3.0
SV	75	Ux	2.37	11.76	8.5
SV	75	Uz	2.04	12.00	3.0
R	90	Ux	1.74	7.34	3.0
R	90	Uz	1.83	7.26	3.0

Inhomogeneous

SH	0	V	1.80	13.60	3.5
SH	90	V	1.77	20.62	3.5

Table I: The values of maximum amplitude  $A_{max}$  computed for the models of hill and basins in Case 1 (homogeneous) and Case 2 (inhomogeneous); given for the type of incident wave, the angle of incidence with respect to the vertical, the component of motion, the frequency of occurrence and position. Note the differences in amplitude of the  $SH$  response for both cases, which can be attributed only to the effect of heterogeneity of the  $S$ -wave velocity. In general, the maximum values occur in either of the basins and not always at positions corresponding to their maximum depth. Note also that no maximum amplitude occurs on the hill.

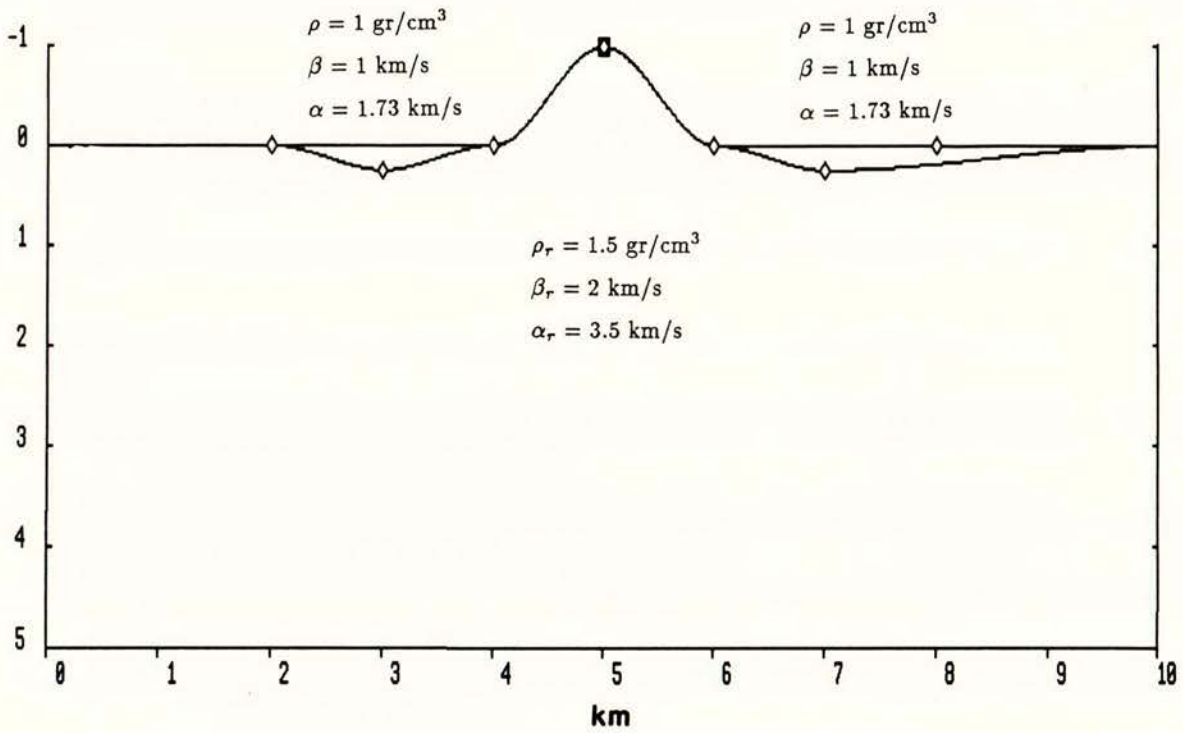


Figure 1. The model of a hill flanked by two irregular basins extending over 10 kilometres (Case 1). The shapes of the hill and basins are determined by cubic-splines fitted at the points marked with blank diamonds, and at the end points of the geometry. The hill is 2 km wide at its base, and 1 km high, i.e. its shape ratio is 1/2. The maximum depth of the basins is 250 metres, and both have the same elastic properties.

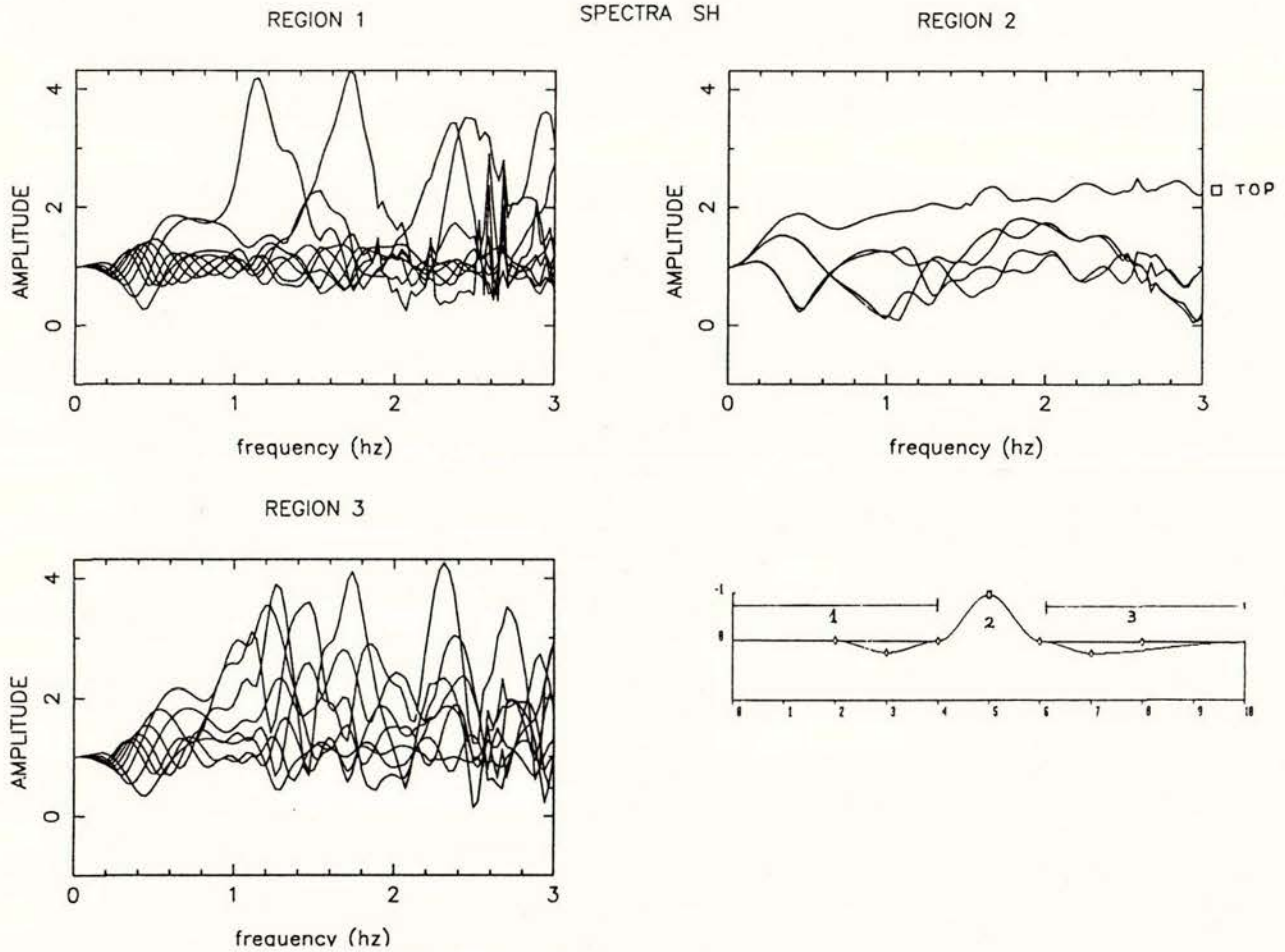


Figure 2. Frequency response of the stratigraphy depicted in Figure 1, to a vertically incident SH wave. Values are divided by a factor of 2, i.e. normalised with respect to the response of the half-space without the stratigraphy. Each trace corresponds to the spectrum computed at a point on the surface, or station, for 100 frequencies sampled between 0 and 3 Hz. The whole geometry is divided into region 1, between 0 and 4 km; region 2, between 4 km and 6 km, and region 3, between 6 km and 10 km. The responses are given for 9 stations regularly distributed along the free-surface of region 1, 5 stations in region 2 and 8 stations in region 3. Only the trace at the top of the hill is identified, with a blank square symbol.

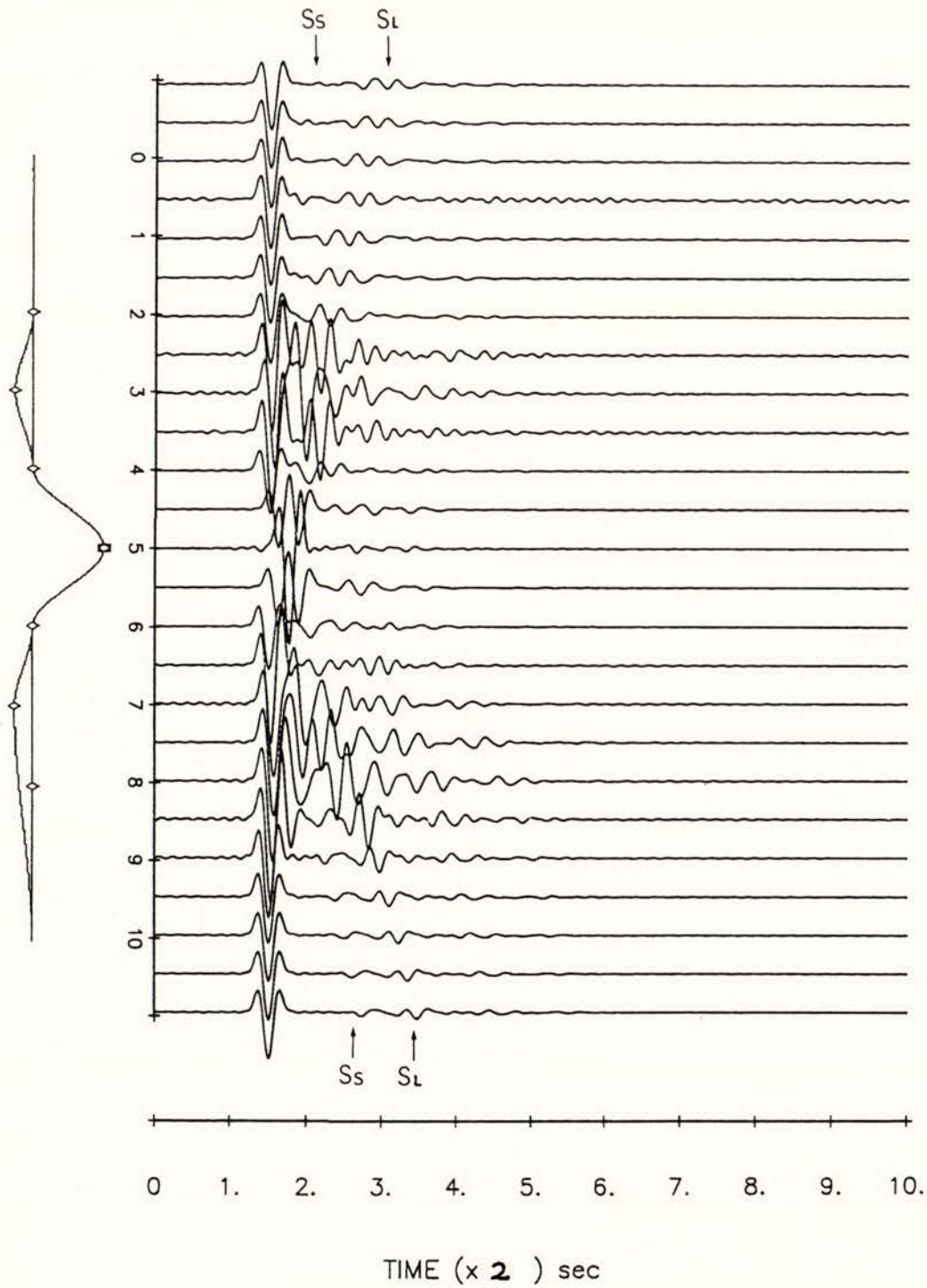


Figure 3. Time-domain response (or synthetic seismograms) to a vertically incident  $SH$  wave at 21 surface points along the geometry depicted in Figure 1 between 0 and 10 km. Two additional stations outside the geometry on each side are included in order to account for the wavefield propagating away from the model. The seismograms correspond to a Ricker wavelet input source-time function, of 1.5 Hz peak frequency. The arrows mark the reflections from the basin-bedrock interfaces ( $S_s$ ), and the arrivals at both ends of a phase caused by scattering at the hill ( $S_L$ ), propagating horizontally throughout the basins.

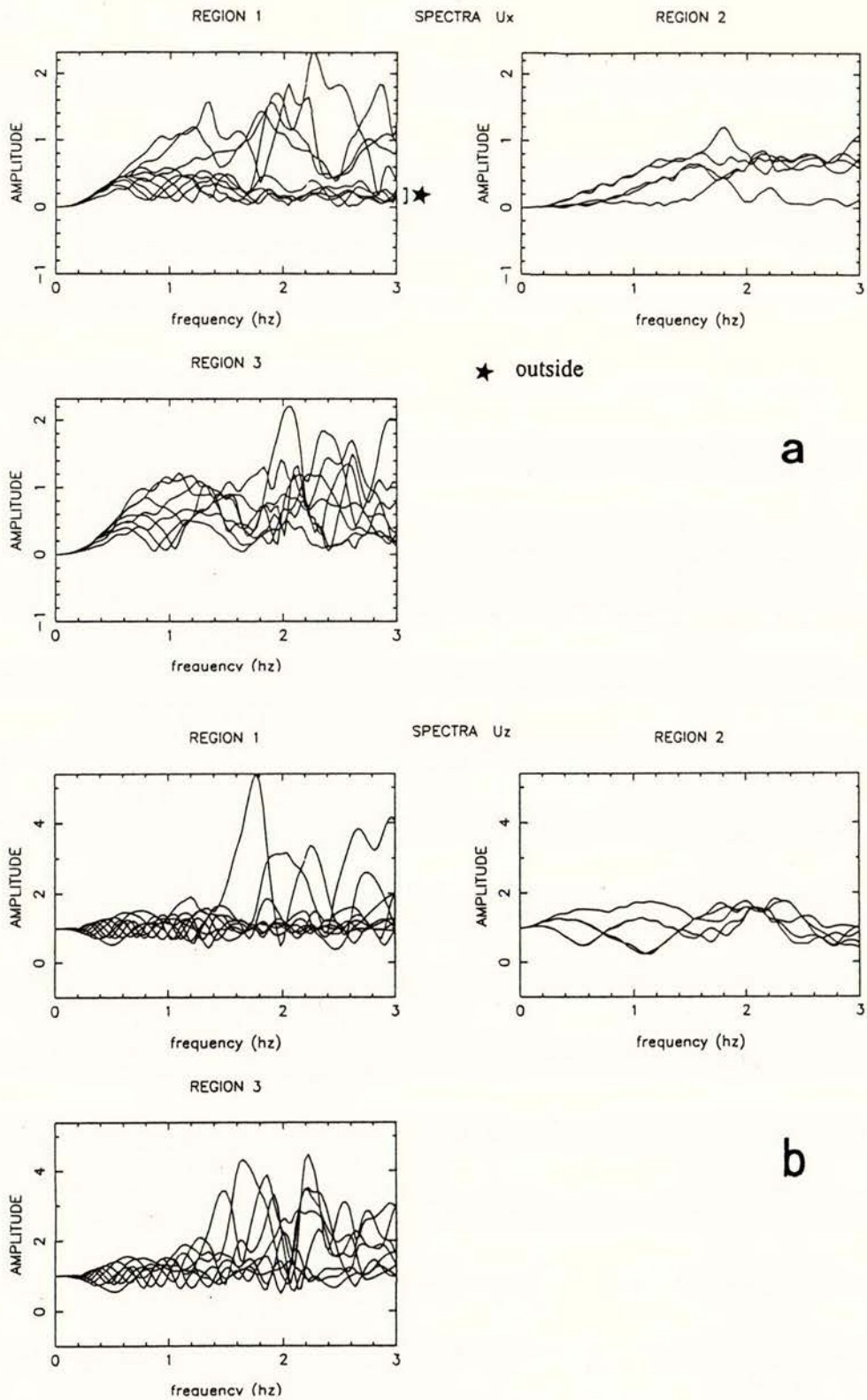


Figure 4. Frequency response of the stratigraphy depicted in Figure 1 to a vertically incident  $P$  wave; (a) corresponds to the horizontal component of motion  $U_x$ , and (b) to the vertical  $U_z$ . The set of traces outside the basin in region 1 is identified.

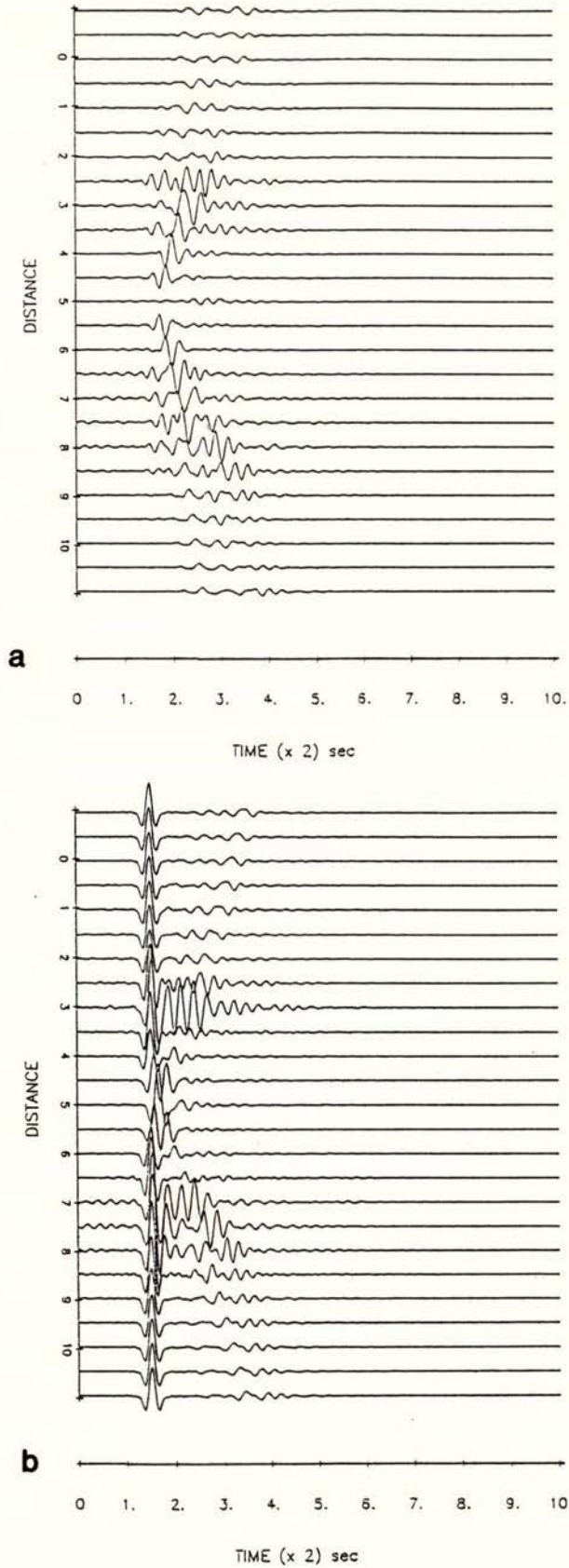


Figure 5. Time-domain response to a vertically incident  $P$  wave, for  $U_x$  (a) and  $U_y$  (b). The description follows that of Figure 3. The apparent non-causal arrivals at points around  $x = 3$  km and  $x = 7$  km are an artifact due to wrap-around effect related to the periodicity of FFT (Fast Fourier Transform) to synthesise the strong resonances that occur at those points.

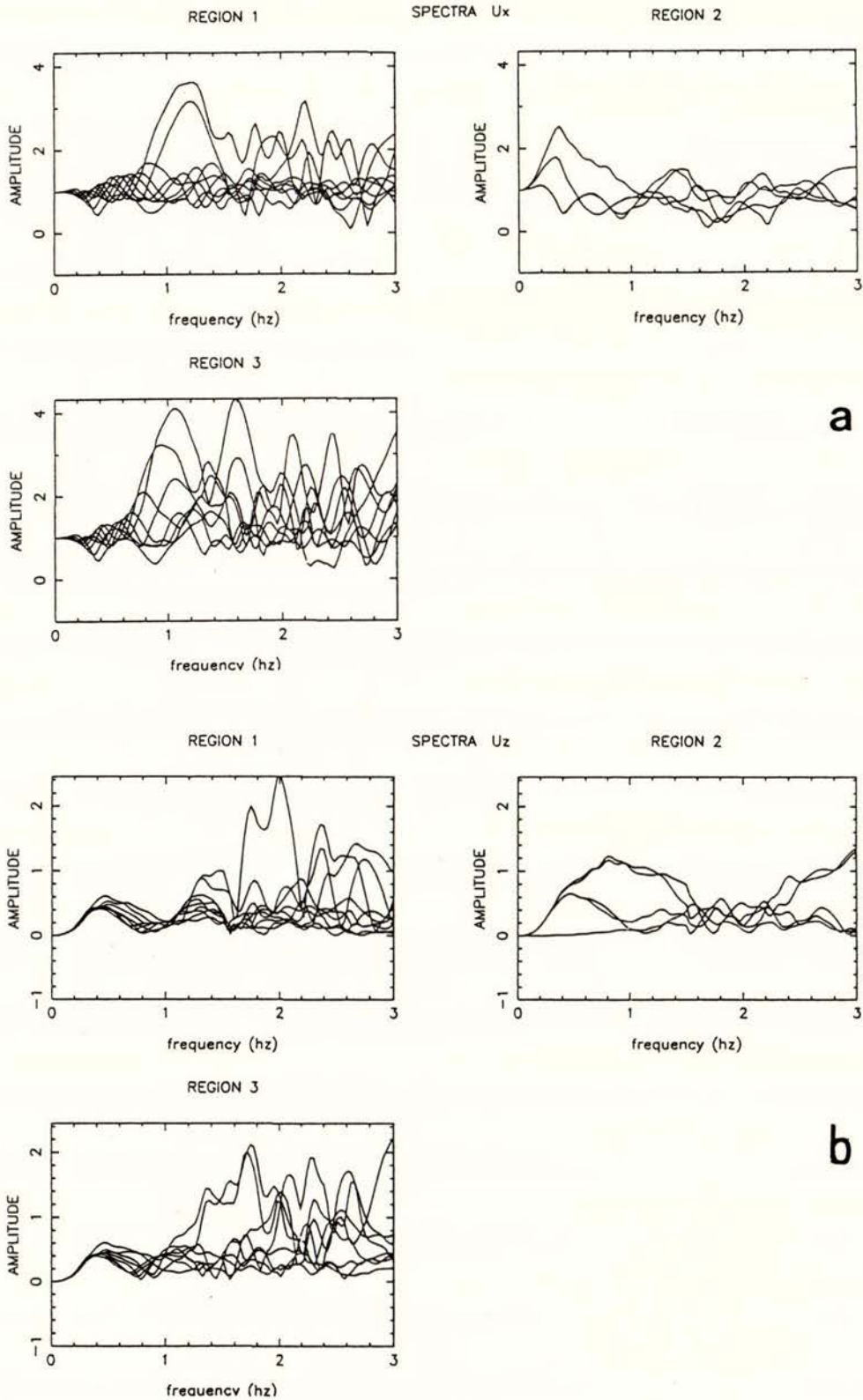


Figure 6. Frequency response to a vertically incident  $SV$  wave, for regions 1, 2 and 3, as in Figure 5. (a) corresponds to  $U_x$  and (b) to  $U_z$  components.

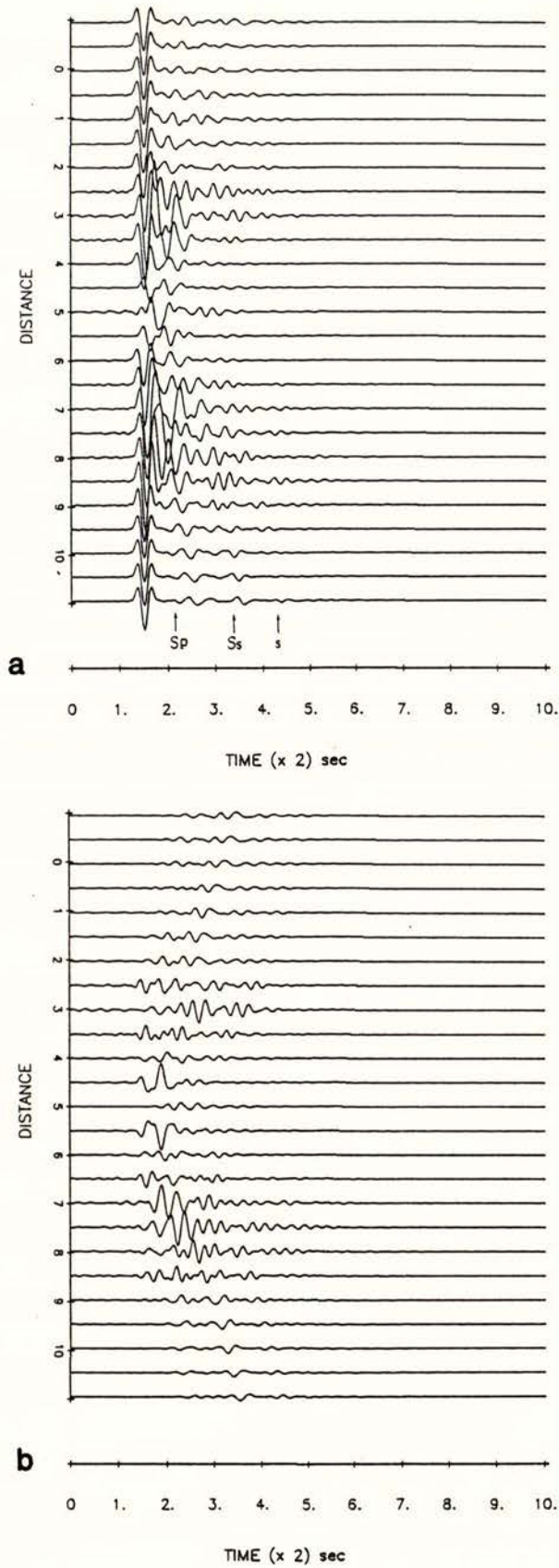


Figure 7. Time-domain response to a vertically incident SV wave, for  $U_x$  (a) and  $U_y$  (b). The peak frequency of the Ricker wavelet is 1.04 Hz. First reflected/converted phase is pointed at by an arrow, as well as distinctive S phases resulting from multiple bouncing within the basins.

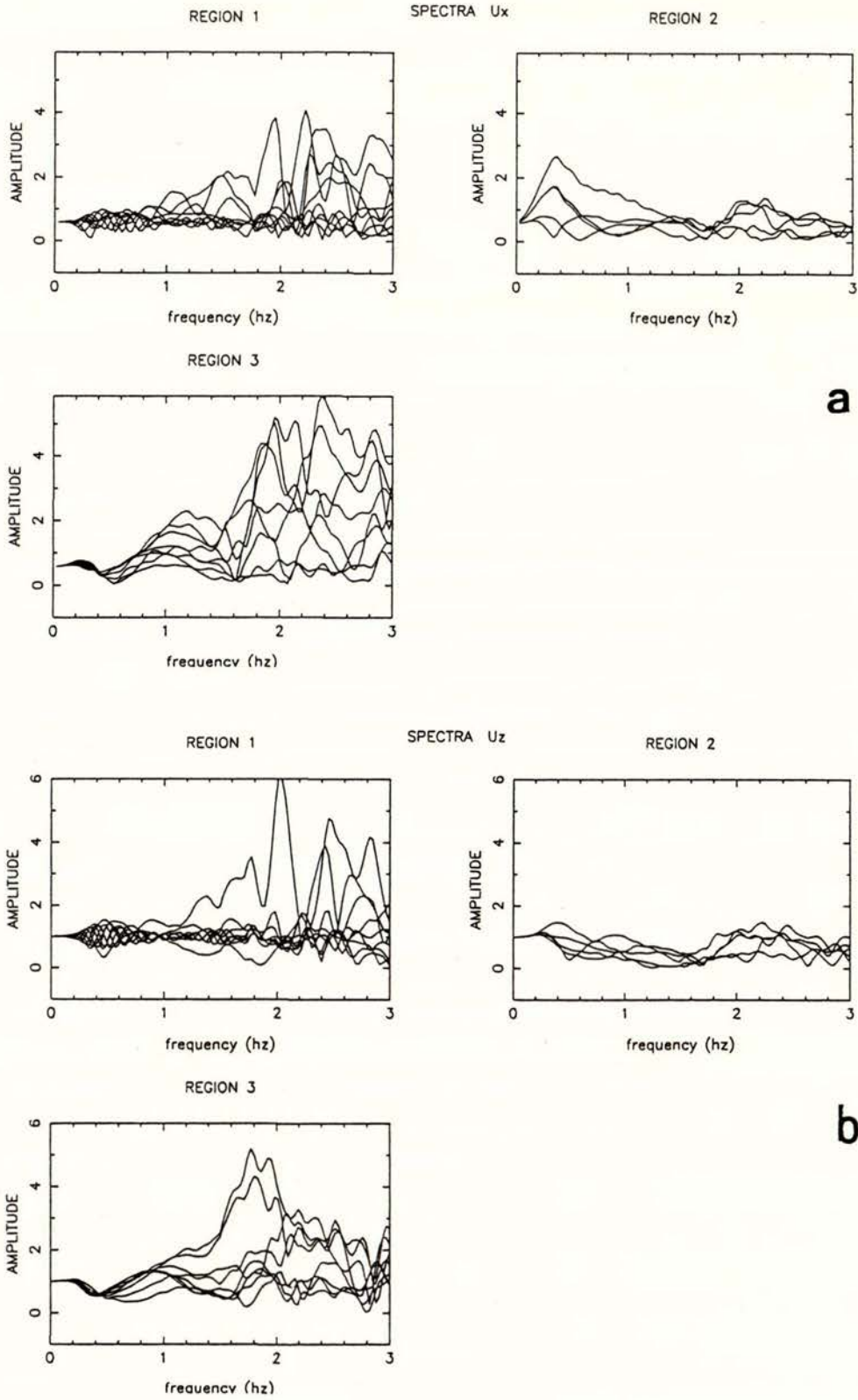


Figure 8. Frequency response to an *SV* wave incident at  $75^\circ$ , (a) for  $U_x$ , (b) for  $U_z$ .

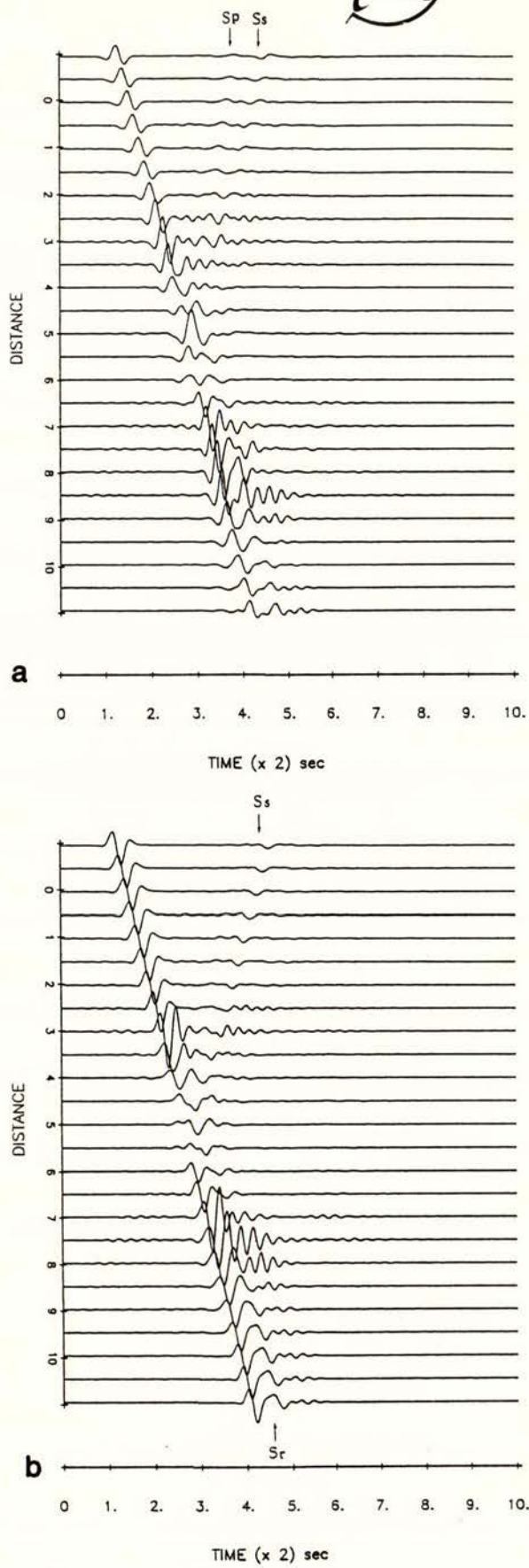


Figure 9. Time-domain response to an  $SV$  wave at  $75^\circ$ , for  $U_x$  (a) and  $U_y$  (b). First reflected/converted phases at the bedrock-sediment interface are well identified for region 1. In (a) arrivals prior to the incident wave in region 3 correspond to  $S$  to  $P$  conversions.

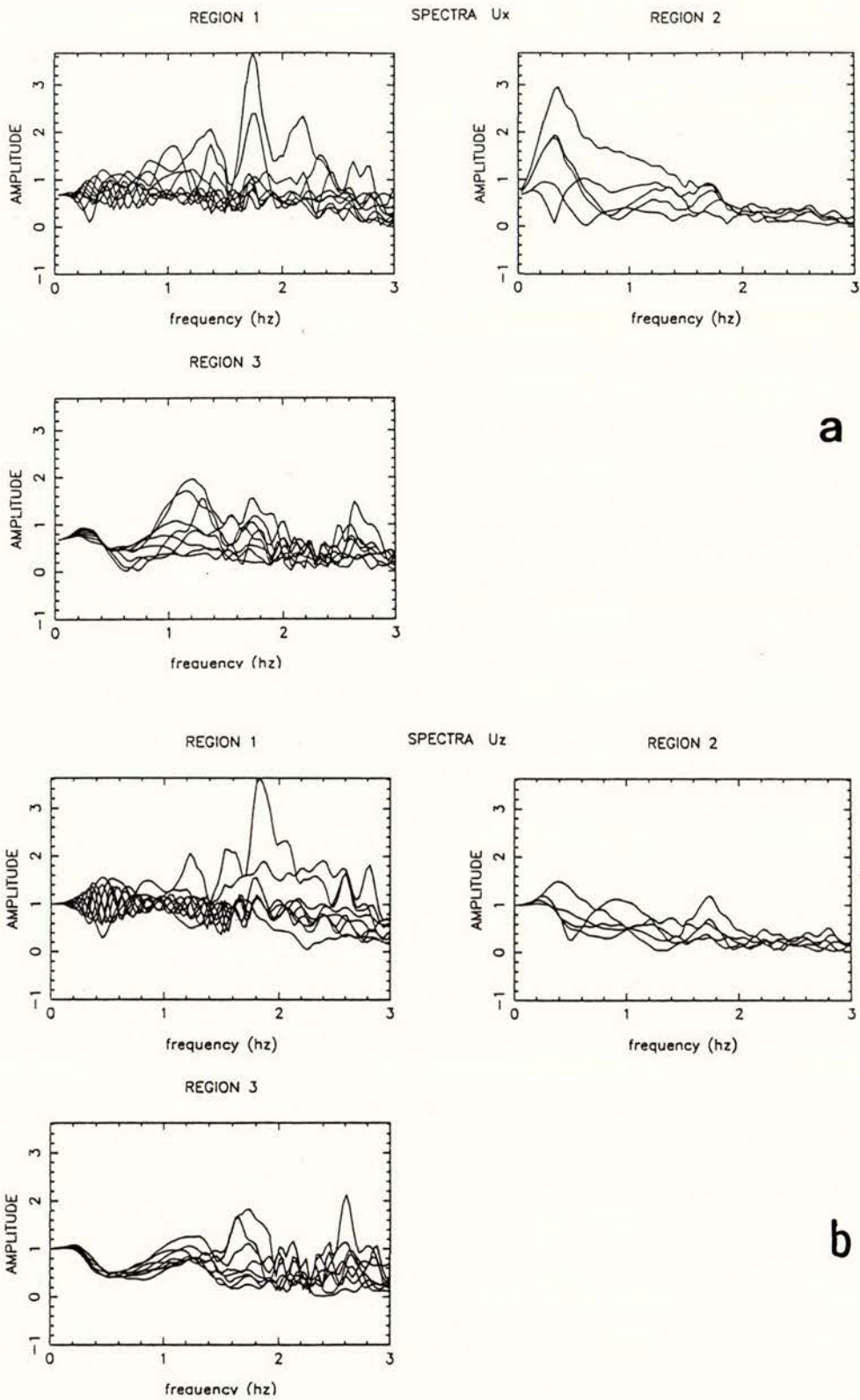


Figure 10. Frequency response to a Rayleigh wave incident from the left side ( $90^\circ$ ) of the stratigraphy depicted in Figure 1, (a) for  $U_x$ , (b) for  $U_z$ .

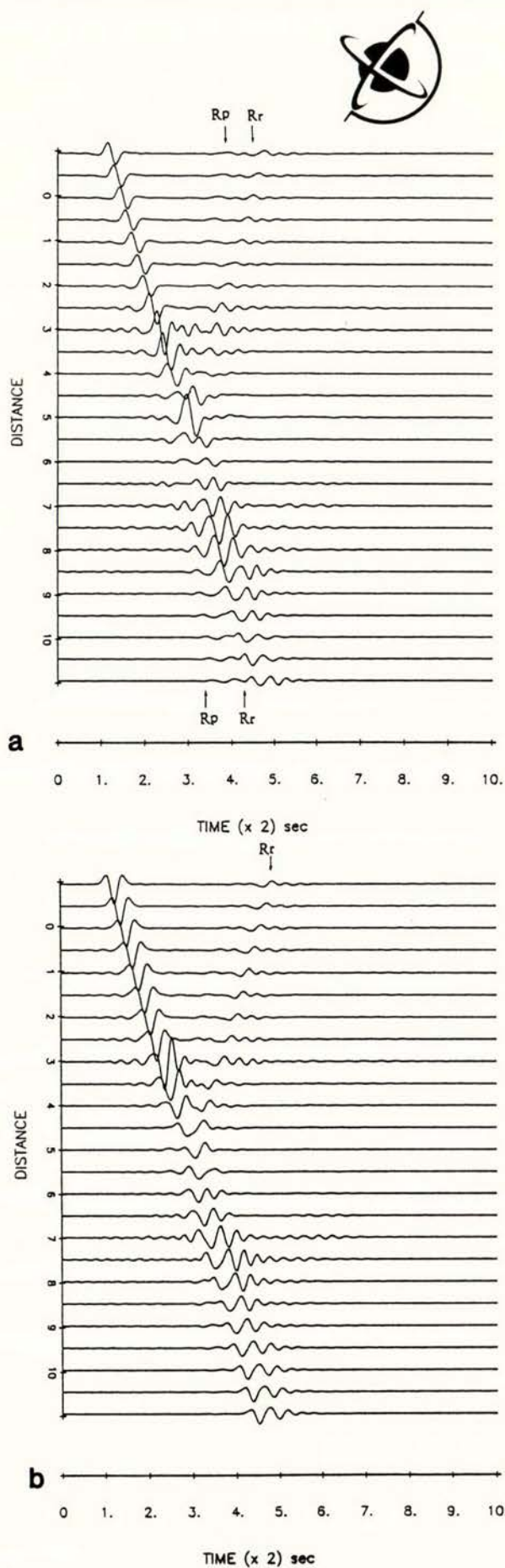


Figure 11. Time-domain response for the Rayleigh wave described in Figure 10, (a) for  $U_x$ , and (b) for  $U_z$ . The Rayleigh wave appears to be strongly attenuated from  $x = 4.5$  km towards the end of the geometry in region 3 ( $R_r$ ). The large amplitude at the top of the hill and at the basins must be due to constructive interference with scattered body  $P$  waves ( $R_p$ ).

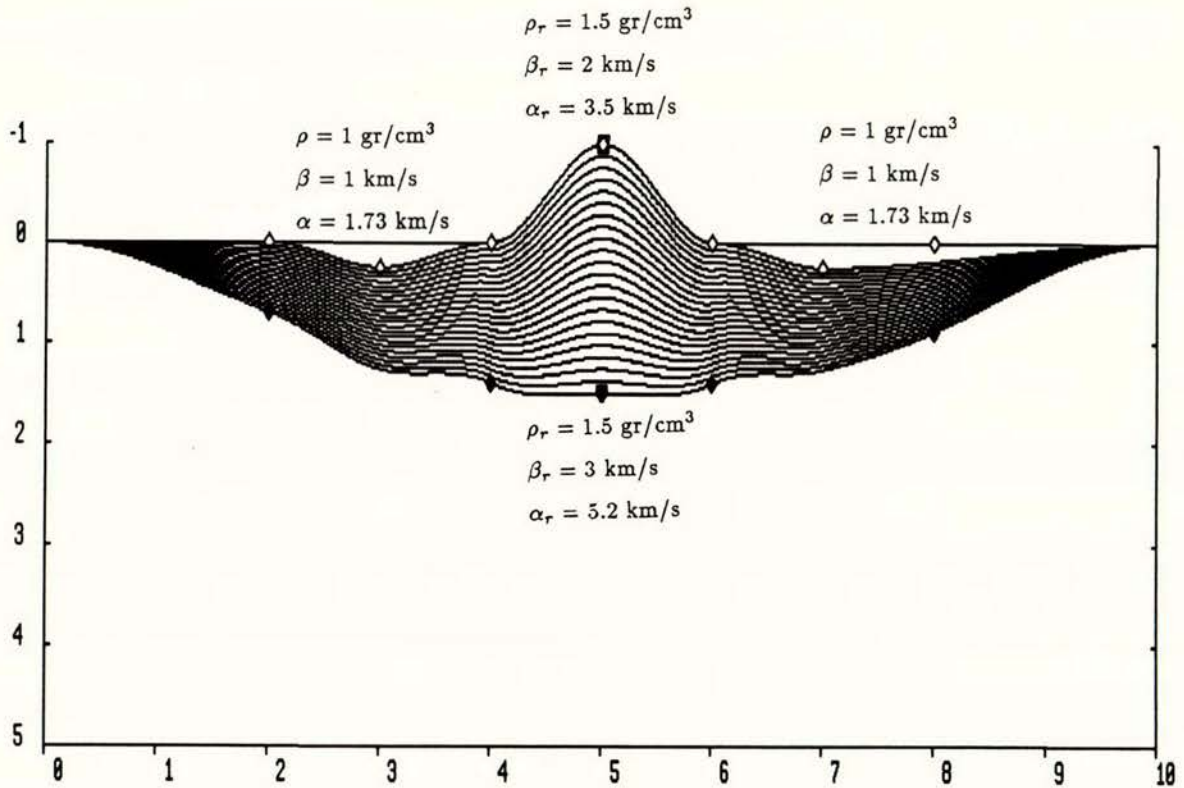


Figure 12. The model of a hill flanked by two irregular basins of Case 2. The geometry is identical to that of Case 1 (Figure 1), but here the velocity of  $S$  waves in the bedrock  $\beta_r$  varies in such a way that at  $x = 5$  km  $\beta_r$  is 2 km/s at the top of the hill ( $z = -1$  km) and 3 km/s at a depth  $z = 2.5$  km. The curve that passes through  $x = 5$  km and  $z = 2.5$  km marked with dark diamonds defines an artificial, arbitrary boundary separating the region where  $\beta_r$  varies, from the region (half-space) where  $\beta_r$  is constant with value 3 km/s. There is no impedance contrast along this boundary. At the free-surface and along the interfaces of the bedrock with the two basins  $\beta_r$  has the same value as that on the top of the hill. The  $S$  wave velocity of the medium between the free-surface outside of the basins and the artificial boundary with the half-space is sampled by cubic-splines. The 22 lines plotted illustrate the overall variation, where each line represents the points of the medium where  $\beta_r$  is constant.

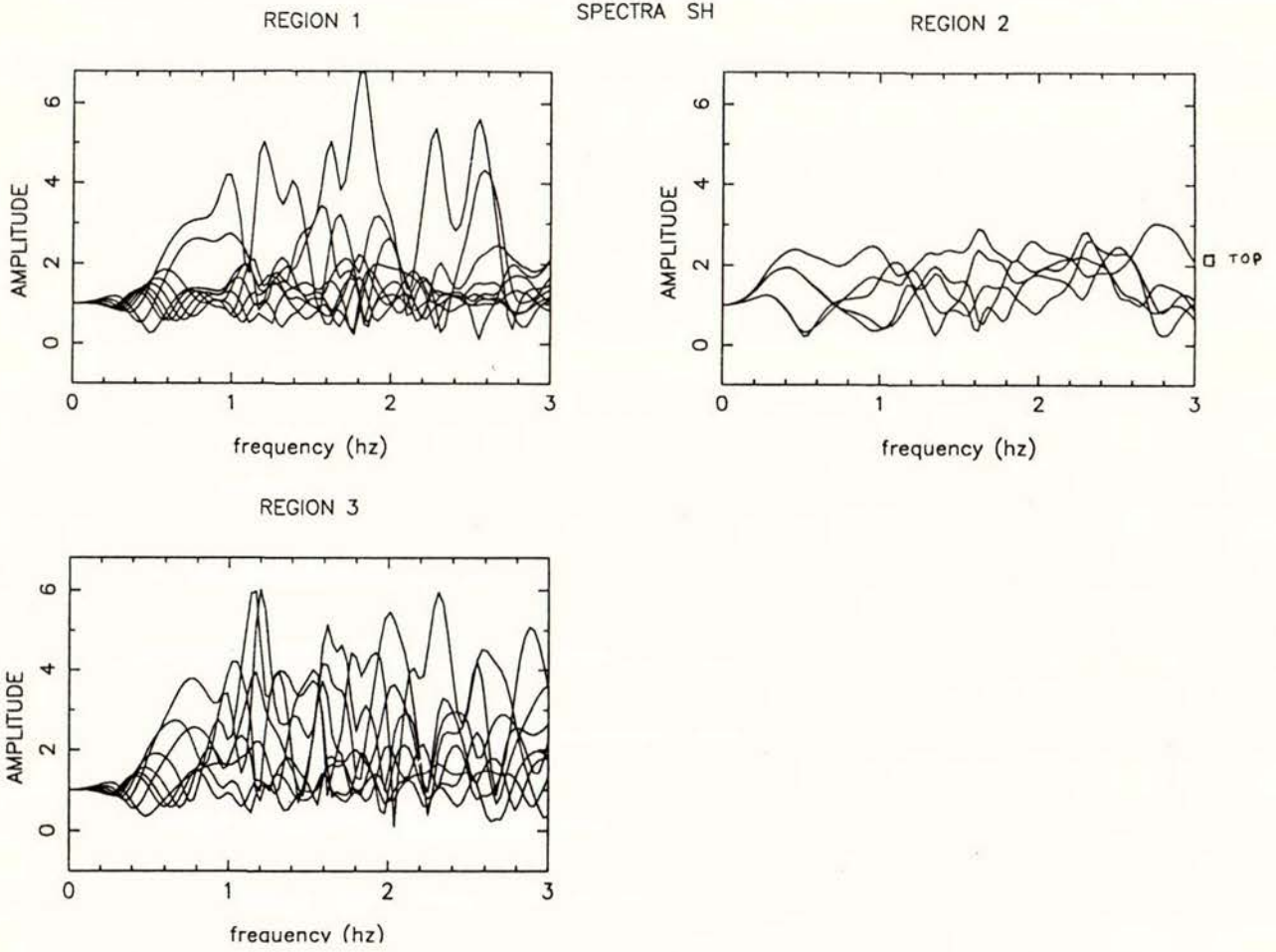


Figure 13. Frequency response of the stratigraphy depicted in Figure 12 to a vertically incident *SH* wave. The regions 1, 2 and 3 are defined in Figure 2, and the values are divided by 2, i.e. normalised with respect to the response of the half-space without the stratigraphy.

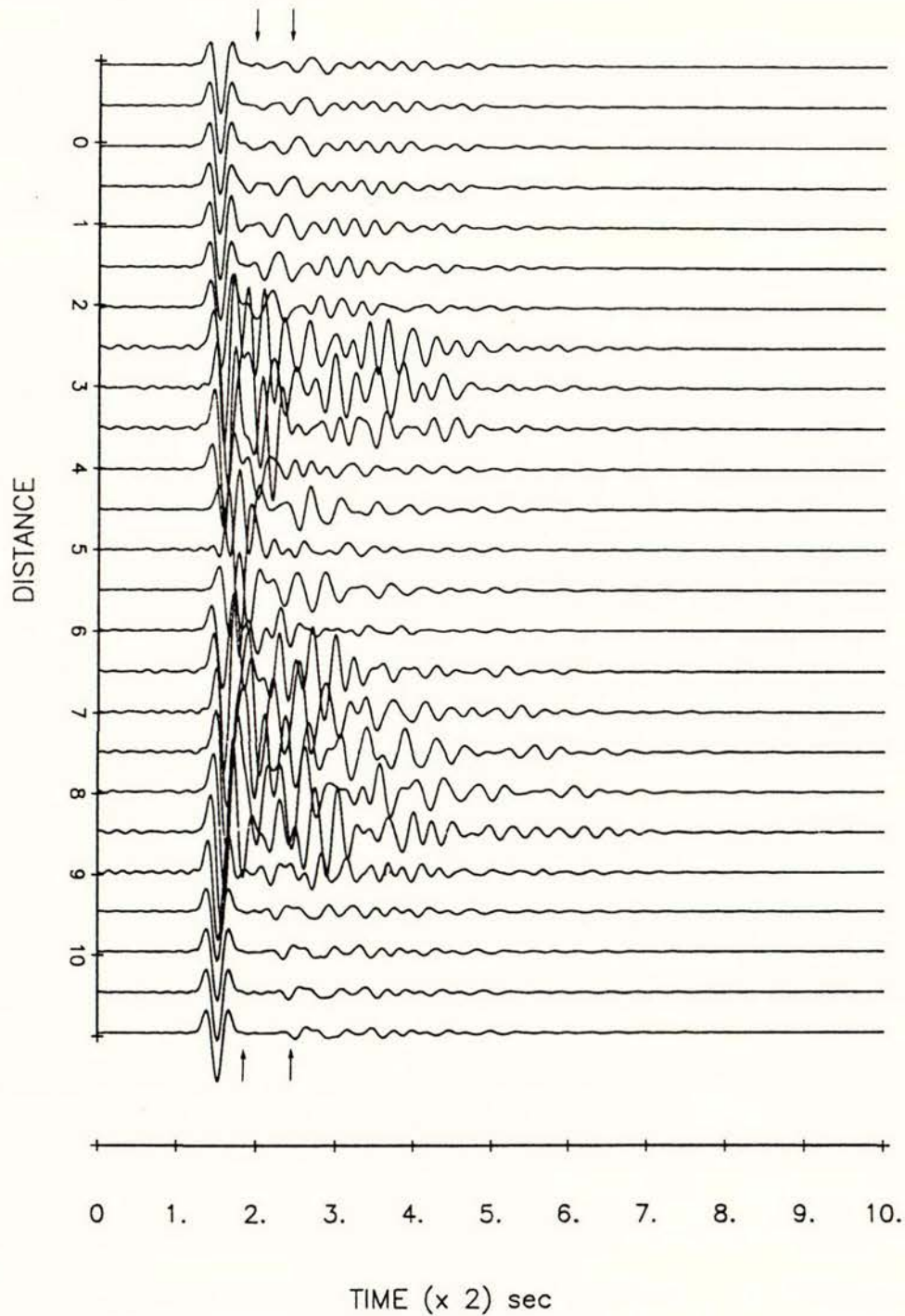


Figure 14. Time-domain response of the stratigraphy depicted in Figure 12 to a vertically incident *SH* wave. The traces' distribution is identical to that of Figure 3, and the peak frequency of the Ricker wavelet is 1.5 Hz. Arrows point at first reflected phases, which appear to arrive at shorter times than those of the homogeneous case (Figure 3).

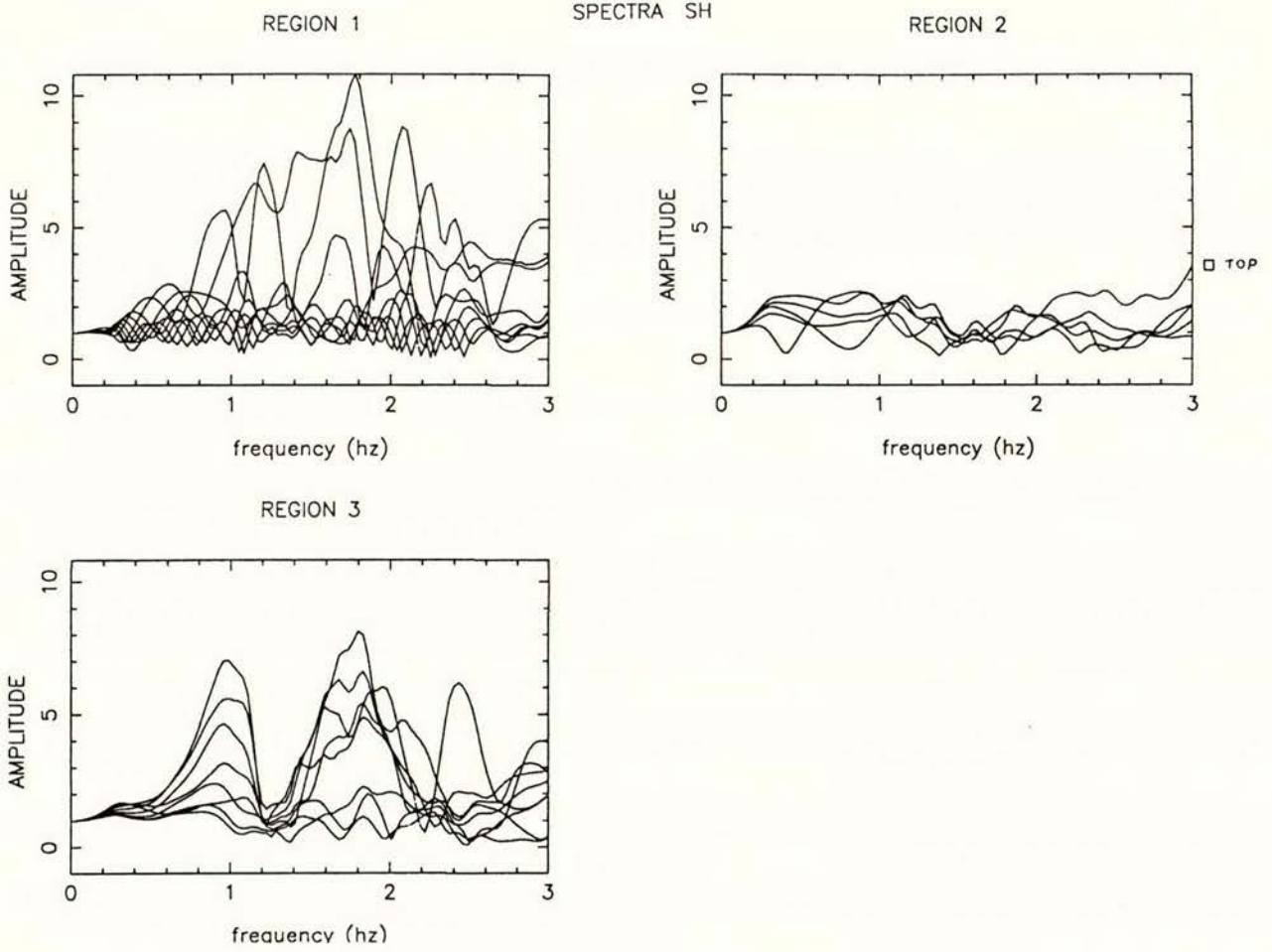


Figure 15. Frequency response of the stratigraphy depicted in Figure 12 to a horizontally incident *SH* wave (at  $90^\circ$ ).

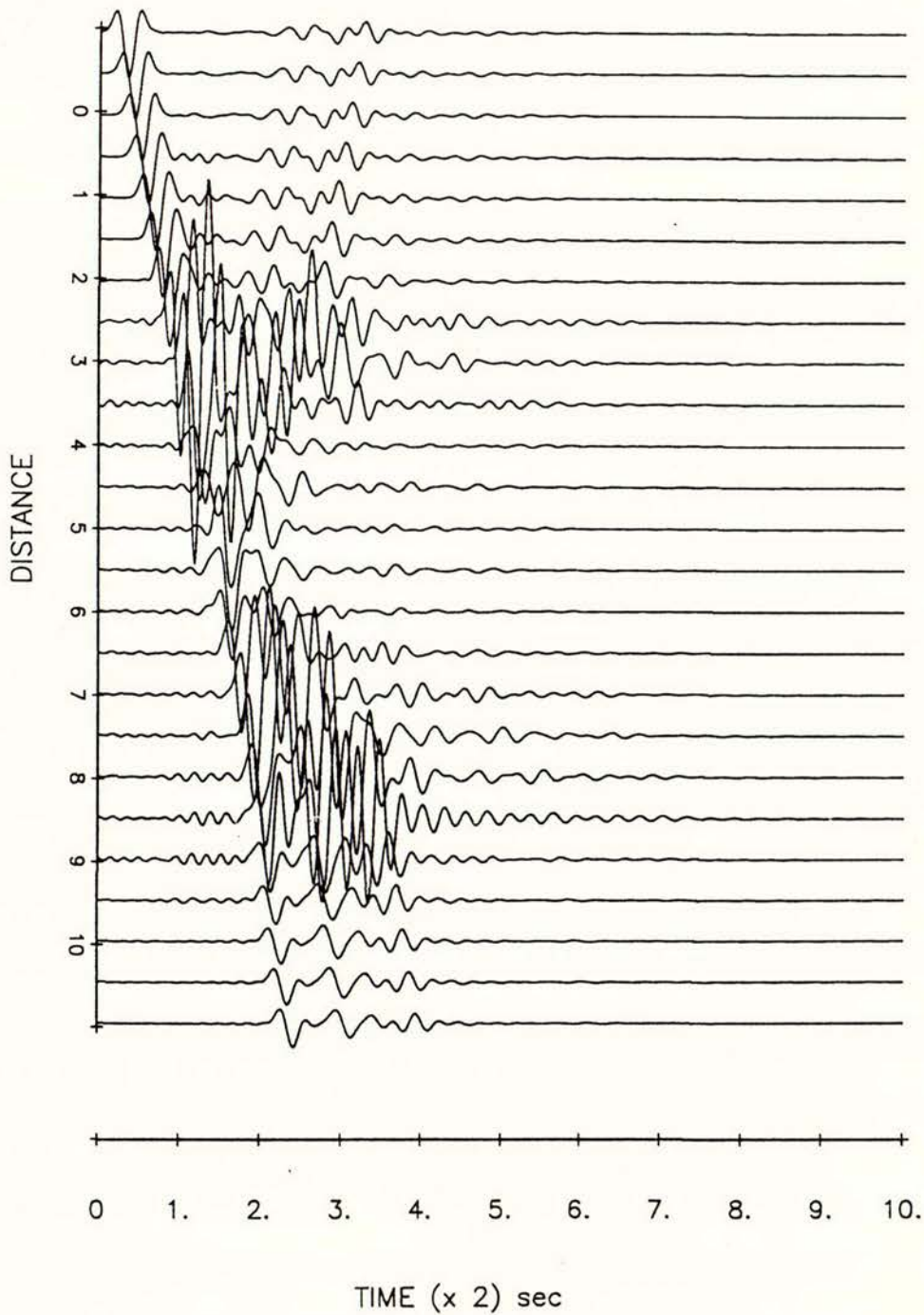
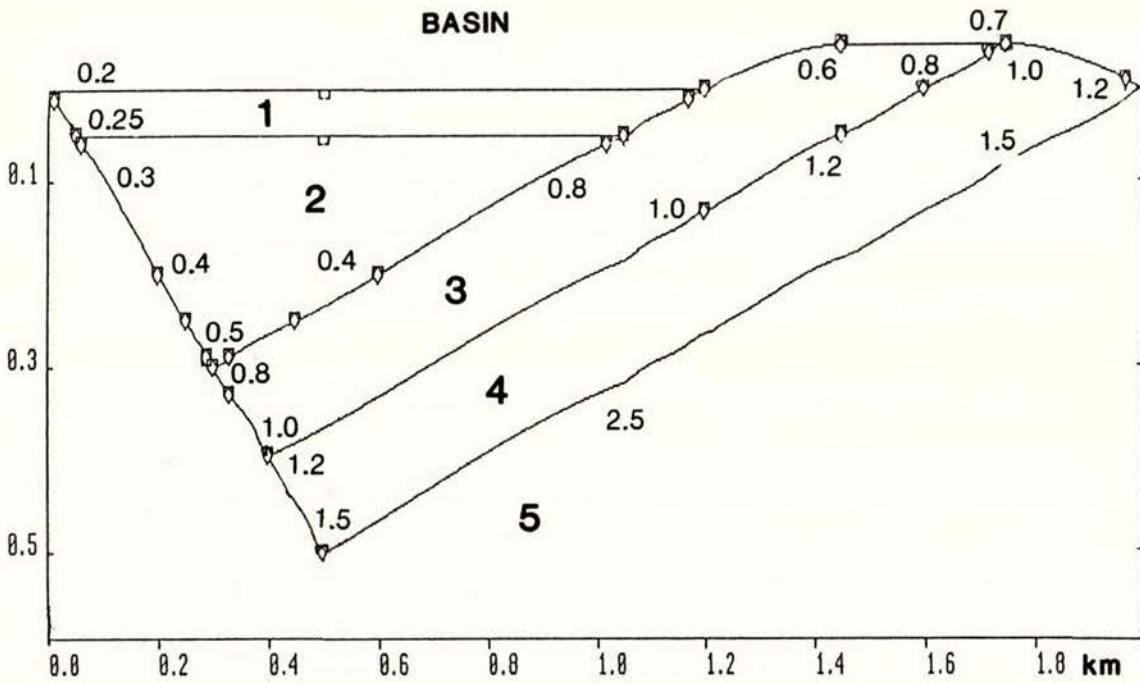
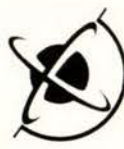


Figure 16. Time-domain response to the horizontally incident *SH* wave described in Figure 15. Apparent non-causal arrivals are caused by an artifact "wrap-around" periodicity effect of FFT, due to poor frequency sampling to account for the observed large amplitudes in the basins.



	$\beta$	$\alpha$	$\rho$	$Q$
<b>1</b>	0.2	1.0	1.5	5
	0.23	1.25	1.75	6.67
<b>2</b>	0.25	1.5	2.0	10
	0.3	1.6	2.05	11.11
	0.4	1.8	2.15	14.28
	0.5	2.0	2.25	20
<b>3</b>	0.6	2.1	2.3	22.22
	0.7	2.2	2.35	25
	0.8	2.3	2.4	28.57
	1.0	2.5	2.5	40
<b>4</b>	1.0	2.5	2.5	40
	1.2	2.7	2.55	50
	1.5	3	2.62	80
<b>5</b>	2.5	4.5	2.75	$\infty$

Figure 17. Stratigraphy for the basin and ridge of Case 3. The model extends from 0 to 2 km. The four layers, numbered from 1 to 4, are embedded into a half-space, numbered 5. Layers of gravels 3 and 4 are tilted, forming a ridge that rises 100 metres above the free-surface level ( $z = 0$  m). Layers 1 and 2 are horizontal deposits of sediments. The interface between the bedrock and both the gravels and sediments are roughly of triangular shape. All four layers are of inhomogeneous material properties. The values of density  $\rho$ ,  $S$  and  $P$  wave velocities  $\beta$ ,  $\alpha$ , respectively, and attenuation factor  $Q$  (equal for  $P$  and  $S$  waves) are listed on the sides of the model. The values of the elastic parameters for each layer are specified at points marked with blank diamonds inscribed into half-squares. For example, in this figure the values of  $S$  wave at those points are indicated explicitly. The values at intermediate points are sampled by cubic-splines. The values of the elastic parameters for the half-space are constant, as listed, with no attenuation for either  $P$  or  $S$  waves ( $Q = \infty$ ).

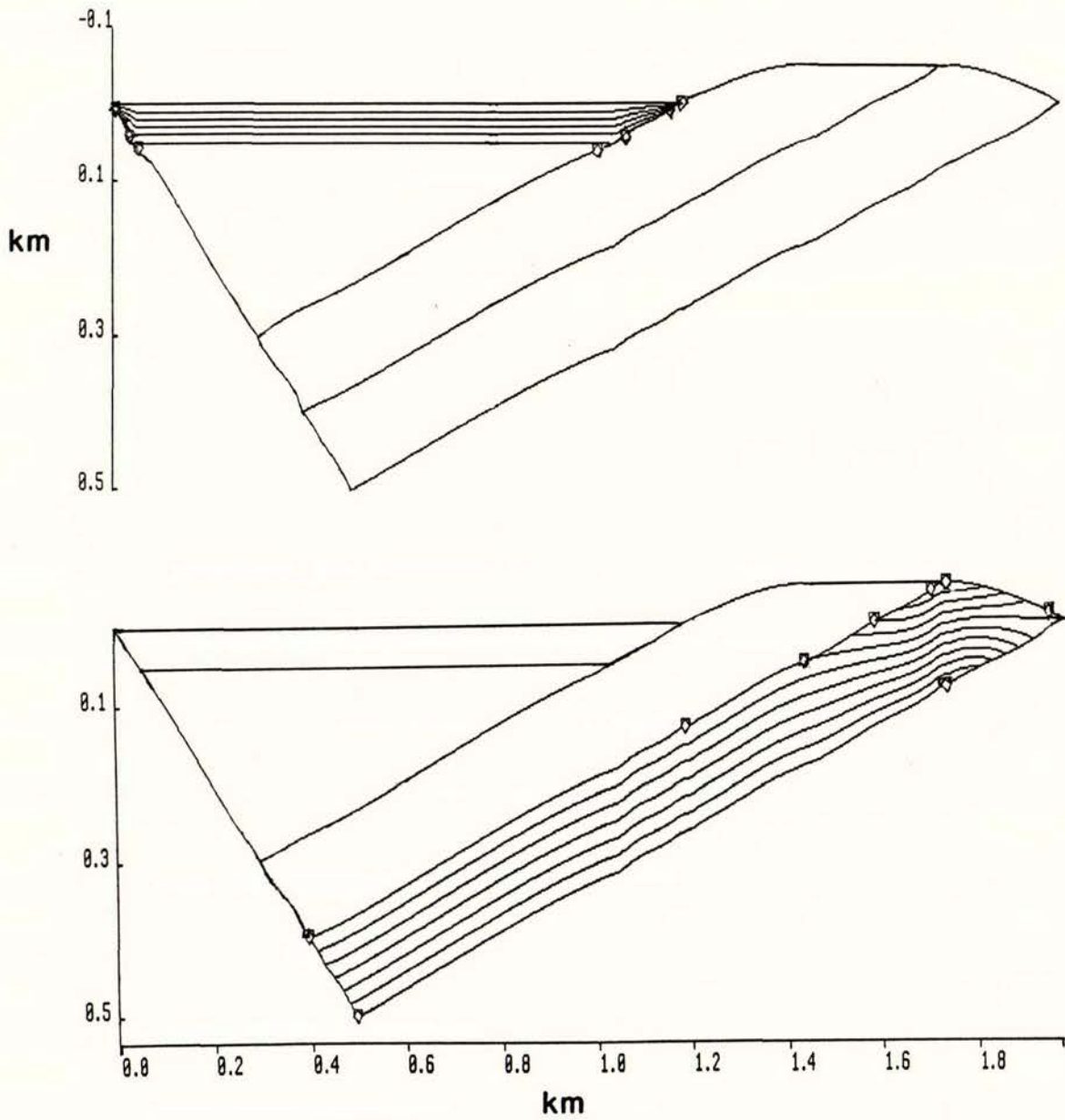


Figure 18. Lines of constant  $S$  wave velocity in layer 1 (top) and layer 4 (bottom) determined by cubic-splines, of the stratigraphy depicted in Figure 17. As example, 5 traces in layer 1 and 9 traces in layer 4 are plotted.

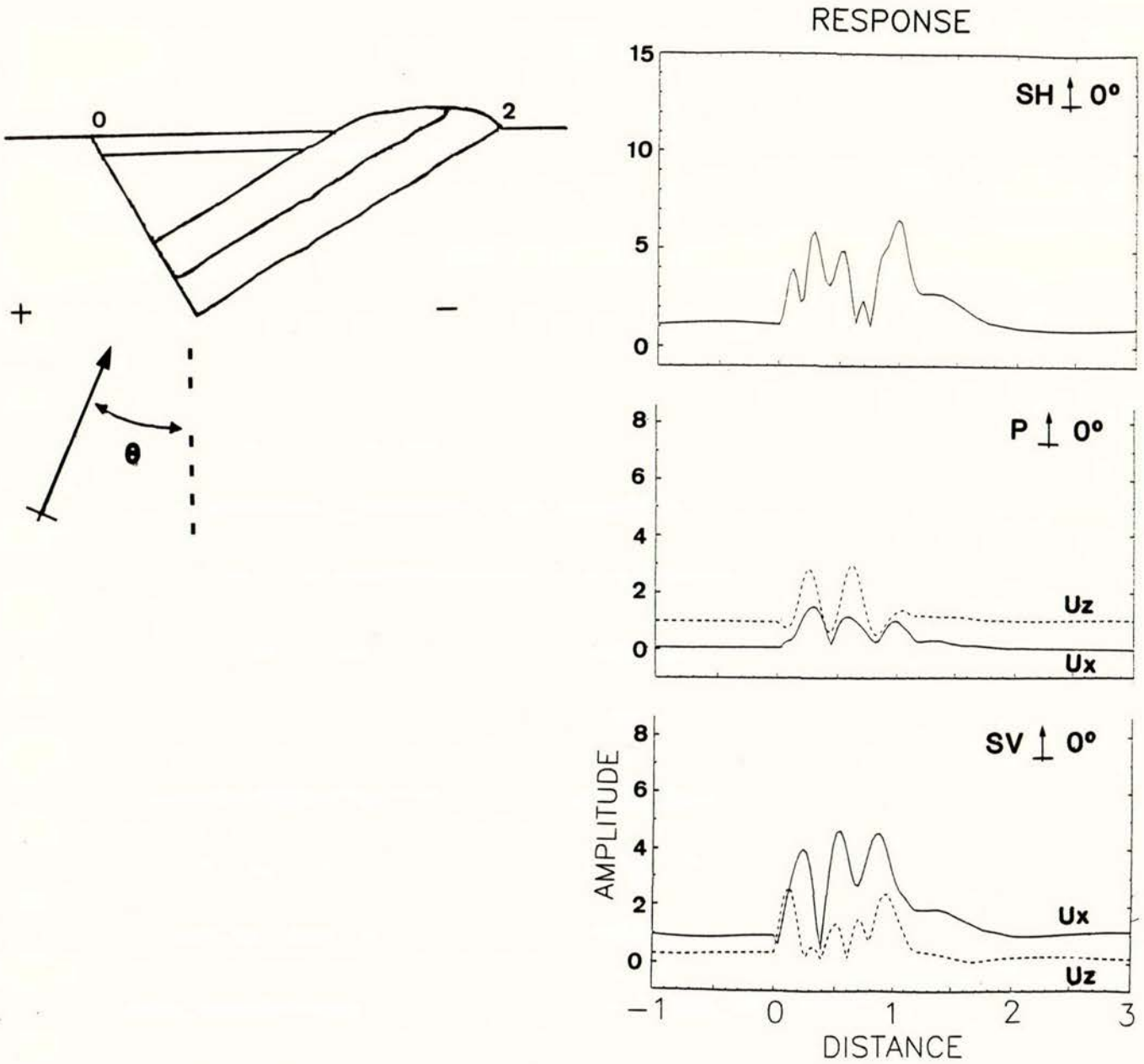


Figure 19. Amplitude distribution of the ground response of the stratigraphy depicted in Figure 17 to vertically incident  $SH$ ,  $P$  and  $SV$  waves. In all cases the input frequency is 2.5 Hz. In general, the angle of incidence  $\theta$  is measured clockwise with respect to the vertical (top left). Amplitudes are normalised with respect to the response of the half-space without the stratigraphy (factor of 2).  $U_x$  (full line) and  $U_z$  (dotted line) correspond to the horizontal and vertical components of motion, respectively.

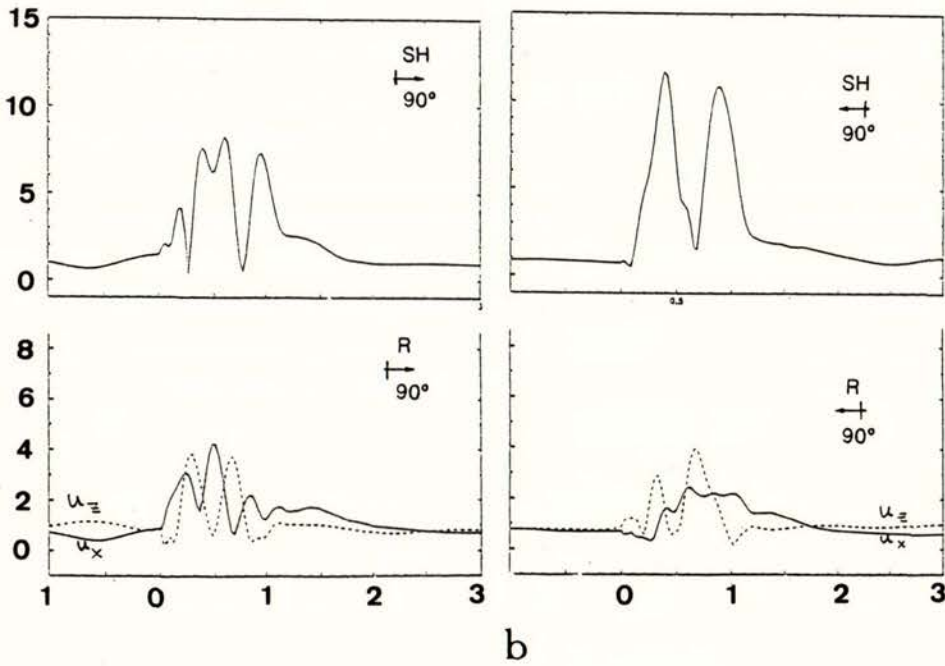
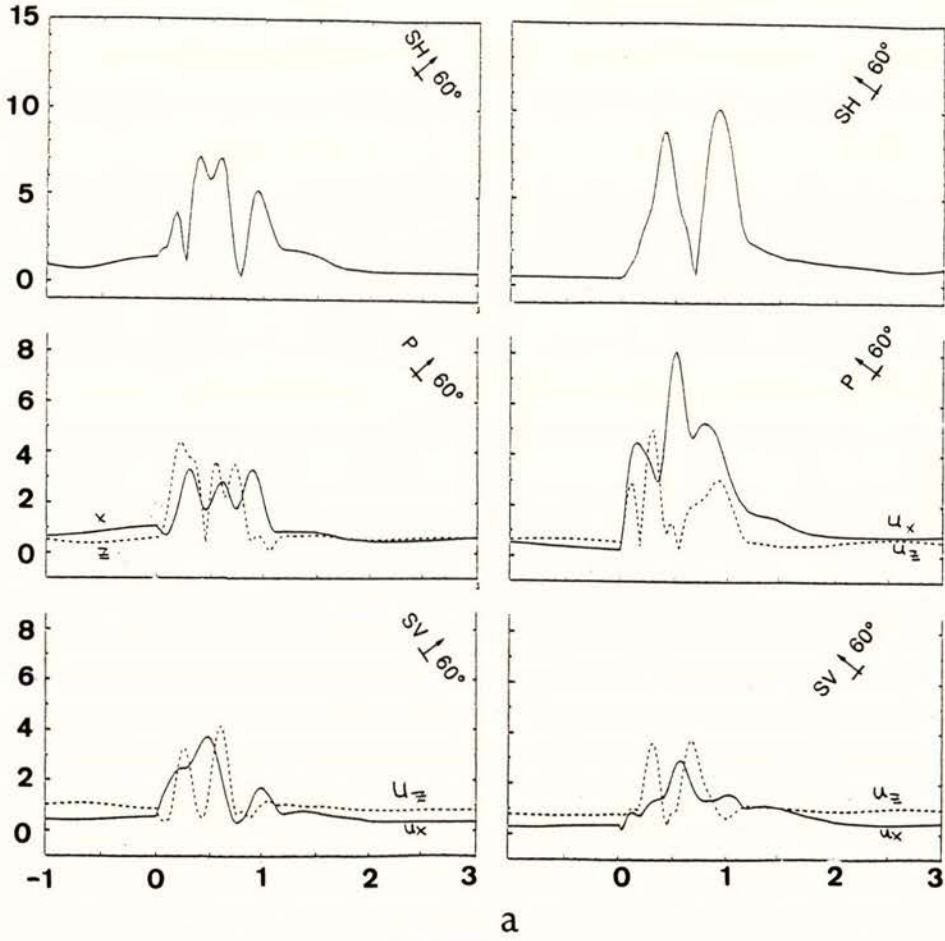


Figure 20. Amplitude distributions of the ground response for (a) *SH*, *P* and *SV* waves incident with angle  $\theta = 60^\circ$ , (b) for *SH* and *R* (Rayleigh) waves horizontally incident  $\theta = \pm 90^\circ$ .

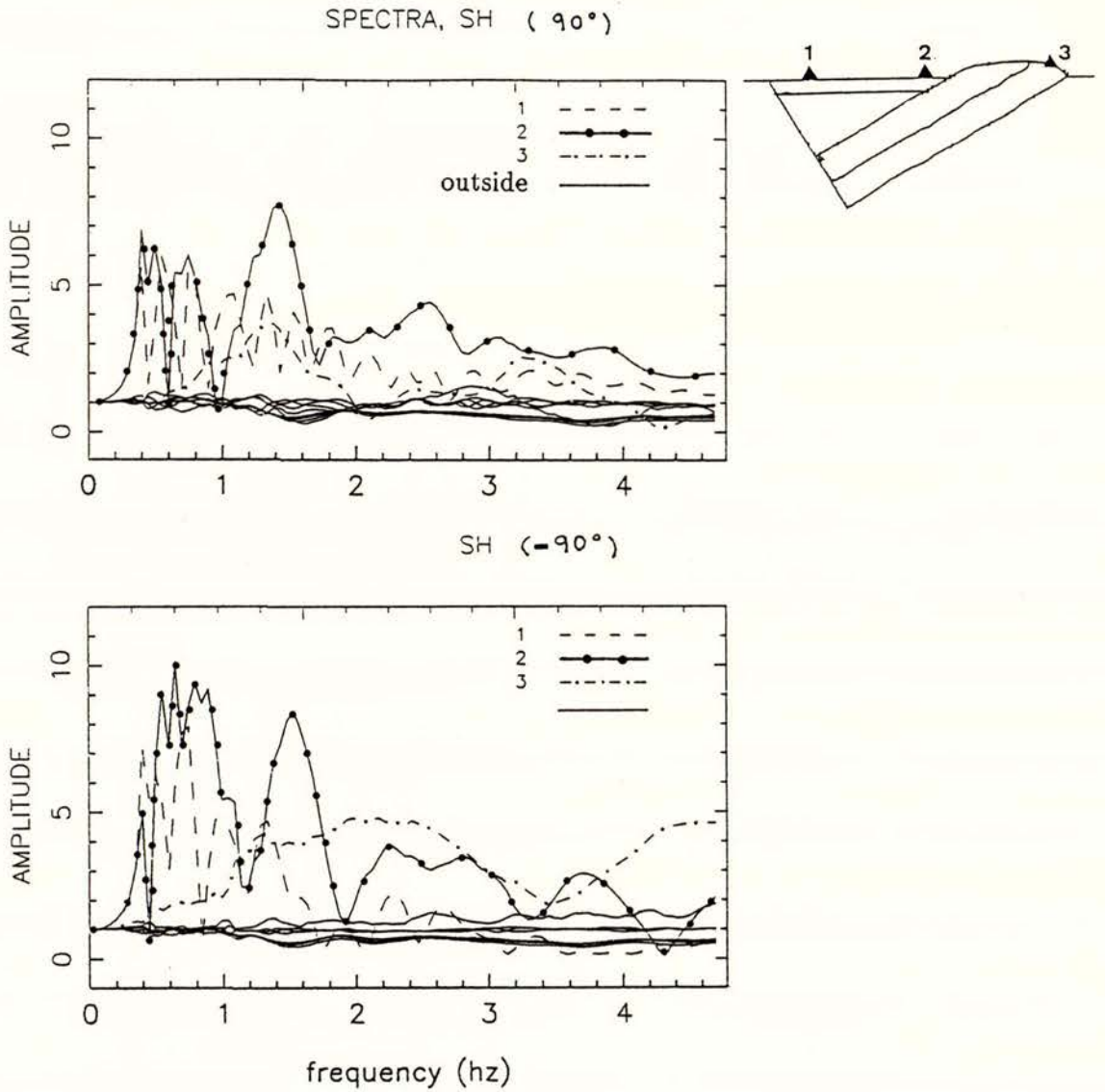
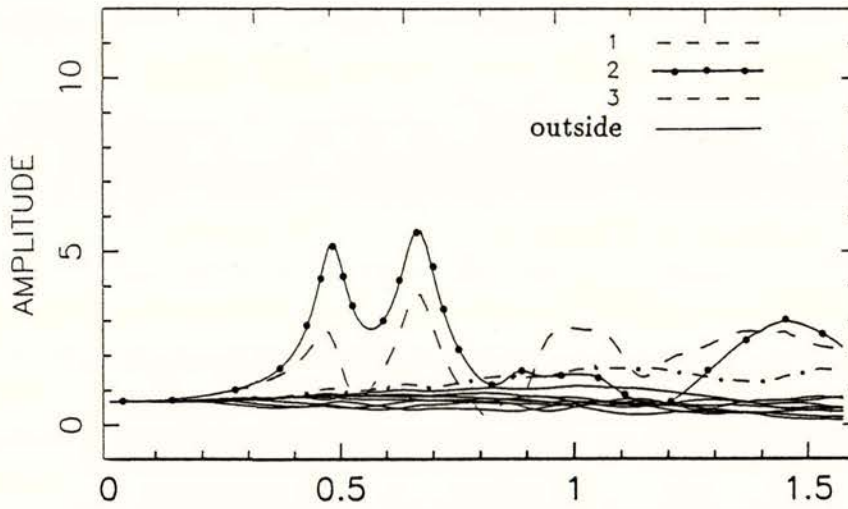


Figure 21. Frequency responses to horizontally incident  $SH$  waves  $\theta = \pm 90^\circ$  at three recording points, or stations, of the stratigraphy depicted in Figure 17. These stations, labelled as 1, 2 and 3 (top right), are located on the free-surface close to the left edge of the basin, at the center of the basin close to the foot of the ridge, and on the hill, respectively. The responses are computed for up to 4.78 Hz for each station, shown as dashed line for station 1, full line with dots for station 2 and dash-dotted line for station 3. Responses are also computed at six stations outside the basin (three at each side) shown by full lines.



SPECTRA,  $U_x$ , R,  $90^\circ$



SPECTRA,  $U_z$ , R,  $90^\circ$

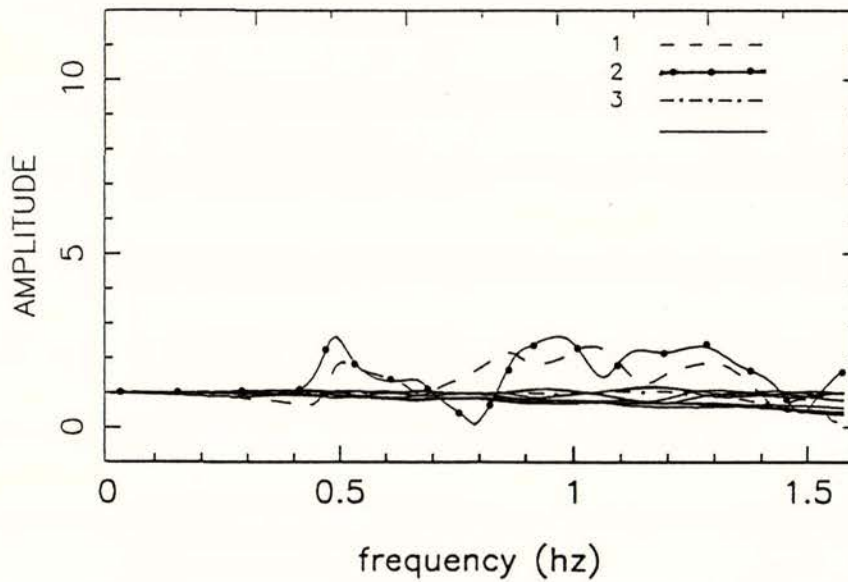


Figure 22. Responses of the stratigraphy depicted in Figure 17 to horizontally incident Rayleigh waves ( $\theta = \pm 90^\circ$ ), for up to 1.6 Hz. The station labels and response curves are identical to those of Figure 21.

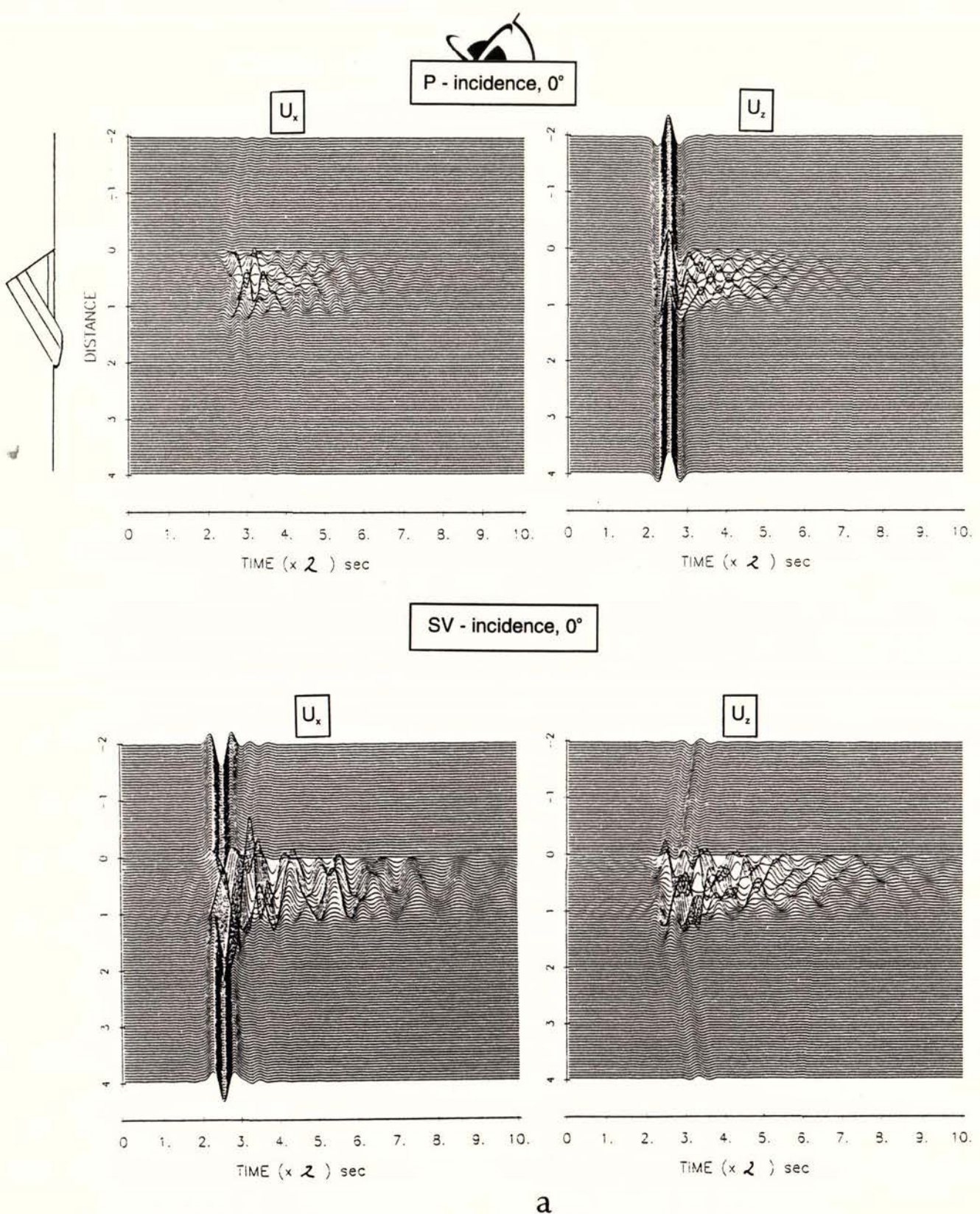
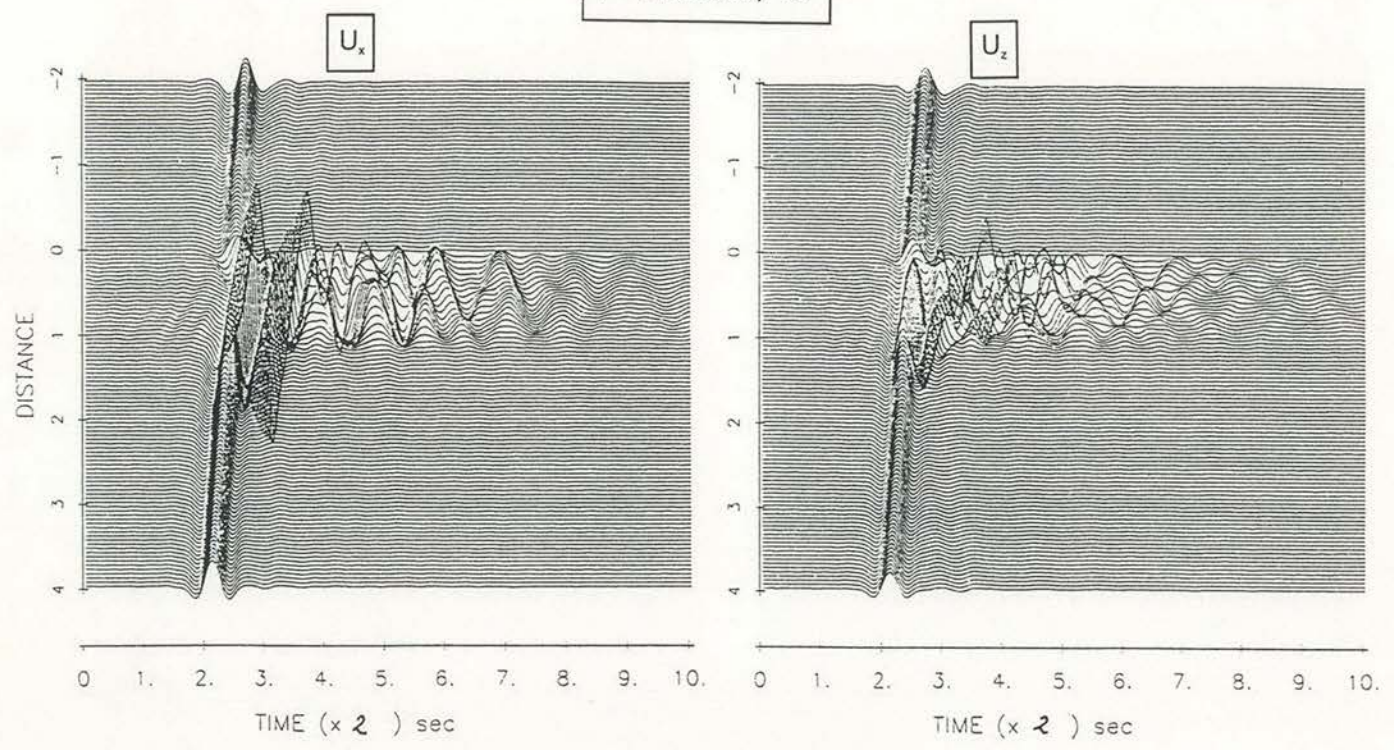


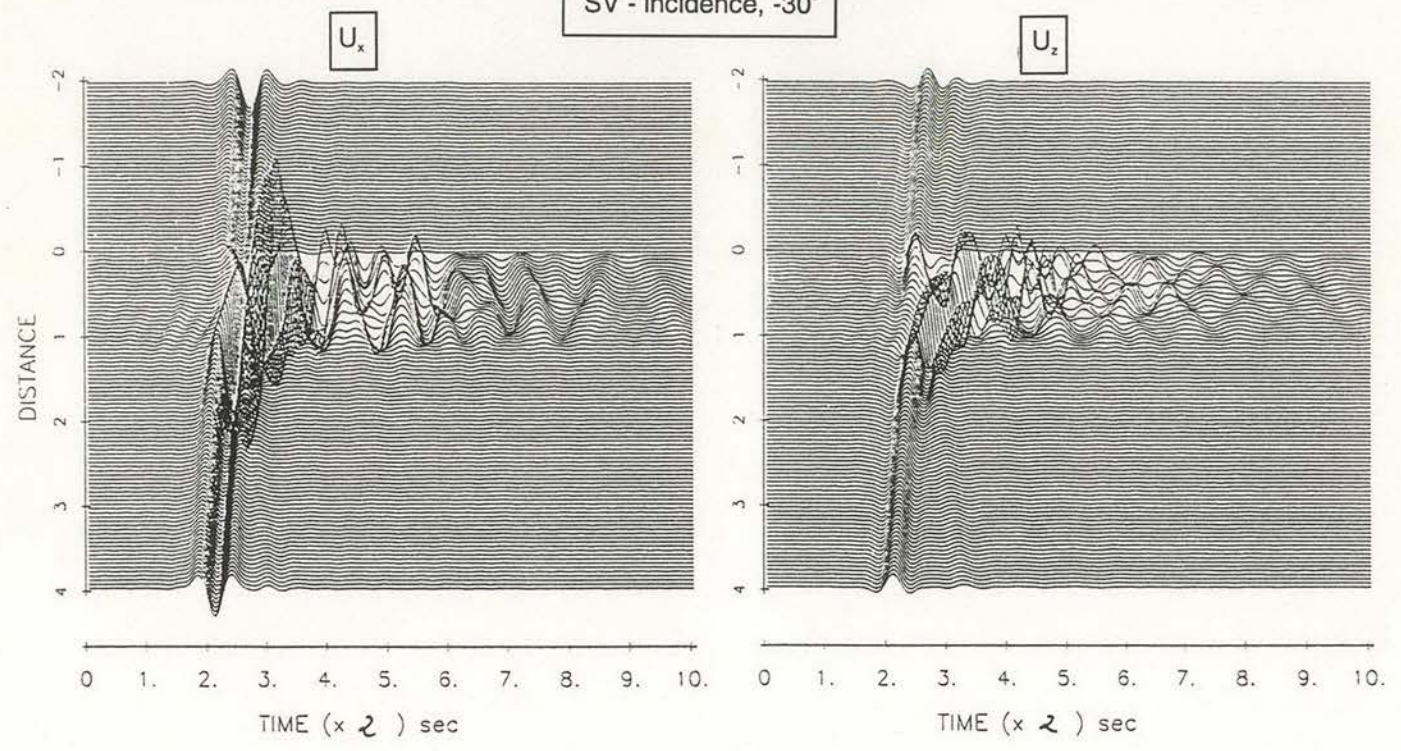
Figure 23. Time-domain responses (or synthetic seismograms) of the stratigraphy depicted in Figure 1. In general, these synthetic seismograms are computed at 120 stations along the free-surface between -2 and 4 km, using a Ricker wavelet as input source-time function, with peak frequency  $f_p = 1.42$  Hz. The total duration is 20 seconds. Synthetic seismograms of components  $U_x$  (horizontal) and  $U_z$  (vertical) are shown for (a) vertically incident  $P$  and  $SV$  waves, where the spatial range of the stratigraphy is depicted at the top left, (b)  $P$  incident with  $\theta = -60^\circ$  (top) and  $SV$  incident with  $\theta = -30^\circ$  (bottom) and (c) horizontally incident Rayleigh waves with  $\theta = \pm 90^\circ$ . The seismograms for a vertically incident  $SH$  wave and for horizontally incident  $SH$  waves with  $\theta = \pm 90^\circ$  are shown in (d), top and bottom, respectively. Apparent non-causal waves between 0 and 2 km are due to an artifact related to FFT periodicity.



P - incidence,  $-60^\circ$

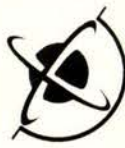


SV - incidence,  $-30^\circ$

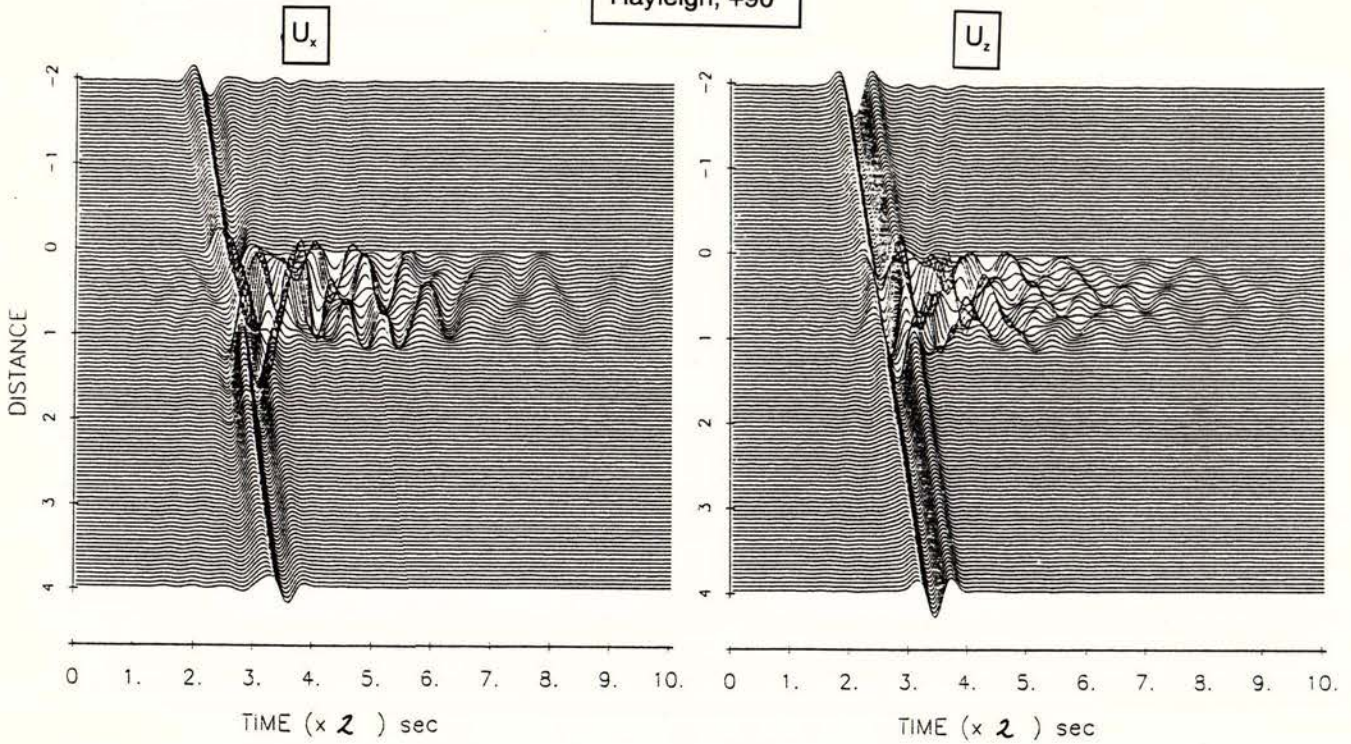


b

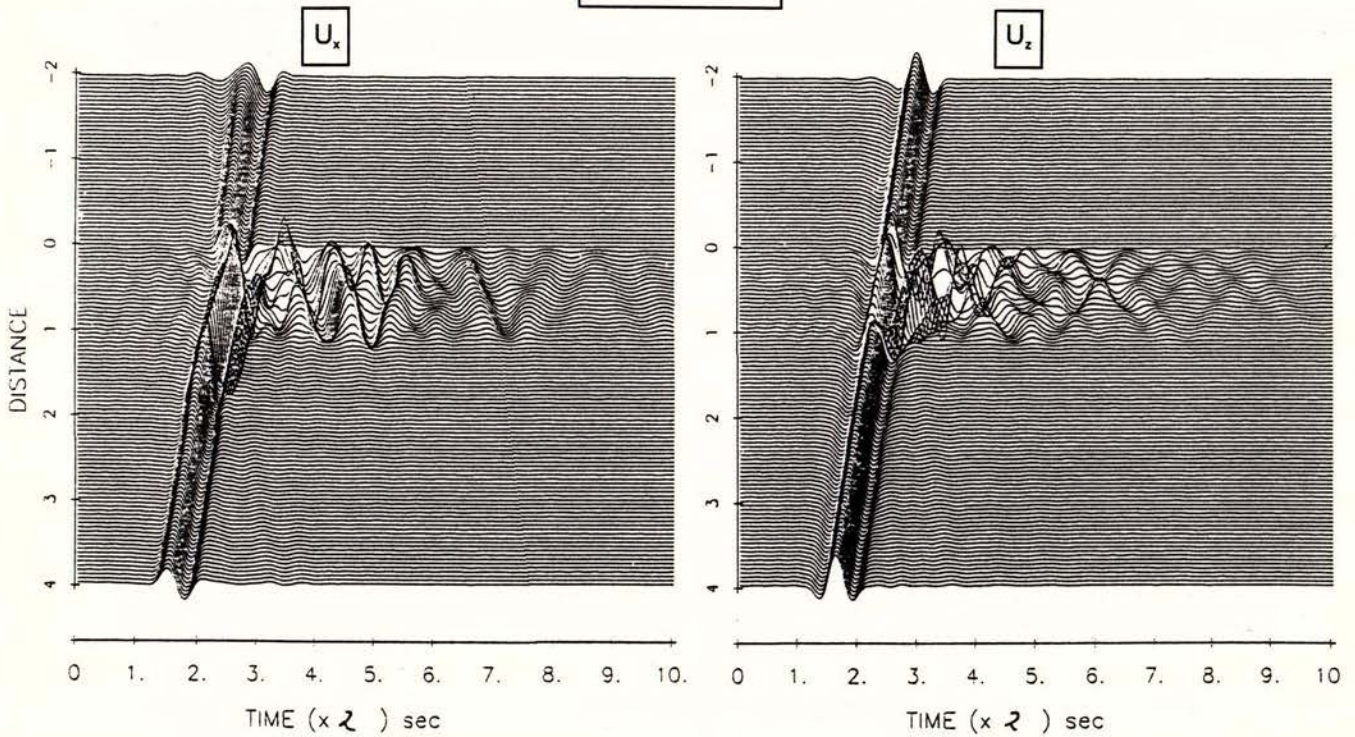
Figure 23 (continued).



Rayleigh, +90°

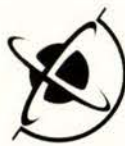


Rayleigh, -90°



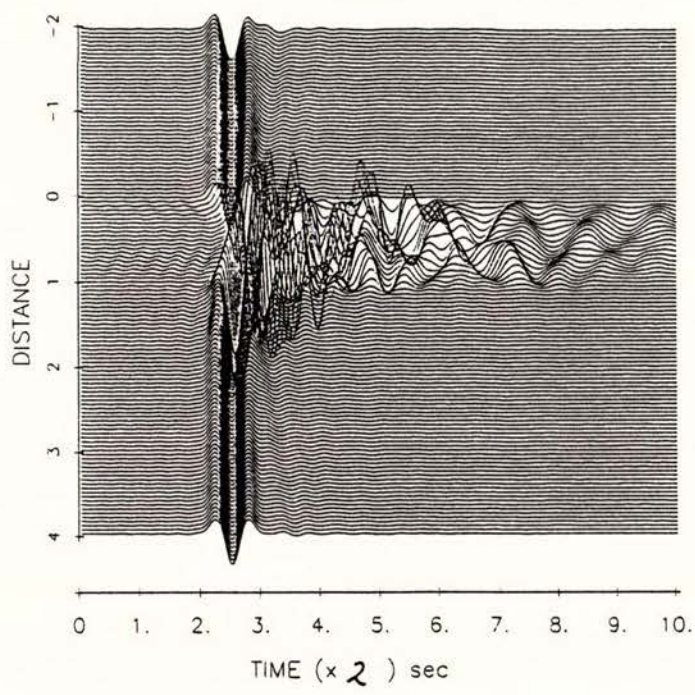
C

Figure 23 (continued).

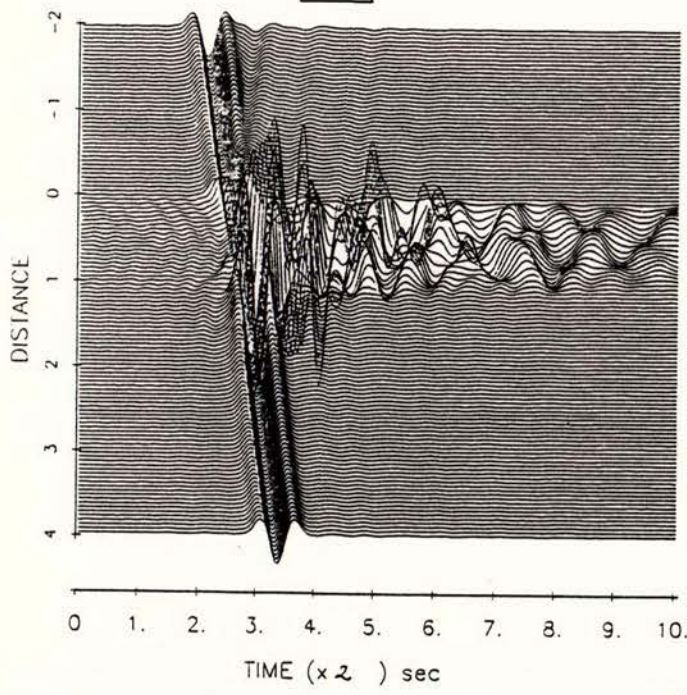


SH - incidence

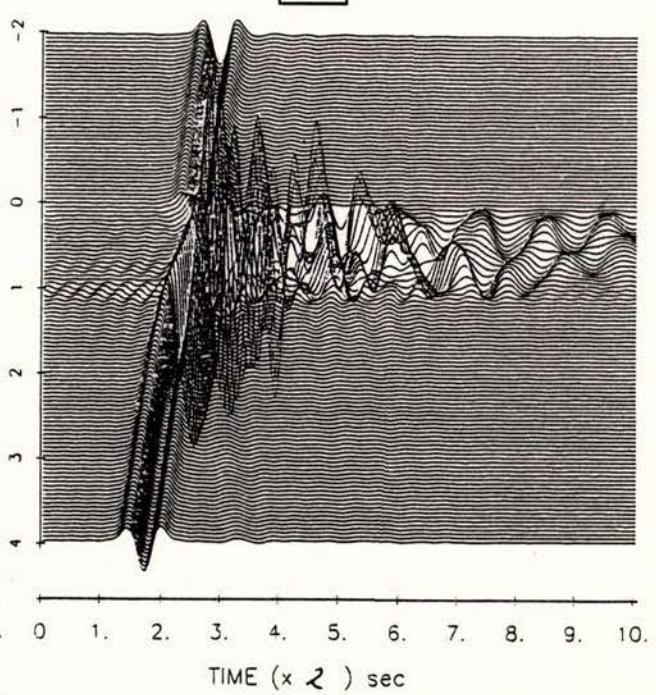
0°



+90°



-90°



d

Figure 23 (continued).



SH,  $-90^\circ$

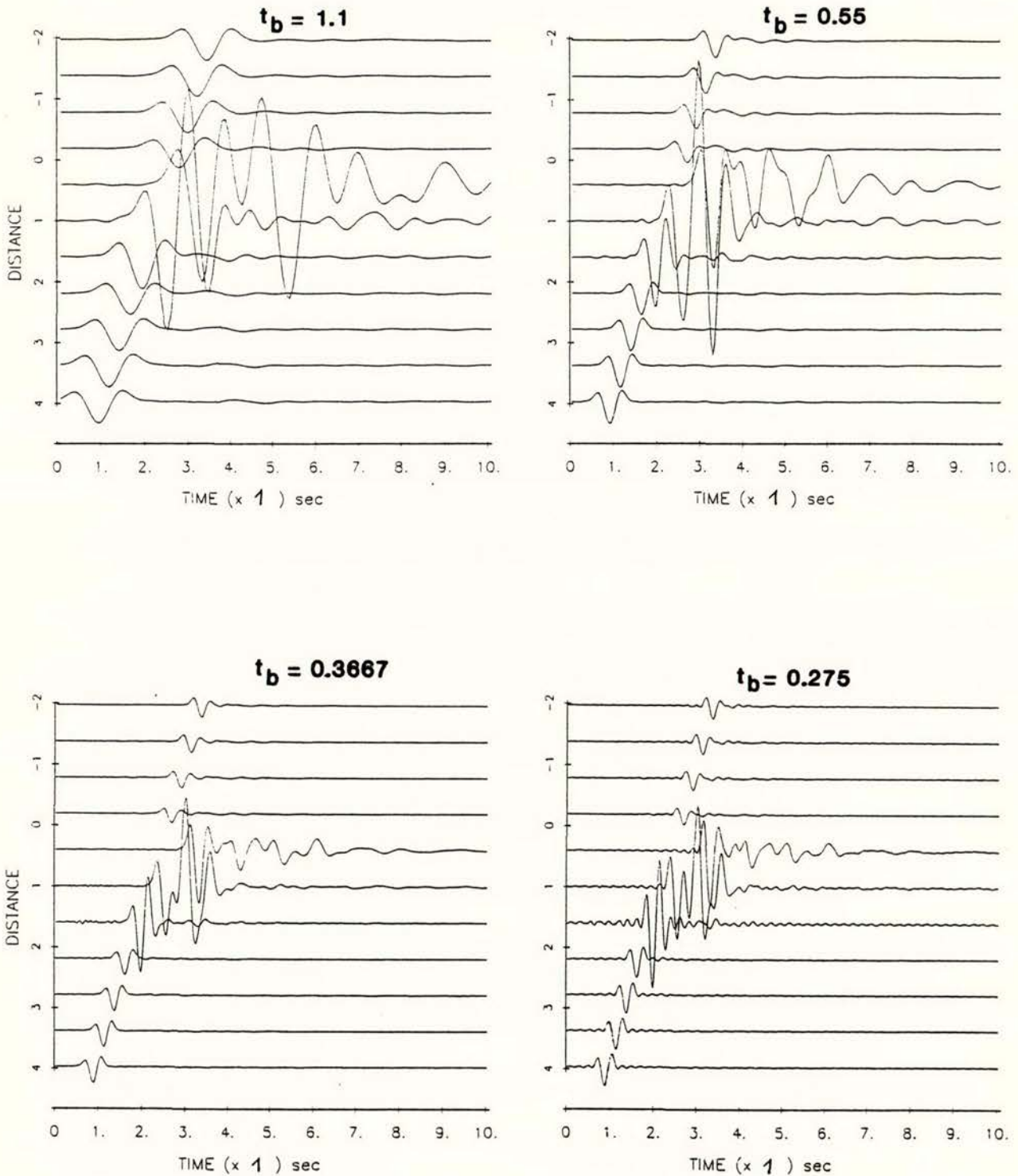


Figure 24. Synthetic seismograms for horizontally incident *SH* waves with  $\theta = \pm 90^\circ$ , computed at 11 stations along the free-surface between  $x = -2$  km and  $x = 4$  km (the stratigraphy depicted in Figure 17 extends between 0 and 2 km). The four sections correspond to four different values of breadth of Ricker wavelet, namely 1.1, 0.55, 0.3667 and 0.275 seconds, which in turn correspond to peak frequencies 0.71, 1.42, 2.84 and 2.13, respectively.

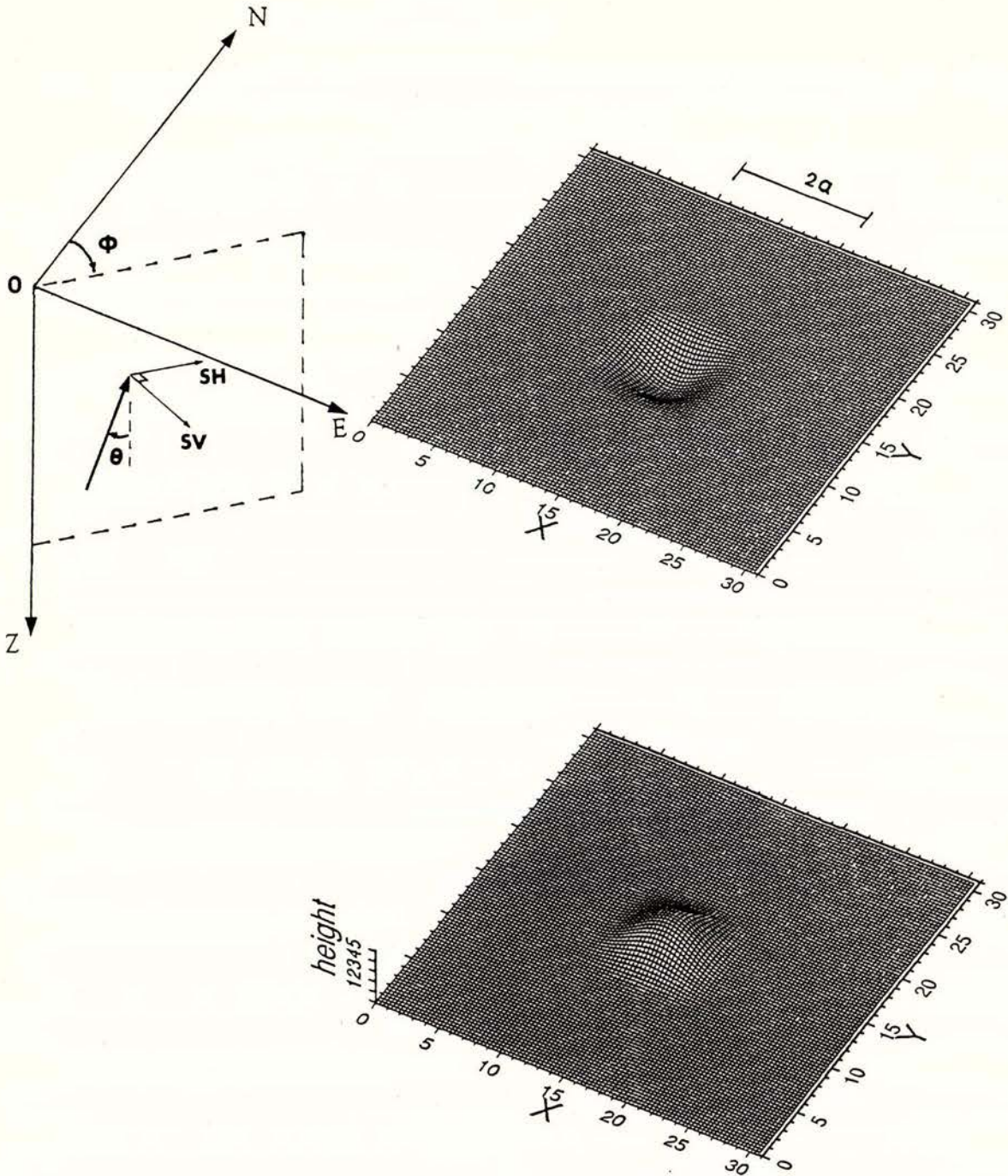


Figure 25. Three-dimensional (3-D) view of cosine-shaped topographic features corresponding to canyon (top) and mountain, or hill (bottom), referred to a Cartesian coordinate system  $E$ ,  $N$  and  $Z$  ( $Z$  positive down). The area where the 3-D topographic feature is defined is a square of side  $x = 31$  km. The base of the canyon (mountain) is also a square, of side 5 km, centred at  $x = 15$  km and  $y = 15$  km measured along  $X$  and  $Y$ , respectively. Its height is 3 km. The area is sampled by a grid of 100 points along  $X \times 100$  points along  $Y$ . The 3-D  $P$ ,  $SV$  and  $SH$  plane waves incident upon this topography are defined with respect to the coordinate system  $E$ ,  $N$ ,  $Z$ , with incident angle  $\theta$  measured clockwise from  $Z$ , and azimuthal angle  $\phi$  measured clockwise from  $N$ . The azimuthal angle defines a plane of incidence (dashed lines) in which the particle motions for  $P$ ,  $SV$  and  $SH$  are defined. For example, if  $\theta = 0$  and  $\phi = 0$ , then the  $P$  particle motion is in the  $z$  direction, the  $SV$  is in the  $E$  direction, and the  $SH$  is in the  $N$  direction.

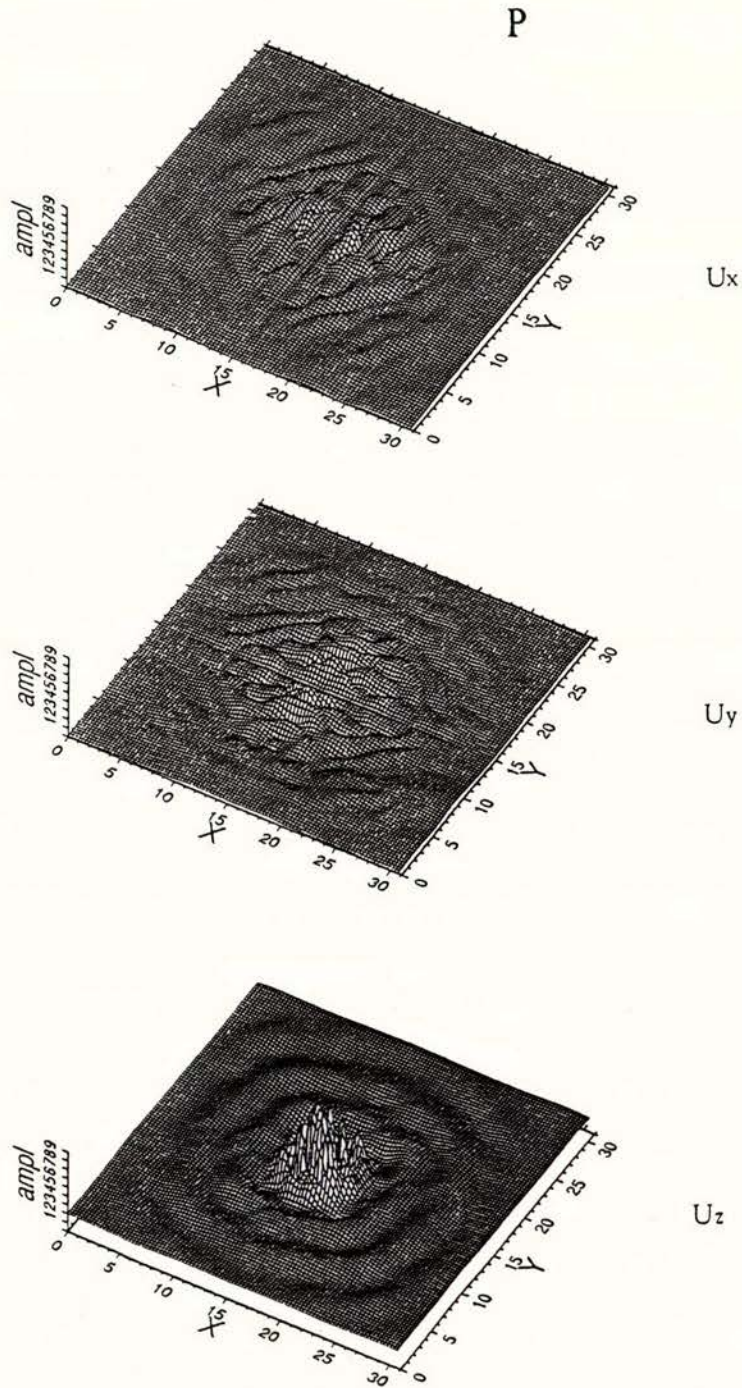
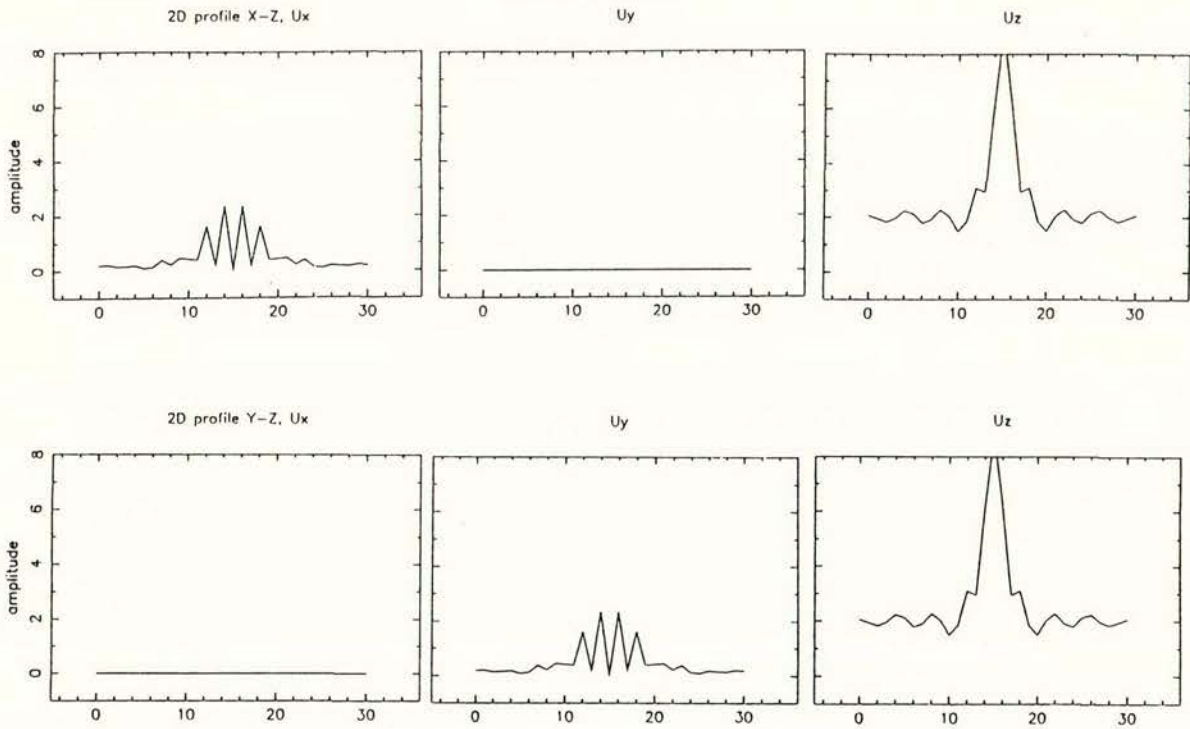


Figure 26. 3-D views of the amplitude distributions of the ground response of the mountain (or hill) described in Figure 25, to a vertically incident  $P$  wave. The motion is computed at each point of the grid, and the amplitudes are given in the same units of displacement as the incident wave. The top view corresponds to the horizontal component along  $X$ ,  $U_x$ , the middle to the horizontal component along  $Y$ ,  $U_y$ , and the bottom to the vertical component  $U_z$ . The input wavelength is equal to 5 km, (i.e one-half of the side of the squared base), corresponding to a non-dimensional frequency  $\eta = 2a/\lambda = 2$ .  $U_x$  and  $U_y$  exhibit nodal lines (zero amplitudes) at  $x = 15$  km and  $y = 15$  km, respectively, showing that both components are equivalent, as expected from the symmetry of the incident wave.



Hill, P,  $\theta = 0^\circ$

$x = 15, y = 15$



$x = 12, y = 12$

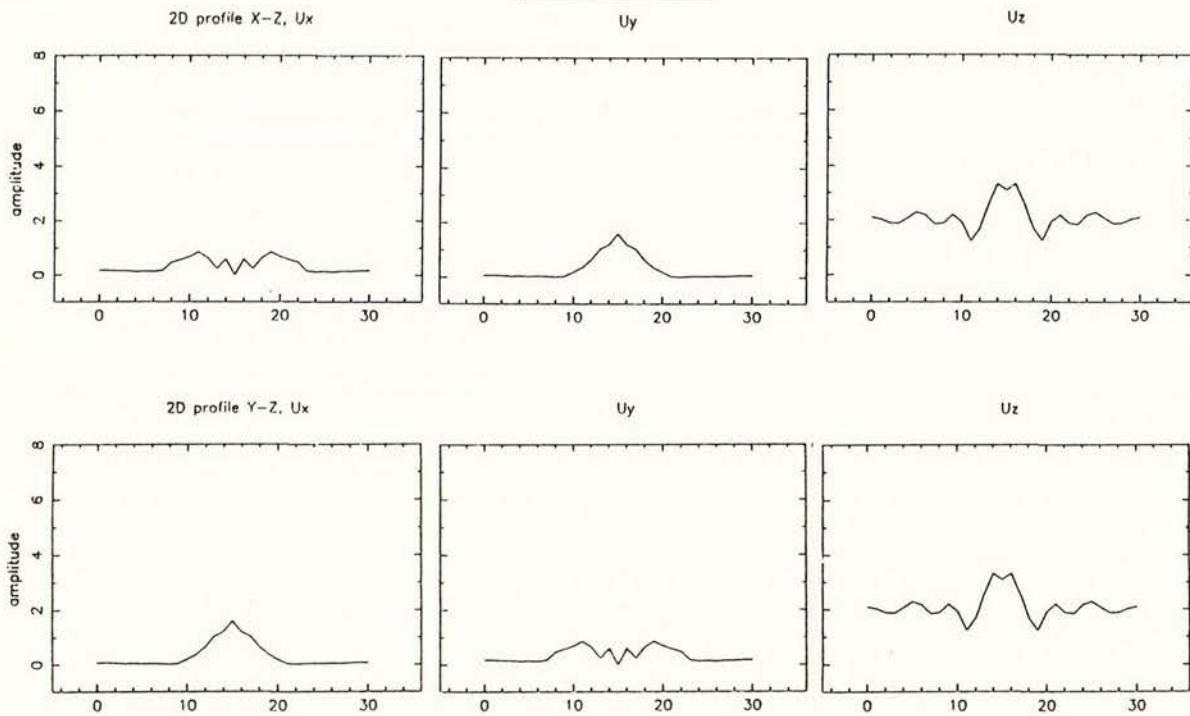


Figure 27. Amplitude distributions of the ground motion along two two-dimensional (2-D) profiles cut at the center point (top two rows), and at a point  $x = 12$  km,  $y = 12$  km of the 3-D views of Figure 26. For each point, the profiles  $X-Z$  and  $Y-Z$  are perpendicular, intersecting at that point. The mountain extends from 10 to 20 km.

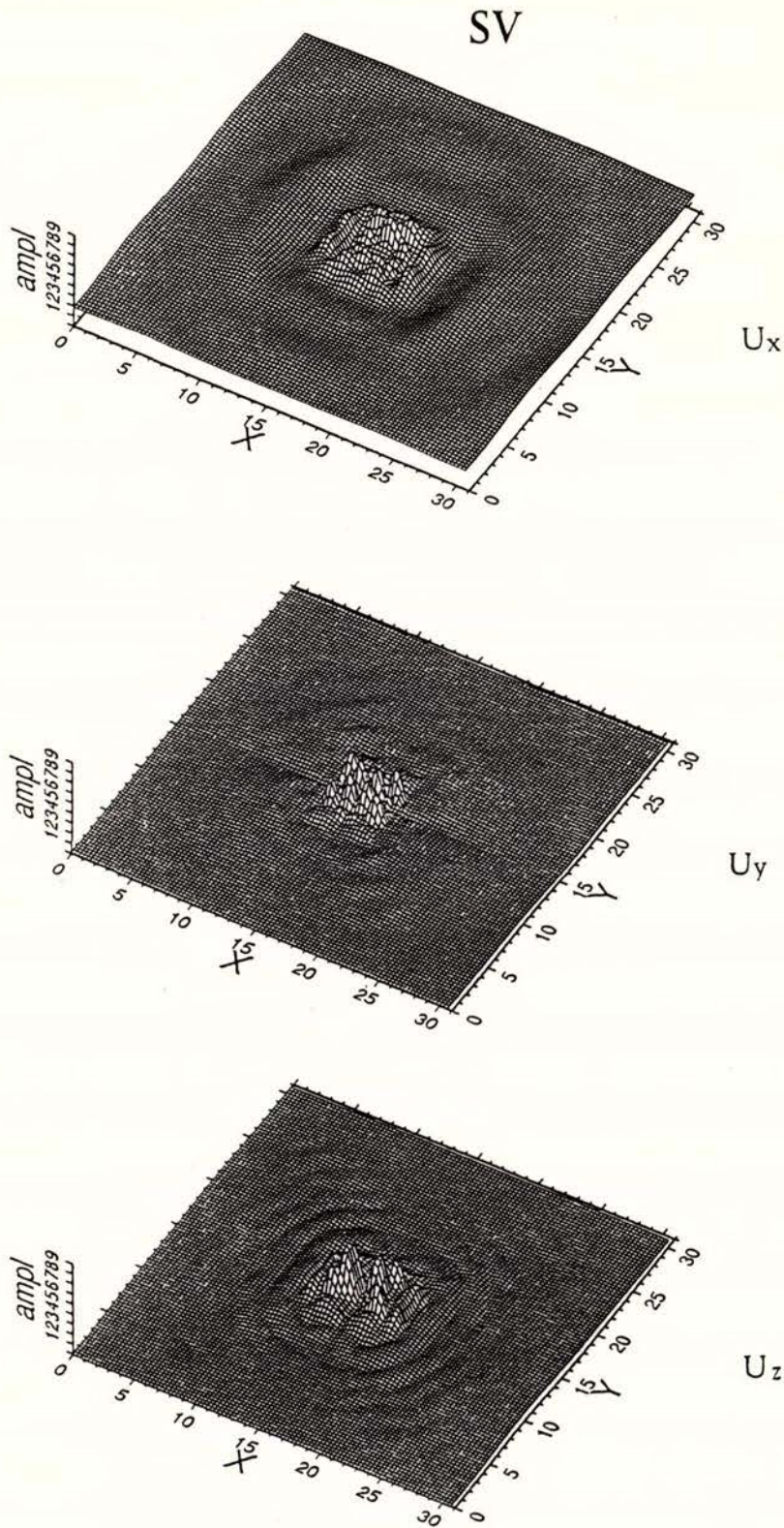
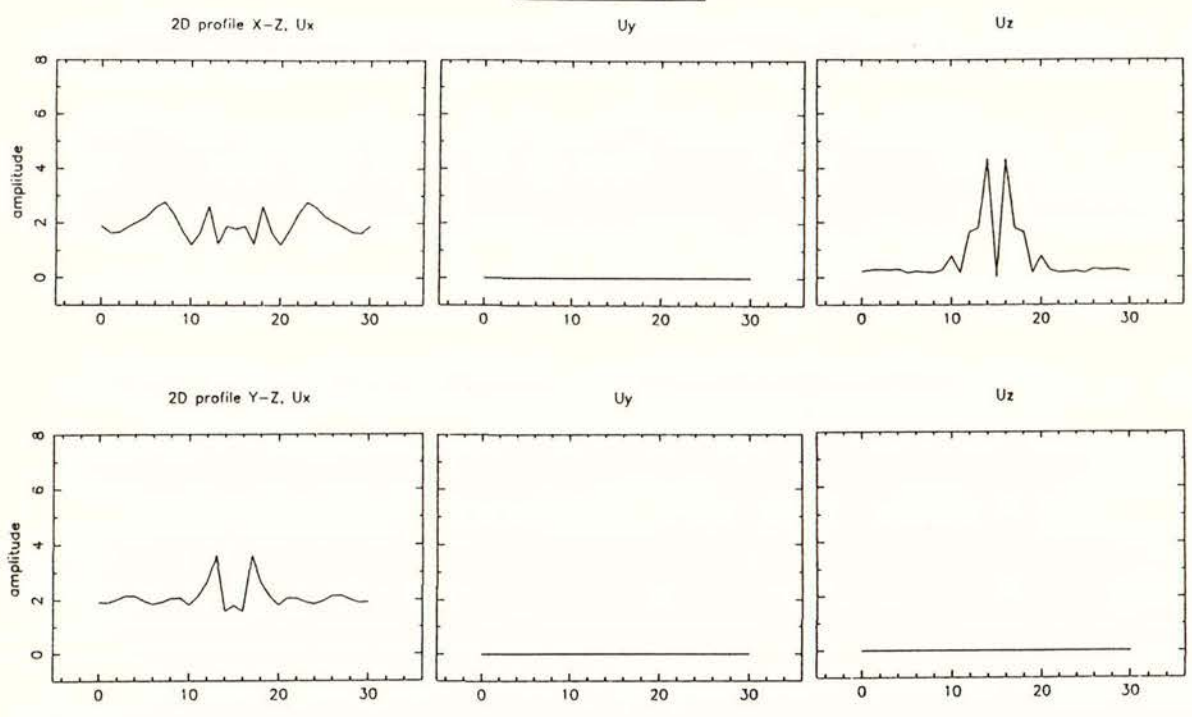


Figure 28. 3-D views of the amplitude distributions of the ground response of the mountain described in Figure 25, to a vertically incident *SV* wave, with azimuthal angle  $\phi = 0$ .



Hill, SV,  $\theta = 0^\circ$

$x = 15, y = 15$



$x = 12, y = 12$

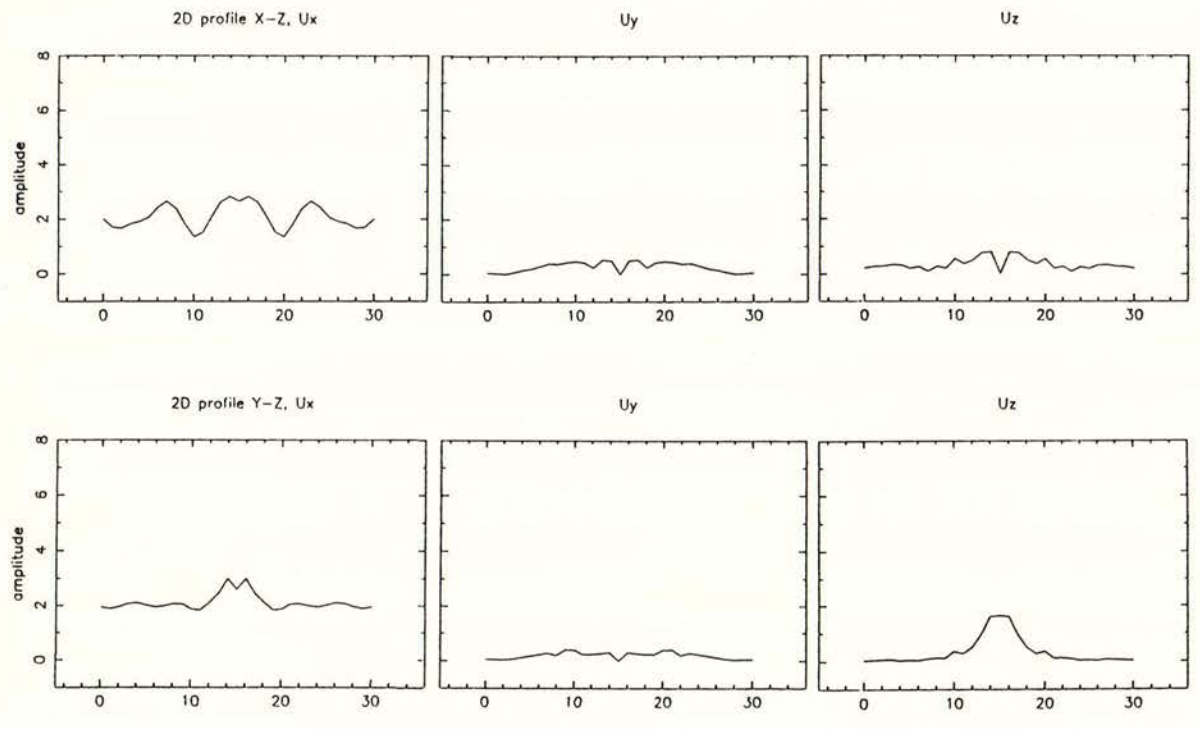
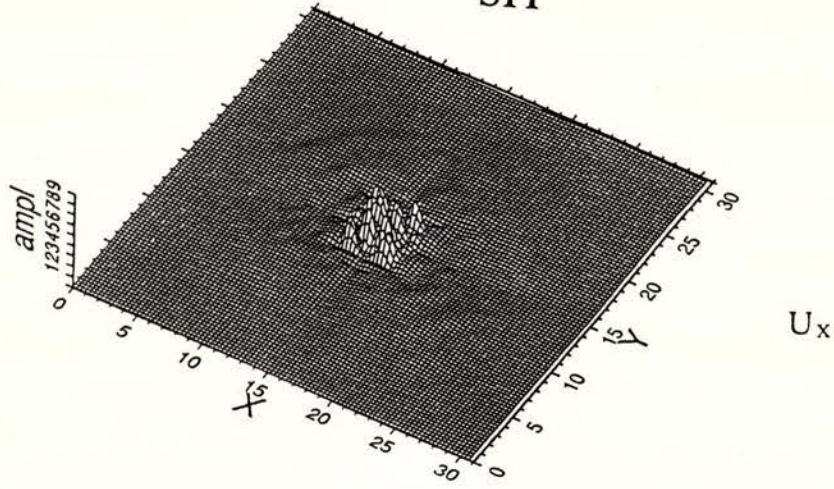


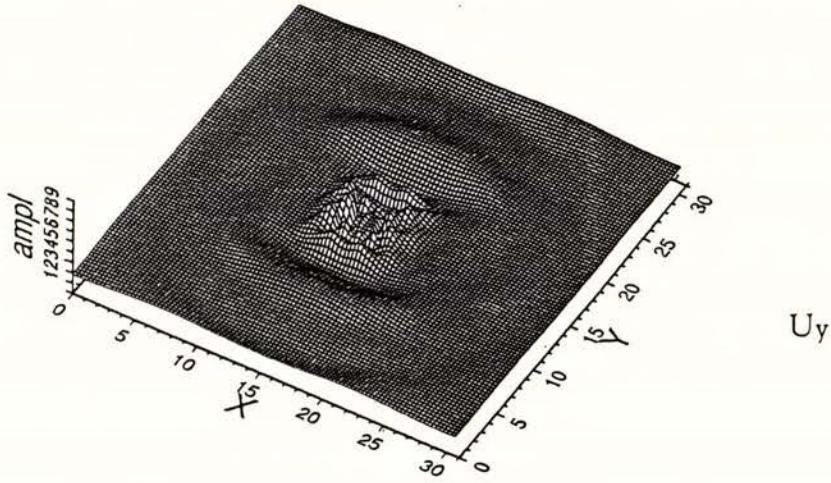
Figure 29. Amplitude distributions of the ground motion along two 2-D perpendicular profiles (described in Figure 27) of the 3-D ground motion due to a vertically incident SV wave, shown in Figure 28.



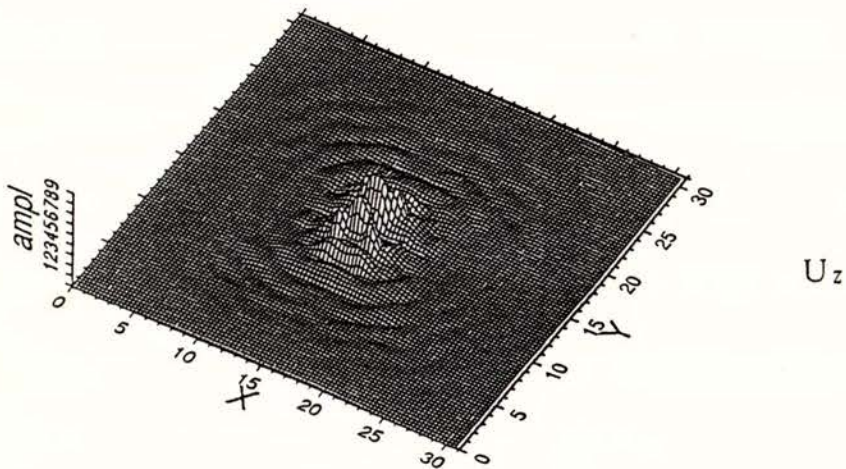
SH



$U_x$



$U_y$



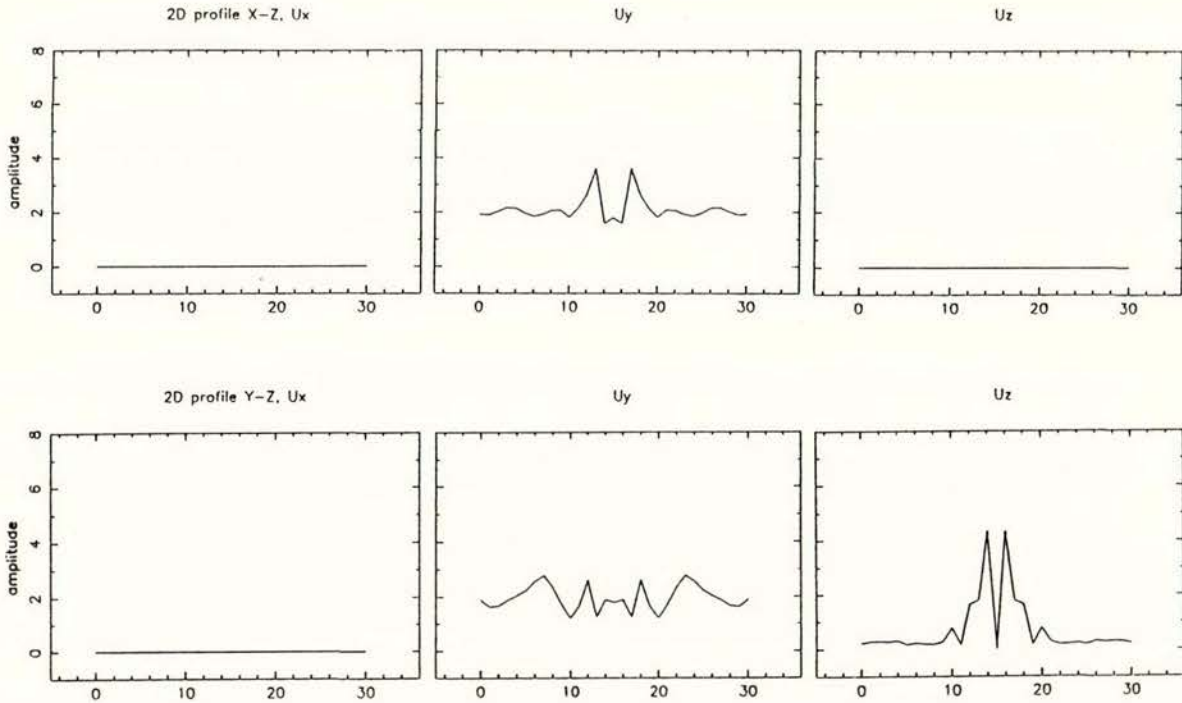
$U_z$

Figure 30. 3-D views of the amplitude distributions of the ground response of the mountain described in Figure 25, to a vertically incident  $SH$  wave, with azimuthal angle  $\phi = 0$ . Comparing them with those of Figure 28, the  $SH$  vertical incidence in this case is equivalent to the  $SV$  vertical incidence with azimuthal angle  $\phi = 90^\circ$ , as it is expected.



Hill, SH,  $\theta = 0^\circ$

$x = 15, y = 15$



$x = 12, y = 12$

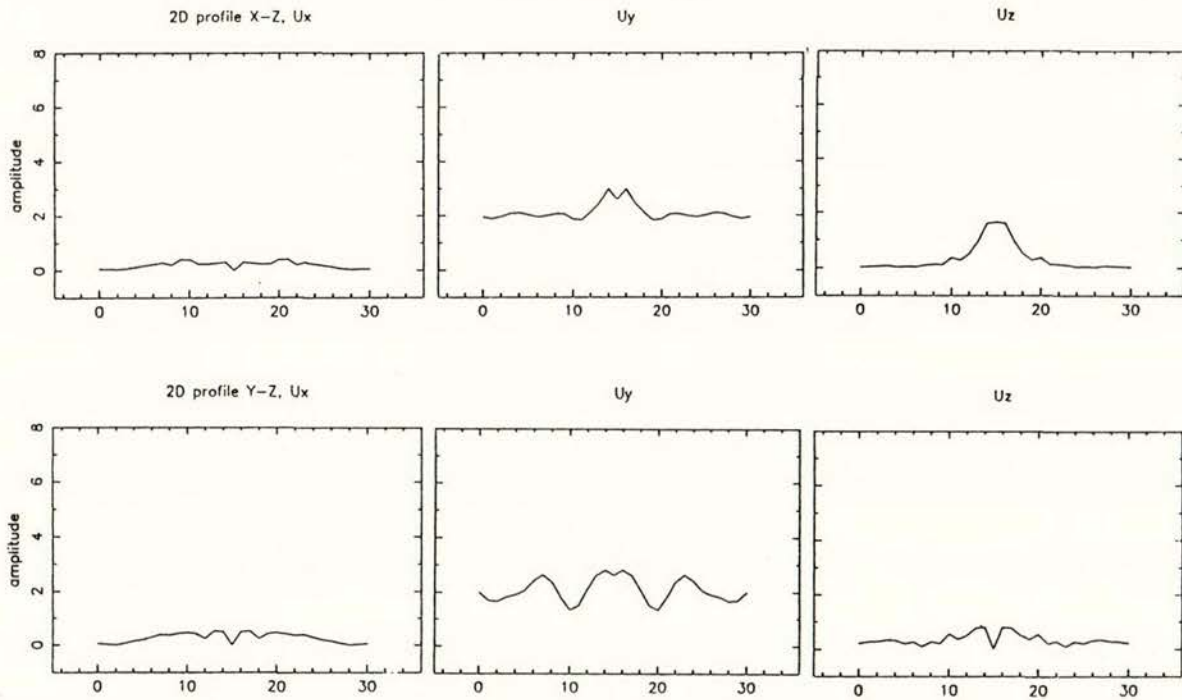


Figure 31. Amplitude distributions of the ground motion along two 2-D perpendicular profiles (described in Figure 27) of the 3-D ground motion due to a vertically *SH* wave, shown in Figure 30. Comparisons with the corresponding motions for an *SV* vertically incident in Figure 29 show that this case of *SH* incidence is equivalent to the *SV* vertical incidence with azimuthal angle  $\phi = 90^\circ$ .

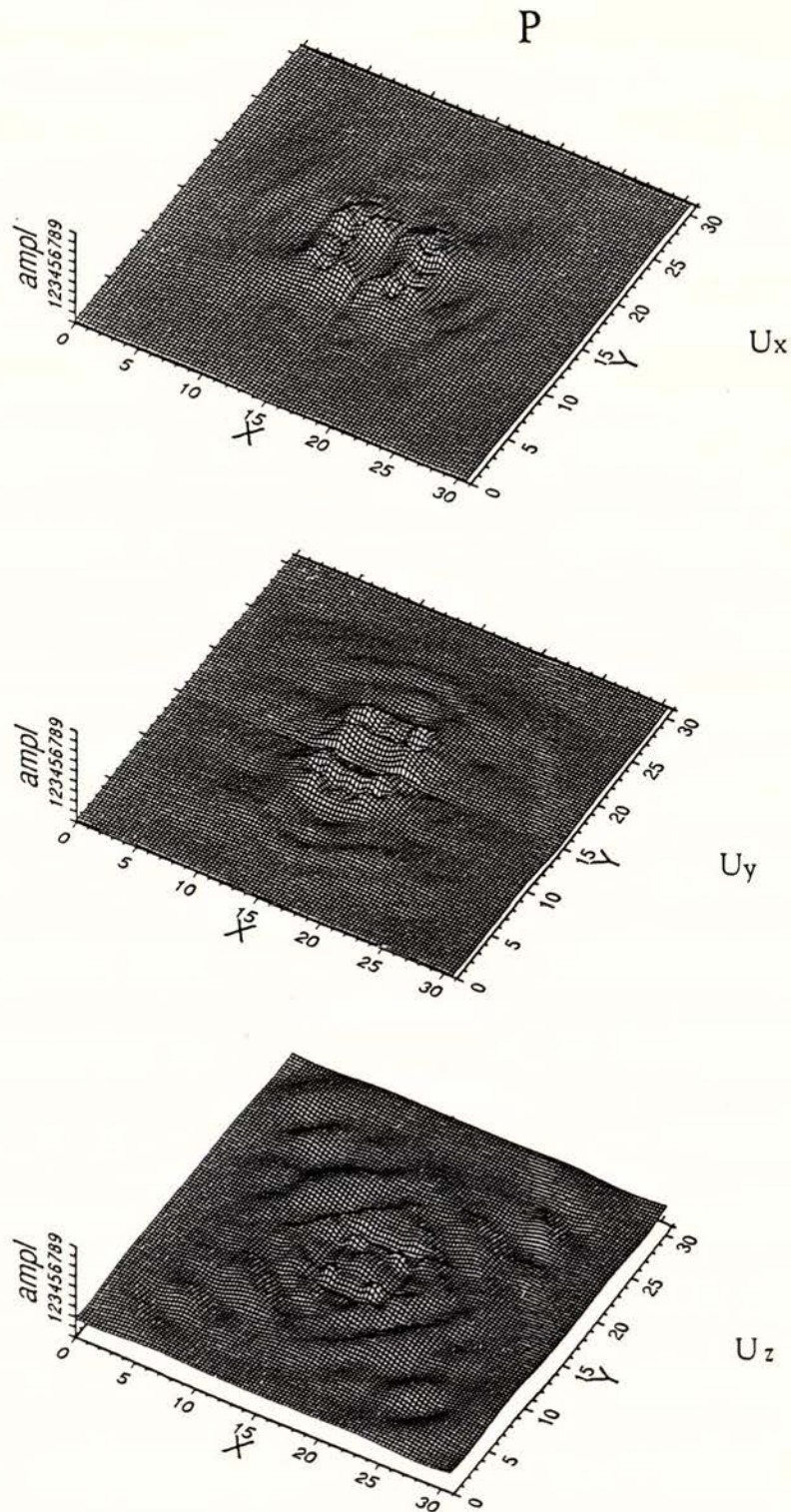
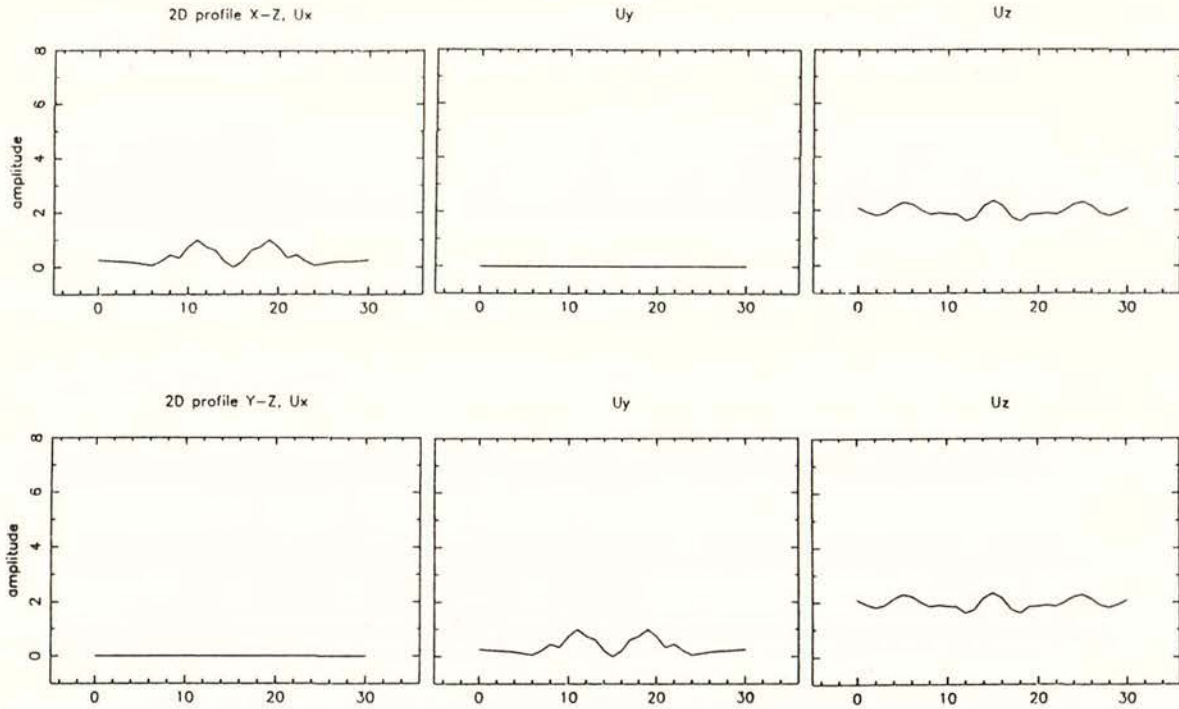


Figure 32. 3-D views of the amplitude distributions of the ground response of the canyon described in Figure 25, to a vertically incident  $P$  wave. As in the case of a mountain, here the input wavelength is 5 km ( $\eta = 2$ ). The top view corresponds to the horizontal component of motion  $U_x$ , the middle to the horizontal  $U_y$ , and the bottom to the vertical  $U_z$ .  $U_x$  and  $U_y$  exhibit nodal lines (zero amplitudes) at  $x = 15$  km and  $y = 15$  km, respectively, showing that both components are equivalent, as expected from the symmetry of the incident wave.



Canyon, P,  $\theta = 0^\circ$

$x = 15, y = 15$



$x = 12, y = 12$

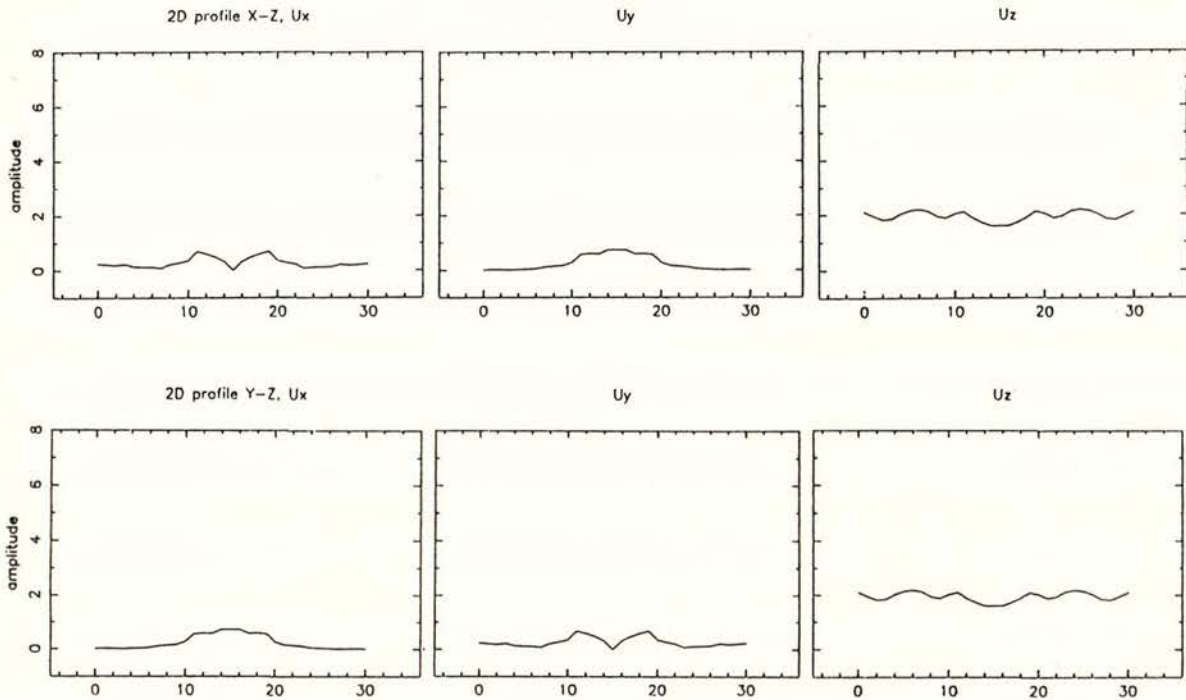


Figure 33. Amplitude distributions of the ground motion along two 2-D perpendicular profiles (described in Figure 27) of the 3-D ground motion due to a vertically P wave, shown in Figure 32. The nodal lines are observed for the profile at the center of the canyon. Note the equivalence of the horizontal components for both profiles.

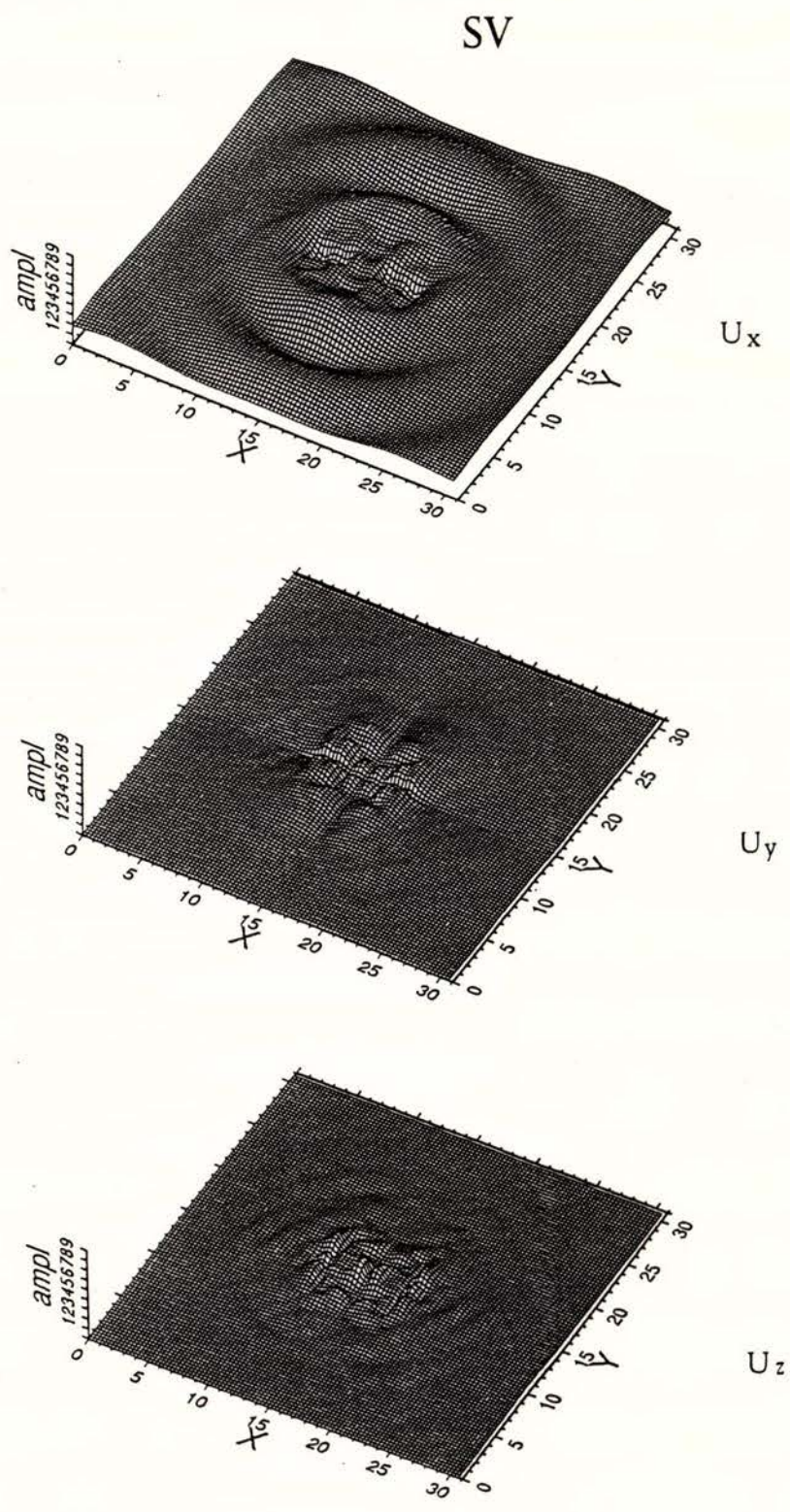


Figure 34. 3-D views of the amplitude distributions of the ground response of the canyon described in Figure 25, to a vertically incident *SV* wave with azimuthal angle  $\phi = 0$  ( $\eta = 1.5$ ). No nodal lines are observed for  $U_x$ , but  $U_y$  cancels out along the perpendicular profiles intersecting at  $x = 15$  km and  $y = 15$  km, and  $U_z$  along  $x = 15$  km.

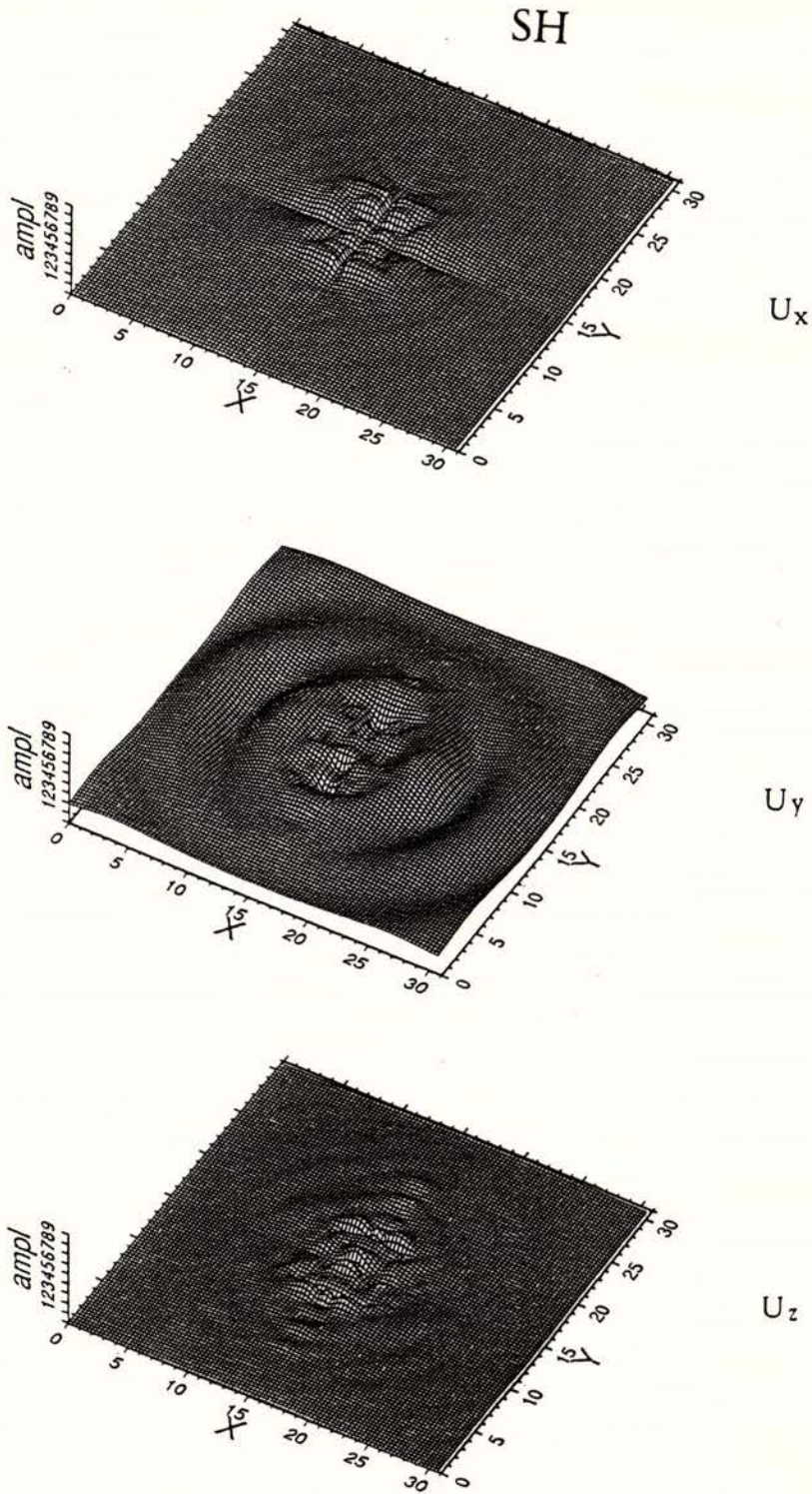
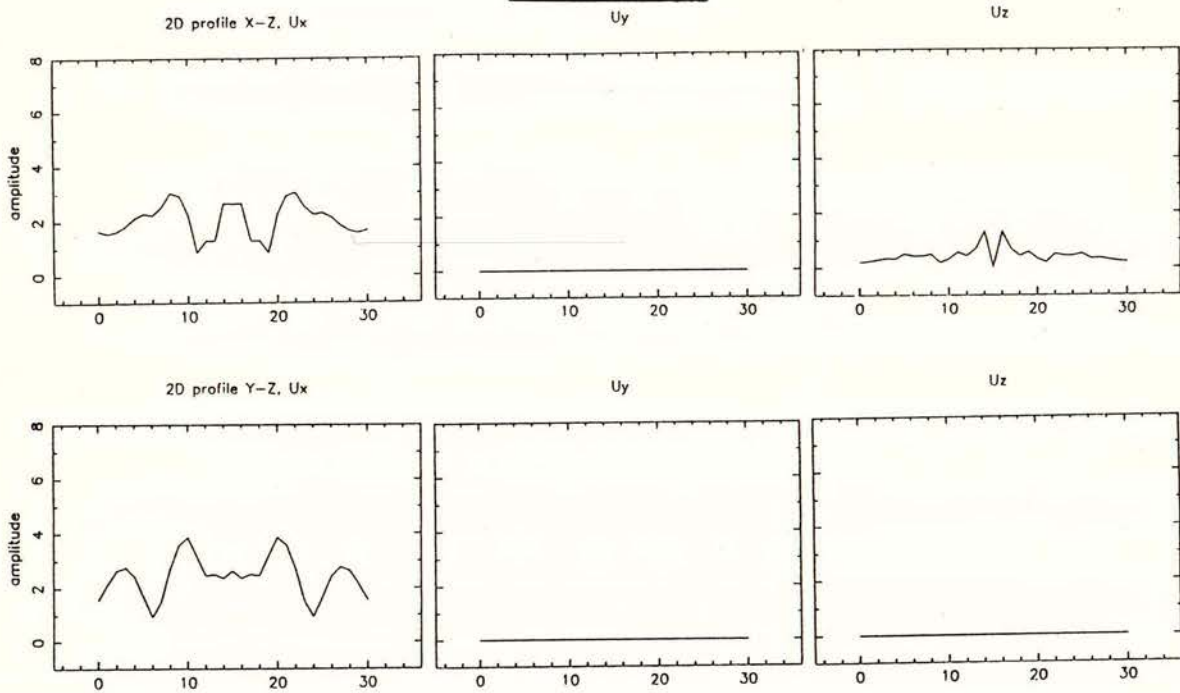


Figure 35. 3-D views of the amplitude distributions of the ground response of the canyon described in Figure 25, to a vertically incident *SH* wave with azimuthal angle  $\phi = 0$  ( $\eta = 1.5$ ). Note that the motions are equivalent to those corresponding to an *SV* vertically incident with azimuthal angle  $\phi = 90^\circ$ .



Canyon, SV,  $\theta = 0^\circ$

$x = 15, y = 15$



$x = 12, y = 12$

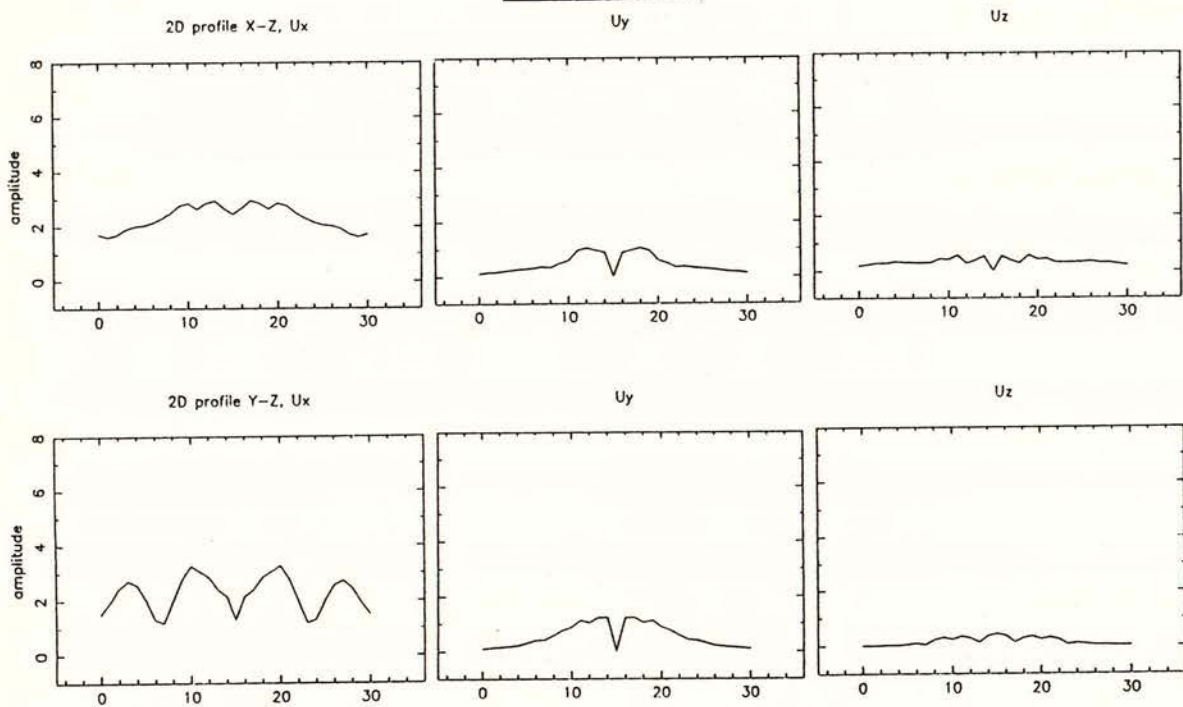
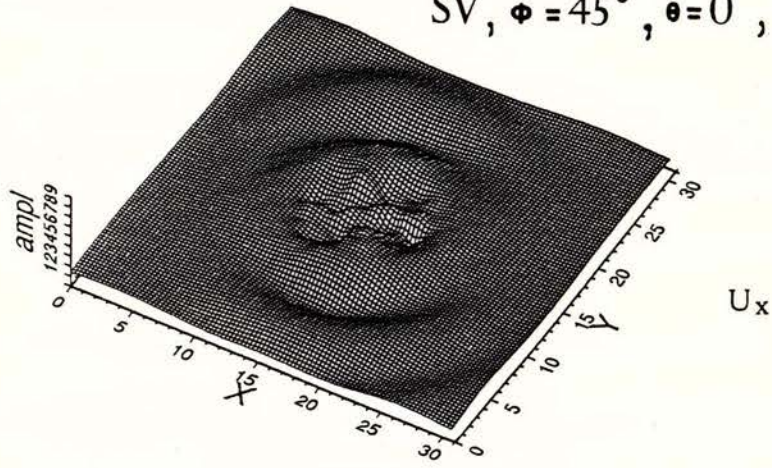


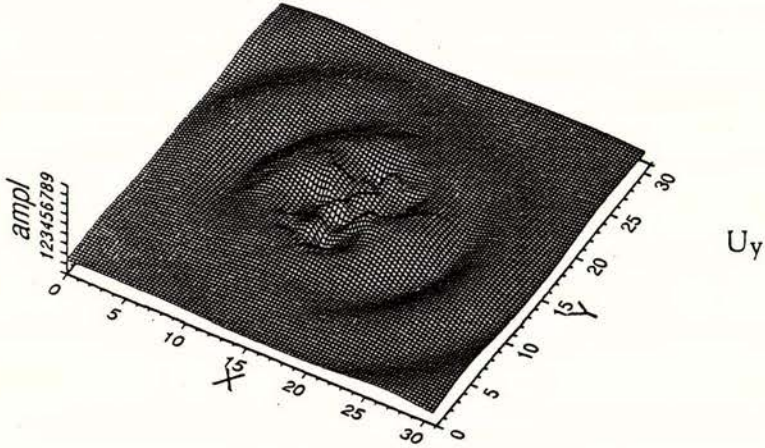
Figure 36. Amplitude distributions of the ground motion along two 2-D perpendicular profiles (described in Figure 27) of the 3-D ground motion due to a vertically incident SV wave, shown in Figure 34. The profiles intersecting at the center of the canyon show the cancellation of  $U_y$  along the X-Z and cancellation of both  $U_x$  and  $U_z$  along Y-Z. In that case, the components  $U_x$  and  $U_z$  along X-Z resemble the response (computed with 2-D methods) of a cosine-shaped 2-D canyon with similar dimensions for an incident SV wave (Bouchon 1973). Similarly, the component  $U_x$  along Y-Z resembles the response of a 2-D canyon to an incident SH wave. The responses along the profiles passing through  $x = 12$  km,  $y = 12$  km do not resemble the 2-D responses at all.



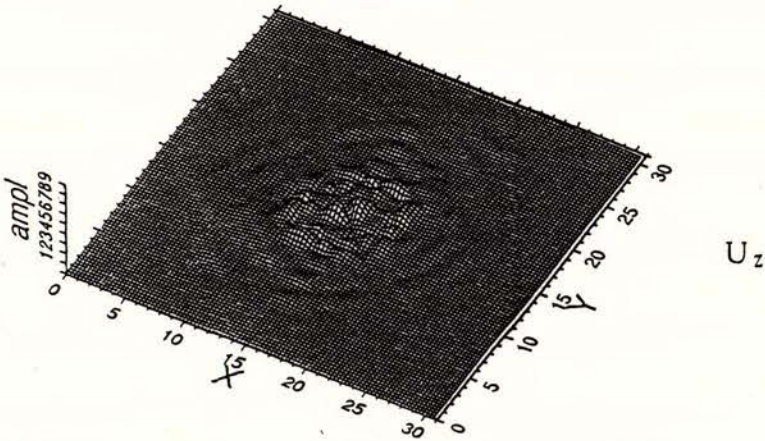
$SV, \phi = 45^\circ, \theta = 0, \eta = 1.5$



$U_x$



$U_y$



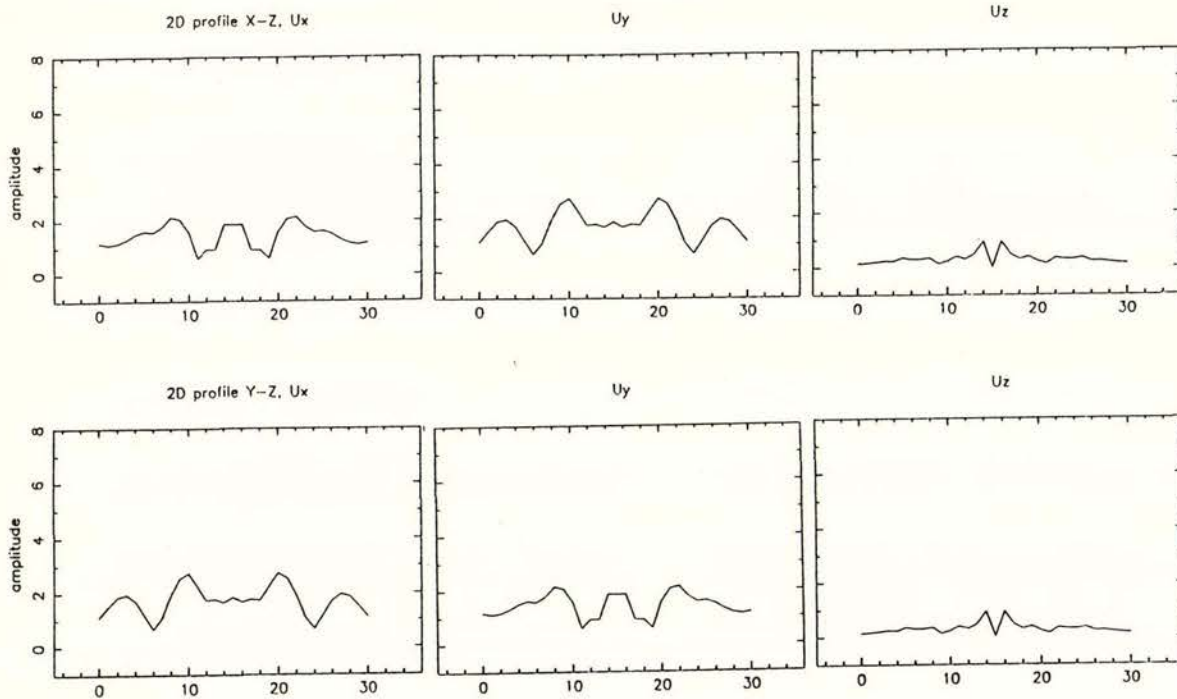
$U_z$

Figure 37. 3-D views of the amplitude distributions of the ground response of the canyon described in Figure 25, to a vertically incident  $SV$  wave with azimuthal angle  $\phi = 45^\circ$  ( $\eta = 1.5$ ). The nodal lines observed for the case of  $\phi = 0$  (Figure 34) disappear, and the motions of both horizontal components become the same.



Canyon, SV,  $\theta = 0^\circ$ ,  $\phi = 45^\circ$

$x = 15$ ,  $y = 15$



$x = 12$ ,  $y = 12$

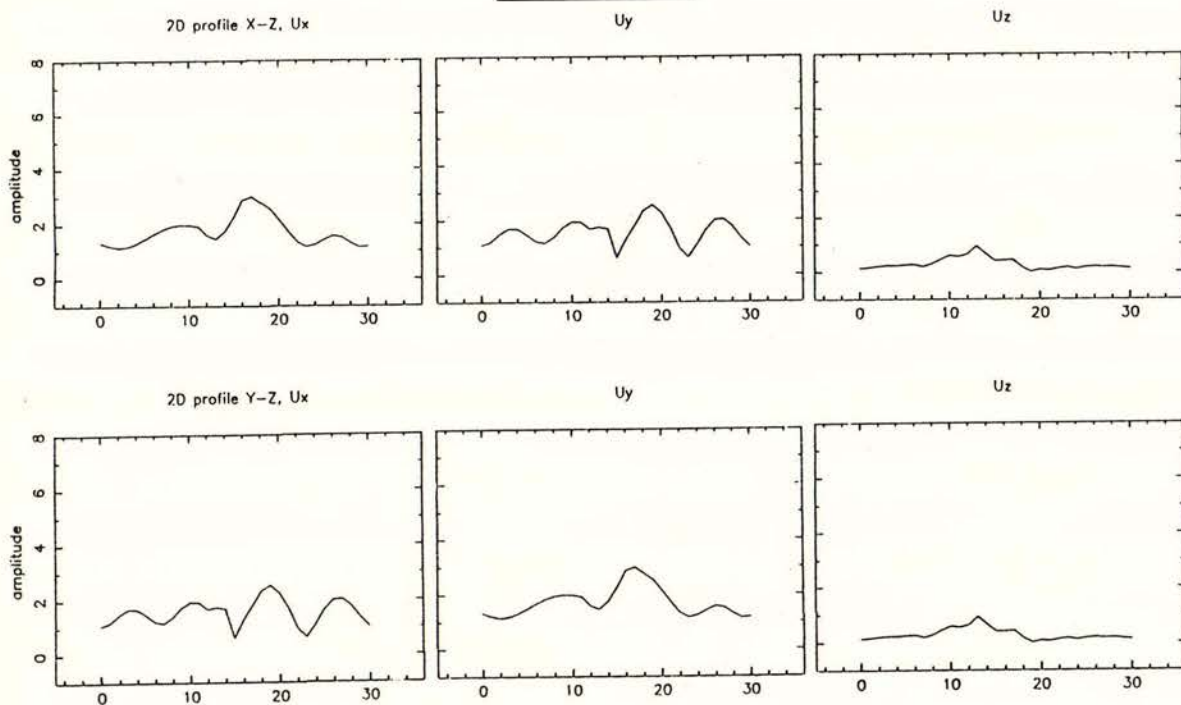
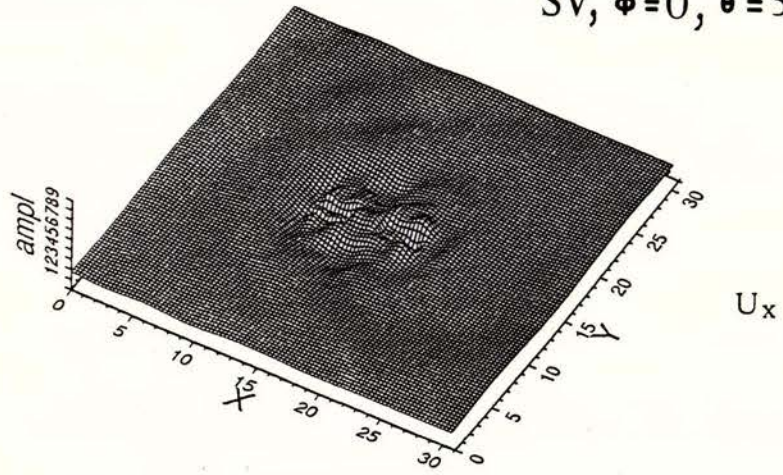


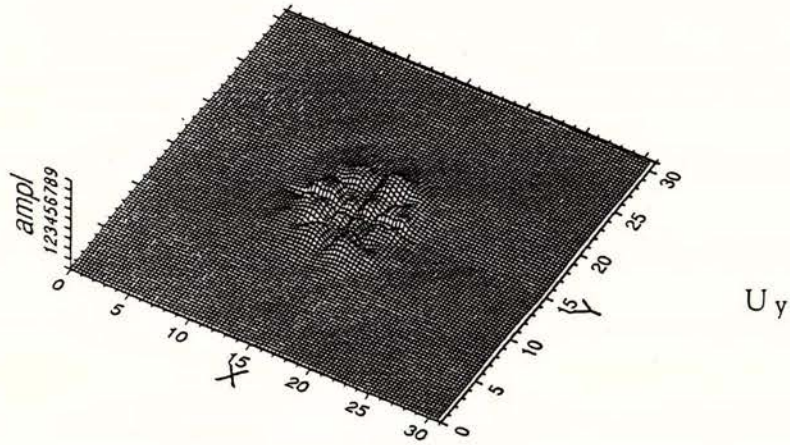
Figure 38. Amplitude distributions of the ground motion along two 2-D perpendicular profiles (described in Figure 27) of the 3-D ground motion due to a vertically incident SV wave with azimuthal angle  $\phi = 45^\circ$ , shown in Figure 37. Note that although the distributions are of identical variability as those of SV with  $\phi = 0$  (Figure 35), the amplitudes are about 50% smaller. The responses are symmetric along profiles X-Z and Y-Z passing through the center, and non-symmetric along profiles X-Z and Y-Z passing through  $x = 12$  km,  $y = 12$  km, as expected from the type of incidence, since these correspond to the absolute values of amplitude (i.e. phase of arrivals not included).



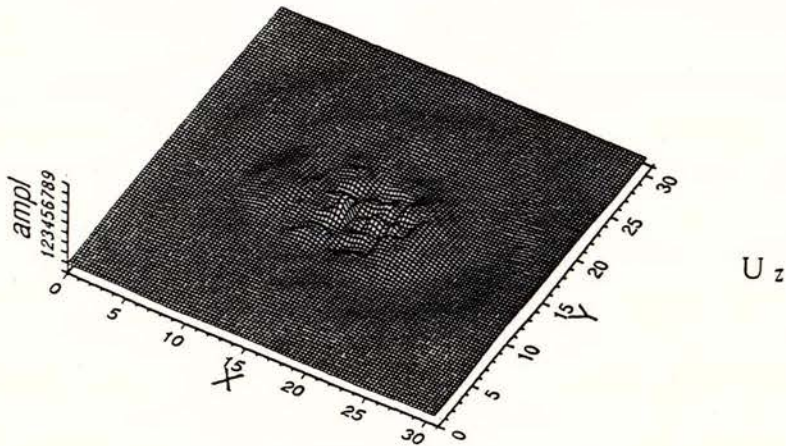
SV,  $\phi = 0^\circ$ ;  $\theta = 30^\circ$ ,  $\eta = 1.5$



$U_x$



$U_y$



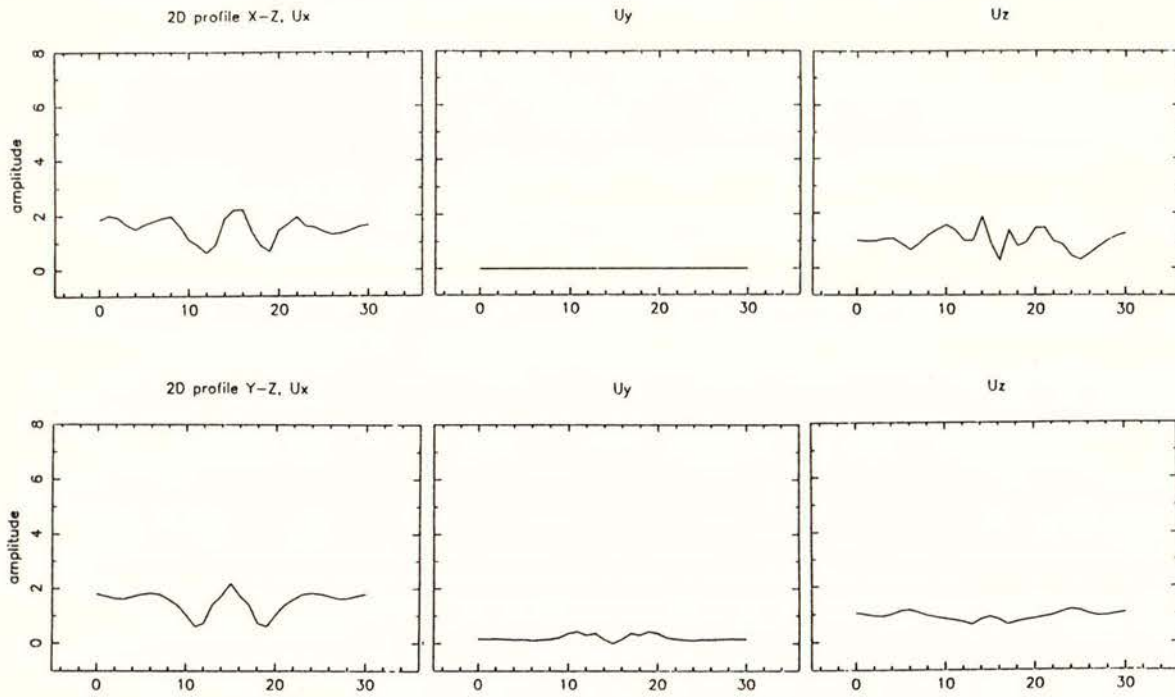
$U_z$

Figure 39 . 3-D views of the amplitude distributions of the ground response of the canyon described in Figure 25, to an SV wave incident with an angle  $\theta = 30^\circ$  and with azimuthal angle  $\phi = 0$  ( $\eta = 1.5$ ).



Canyon, SV,  $\theta = 30^\circ$ ,  $\phi = 0^\circ$

$x = 15$ ,  $y = 15$



$x = 12$ ,  $y = 12$

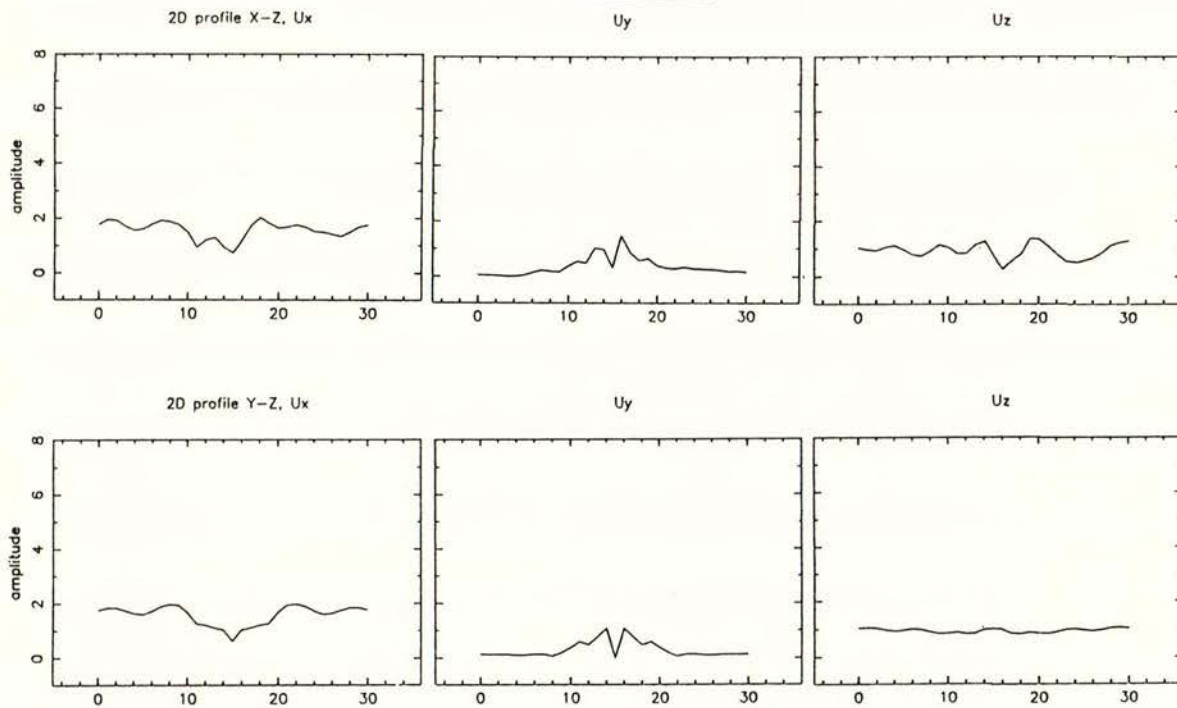


Figure 40. Amplitude distributions of the ground motion along two 2-D perpendicular profiles (described in Figure 27) of the 3-D ground motion due to an SV wave incident with angle  $\theta = 30^\circ$  and azimuthal angle  $\phi = 0$ , shown in Figure 39. In general, the responses are symmetric along the profiles Y-Z, as expected from the type of incidence.



## ACKNOWLEDGMENTS

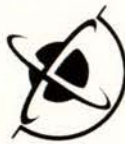
The authors express their gratitude to Bill Stephenson and to Euan Smith, whose critical comments helped to improve significantly the quality of the manuscript.

## REFERENCES FOR PART I AND PART II

- Aki, K., (1988), Local site effect on ground motion, in Earthquake Engineering and Soil Dynamics II - Recent advances in ground-motion evaluation, J. Lawrence Von Thun, Editor, *Am. Soc. Civil Eng. Geotechnical Special Publication 20*, 103-155.
- Aki, K., and Lerner, K.L., (1970), Surface motion of a layered medium having an irregular interface due to incident plane SH waves, *J. Geophys. Res.*, 75, 933-954.
- Aki, K., and Richards, P.G., (1980), *Quantitative Seismology: Theory and Methods*, Freeman and Co.
- Bard, P.Y., (1982), Diffracted waves and displacement field over two dimensional elevated topographies, *Geophys. J. R. Astr. Soc.*, 71, 731-760.
- Bard, P.Y., (1983), Site Effects: two-dimensional modelling and Earthquake Engineering, A workshop on "site-specific effects of soil and rock on ground motion and the implications for earthquake resistant design", *Proceedings of Conference XXII, United States Department of the Interior Geological Survey*.
- Bard, P.Y., Tucker, B.E., (1985), Ridge and tunnel effects: comparing observations with theory, *Bull. Seis. Soc. Am.*, 75, 905-922.
- Benites, R., (1990), Seismological applications of Boundary Integral and Gaussian beam methods, PhD thesis, Massachusetts Institute of Technology, Cambridge MA 02139, USA.
- Benites, R.A., and Aki, K., (1994), Ground motion at mountains and sedimentary basins with vertical seismic velocity gradient, *Geophys. J. Int.*, 116, 95-118.
- Benites, R.A., and Haines, A.J., (1991), The Riccati matrix equation- boundary integral method to compute seismic wavefields in heterogeneous media", *EOS, Transactions, American Geophysical Union, Vol. 72, No. 44*, 332 (abstract).
- Boore, D.M., (1972), A note on the effect of simple topography on seismic SH waves, *Bull. Seis. Soc. Am.*, 62, 275-284.



- Bouchon, M., (1973), Effect of topography on surface motions, *Bull. Seis. Soc. Am.*, 63, 615-32.
- Dakoulas, P., Gazetas, G., (1986), Seismic shear vibration of Embankment Dams in Semi-cylindrical valleys, *Earthquake Engineering and Structural Dynamics*, 14 (1), 19-40.
- Davis, L.L., West, L.R., (1973), Observed effects of topography on ground motion, *Bull. Seis. Soc. Am.*, 63, 283-298.
- Evans, J.F., Hadley, C.F., Eisler, J.D., and Silverman, D., A three-dimensional seismic wave model with both electrical and visual observation of waves, *Geophysics* 19, 220-236.
- Geli, L., Bard, P. Y., and Jullien, B., (1988), The Effect of Topography on Earthquake Ground Motion, *Bull. Seis. Soc. Am.*, 78, 42-63.
- Griffiths, D.W., Bollinger (1979), The effect of Appalachian Mountain topography on seismic waves, *Bull. Seis. Soc. Am.*, 69, 1081-1105.
- Haines, A.J., (1989), On the structure of one-way elastic wave propagation and exact solutions to the elastodynamic equations: theory for 2-dimensional SH waves, 259 pp monograph.
- Hudson, D.E., (1972), Local distribution of strong earth ground motion, *Bull. Seis. Soc. Am.*, 47, 221-250.
- Kawase, H., (1988), Time domain response of a semicircular canyon for incident SV, P, and Rayleigh waves calculated by the discrete wave number boundary element method, *Bull. Seis. Soc. Am.*, 78, 1415-1437.
- Kawase, H., (1990), Effects of topography and subsurface irregularities on strong ground motion. ORI Report 90-02, Ohsaki Research Institute, Inc., Tokyo, Japan.
- Lee, V.W., (1982), A note on the scattering of elastic plane waves by a hemispherical canyon, *Soil Dynamics and Earthquake Engineering* 1 (3), 122-129.
- Luco, J.E., Wong, H.L., de Barros, F.C.P, (1989), Three-dimensional response of a canyon in a layered half-space, University of California, San Diego, Department of Applied Mechanics and Engineering Sciences, Report.
- Macdonald, H.M., *Electric waves*, Cambridge University Press, Cambridge, England, 1902.
- Moen-Vaziri, N., Trifunac, M.D., (1981), A note on the vibrations of a semi-circular canal excited by plane SH-waves, *Bull. ISET*, 18.
- Mossessian, T.K., Dravinski, M., (1989), Scattering of elastic waves by three-dimensional surface topographies, *Wave Motion* 11, 579-592.



- Oliver, J., Press, F., and Ewing, E., (1954), Two-dimensional model Seismology, *Geophysics* 19, 202-219.
- Rogers, A.M., Katz, L.J., Bennett, T.J., (1974), Topographic effect on ground motion for incident P waves: a model study, *Bull. Seis. Soc. Am.* 64, 437-456.
- Sanchez-Sesma, F.J., and Rosenblueth, L., (1979), Ground motion at canyons of arbitrary shape under incident SH waves, *Int. J. Earthquake Engineering and Structural Dynamics*, 7, 441-450.
- Sanchez-Sesma, F.J., (1983), Diffraction of elastic waves by three-dimensional surface irregularities, *Bull. Seis. Soc. Am.*, 73, 1621-1636.
- Sills, L.B., (1978), Scattering of horizontally polarized shear waves by surface irregularities, *Geophys., J.R. Astr. Soc.*, 42, 747-768.
- Smith, W.D., (1975), The application of finite elements analysis to body wave propagation problems, *Geophys. J.* 42, 746-768.
- Trifunac, M.D., (1973), Scattering of plane SH waves by semi-cylindrical canyon, *Int. J. Earthquake Eng. Struct. Dyn.* 1, 267-281.
- Tucker, B.E., King, J.L., Hatzfeld, D., Nersesov, I.L. (1984), Observations of hard rock site effects, *Bull. Seis. Soc. Am.*, 74, 121-136.
- Umeda, Y., Kuroiso, Ito, K., Sakei, T., (1986), High accelerations in the epicentral area of the Western Nagano Prefecture, Japan, Earthquake of 1989, *J. Seism. Soc. Japan*, 39, 217-228.
- Voght, R.F., Wolf, J.P., Bachmann, H., (1988), Wave scattering by a canyon of arbitrary shape in layered half-space, *Earthquake Engineering and Structural Dynamics*, 16, 803-812.
- Wong, H.L., (1982), Effect of surface topography on the Diffraction of P, SV and Rayleigh Waves, *Bull. Seis. Soc. Am.*, 72, 1167-1183.
- Wong, K.C., Datta, S.K., Shah, A.H., (1986), Three-dimensional motion of a buried pipeline. I. Analysis, *Journal of Engineering Mechanics*, 112 (12), 1319-1397.
- Zhengpeng, L.Y., Baipo, L., Yifan, Y. (1980), Effect of three-dimensional topography on earthquake ground motion, *Proceedings of the 7th World Conference on Earthquake Engineering*, vol. 2, Istanbul, Turkey, September 8-13, 1980.

**INSTITUTE OF GEOLOGICAL & NUCLEAR SCIENCES LIMITED**

Corporate Services  
Gracefield Road  
PO Box 30 368  
Lower Hutt  
New Zealand  
Phone +64-4-570 1444  
Fax +64-4-569 0600

30 Gracefield Road  
PO Box 31 312  
Lower Hutt  
New Zealand  
Phone +64-4-569 0637  
Fax +64-4-569 0657

State Insurance Building  
Andrews Avenue  
PO Box 30 368  
Lower Hutt  
New Zealand  
Phone +64-4-569 9059  
Fax +64-4-569 5016

32 Salamanca Road  
Kelburn  
PO Box 1320  
Wellington  
New Zealand  
Phone +64-4-473 8208  
Fax +64-4-471 0977

Wairakei Research Centre  
State Highway 1, Wairakei  
Private Bag 2000  
Taupo  
New Zealand  
Phone +64-7-374 8211  
Fax +64-7-374 8199

Crown Research Dunedin  
764 Cumberland Street  
Private Bag  
Dunedin  
New Zealand  
Phone +64-3-477 4050  
Fax +64-3-477 5232